I.D. FOS Research E.E.I.G.
(European Economic Interest Grouping)

DBE TECHNOLOGY GmbH

Operational Safety Monitoring with Fiber Optic Sensing Systems

Final Report
Vol. II
- Technical Details -

Authors: Johan Vlekken[1]
Marc R-H Voet[1]
Michael Jobmann[2]

[1]I.D. FOS Research E.E.I.G., Cipalstraat 12, B-2440 Geel, Belgium
[2]DBE TECHNOLOGY GmbH, Eschenstraße 55, D-31224 Peine, Germany

Peine, June 2005

The reported research work has been funded by the Federal Ministry of Economics and Labour (BMWA = Bundesministerium für Wirtschaft und Arbeit) under the contract No FKZ 02E 9249. However, the authors are responsible for all the content.

Table of contents

1. Sensor development

1.1. Carbon protected temperature chain

A special type of a temperature cable has been developed. Since temperature cables will for example directly be installed in a borehole or in an engineered barrier system with different mechanical loads, a good protection mechanism of the optical fiber is requested. The ideal protection should fulfill the following criteria points:

1. low weight
2. flexible
3. small diameter
4. protection against harsh environments (corrosion)
5. protection against high tension loads
7. easy fabrication process
8. cause no delay in response time

As can be noticed, these criteria are not all fulfilled with standard protection systems such as the steel reinforced and armored outdoor and sub sea cables. Therefore, the development of a special temperature cable was started. The current research effort involved reinforcing the FBG sensor arrays with carbon using a standard pultrusion process. Cable test system and design are shown in 1.1 and 1.2. This design has the advantage that the carbon fibers give a very good protection against high tension loads without the need of over sizing the weight and diameter of the final cable. Furthermore, the carbon shield gives a very good protection against corrosion and can be made watertight.

Fig. 1.1: Temperature cable.

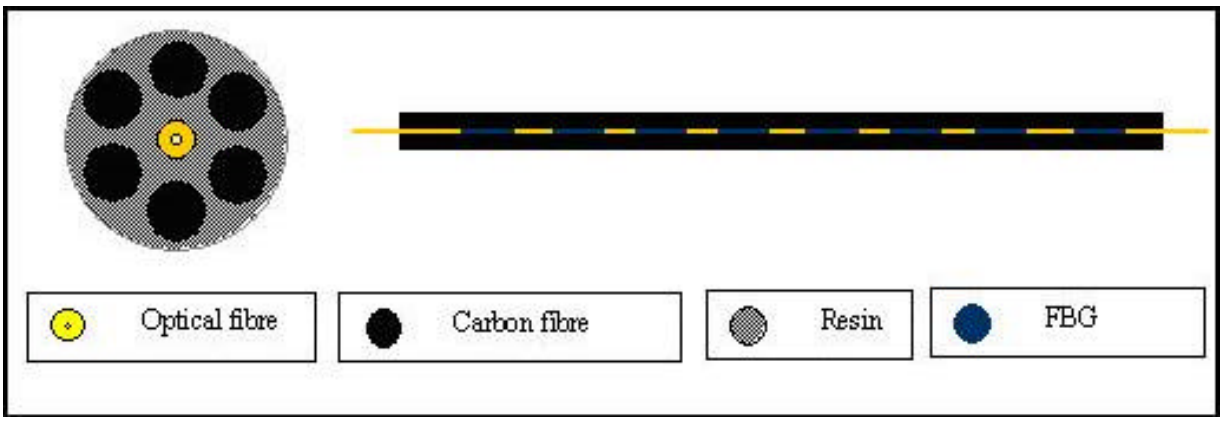

Fig. 1.2: Design temperature cable

The Pultruded Carbon Reinforced sensing fibre has been produced using a standard pultrusion process. Fig. 1.3 shows a schematic diagram of the process. Six carbon fibres with a diameter of 700 µm and one polyimide coated glass fibre with a diameter of 155 µm are pulled through a resin impregnation bath (Epoxy resin). The glass fibre is positioned at the centre and contains one FBG with a nominal wavelength of 1531.8 nm at 20°C.

Subsequently, the fibres go through a shaping die of 2 mm diameter and are subsequently cured to harden out the resin. The resulting part is a 2 mm diameter carbon reinforced sensing fibre. This production process can be fully automated and allows the fabrication of very long lengths, up to several km.

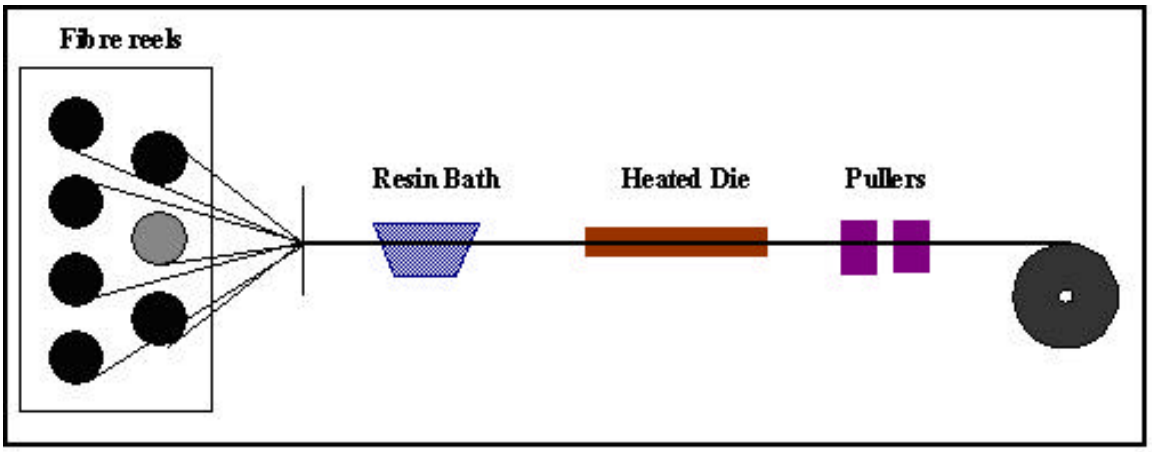

Fig. 1.3: Schematic overview of pultrusion process

In order to characterise the temperature cable, three different experiments were performed. In a first experiment, a temperature calibration has been performed. The temperature is changed from 0 up to 70°C in steps of 10°C. Each time thermal equilibrium has been reached, the wavelength has been recorded. The result of this experiment is shown in Figure 1.4. As can be seen, a good linear relation is obtained. The sensitivity is equal to 8.5 pm/°C. This is lower than the sensitivity of the naked FBG which has been measured to be equal to 9.8 pm/°C. This can be explained by the negative thermal expansion coefficient of the carbon fibre. Due to the increasing temperature, a negative strain is applied on the FBG by the carbon fibres resulting in a decrease of the temperature sensitivity.

Notice that this change in temperature sensitivity is determined by the type of reinforced fibres and the used resin. As a consequence, by choosing other materials, the temperature sensitivity can be increased or decreased dependent on the requested specifications. For example, using a mix of carbon and glass as reinforced fibre will increase the temperature sensitivity.

In a second experiment the temperature response time of the temperature cable has been investigated. It is important that the reinforcement does not increase too much the response time. A comparison was made between a naked FBG and the carbon reinforced FBG. Both fibres were put into a climatic chamber. After stabilising to a temperature of 70°C, the temperature was suddenly changed to 25°C.

Fig. 1.5 shows the normalised temperature change of the naked and the carbon reinforced FBG as function of time. The carbon reinforced FBG shows a similar temperature response as the naked FBG, so it can be concluded that almost no delay is induced by the carbon reinforcement. Based on the previous two results it is proven that the temperature cable is suitable for temperature measurements.

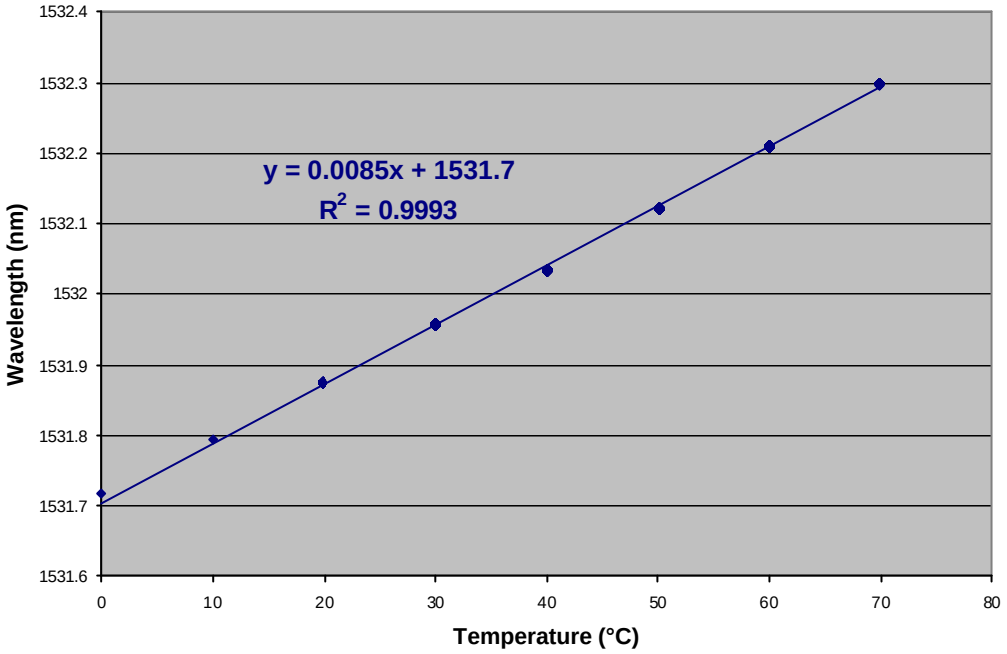

Fig. 1.4: Temperature calibration of temperature cable

Finally, in a third experiment, some strain tests were applied. The temperature cable was put under different load levels, ranging from 0 up to 5 kg and back from 5 to 0 kg. The result is shown in Figure 1.6. A good linear behaviour between wavelength and load can be observed with a sensitivity of 24pm/kg. Since the sensitivity of the naked FBG is around 10 nm/kg, this indicates that the reinforcement is working very well. Furthermore, almost no hysteresis is observed. This makes this type of cable also suitable for strain measurements.

Notice that the maximum load level of 5 kg has been limited by the experimental set-up and not by the cable itself. The cable can sustain much higher load levels, dependent on the type of carbon fibres, resin, and adaptive diameter.

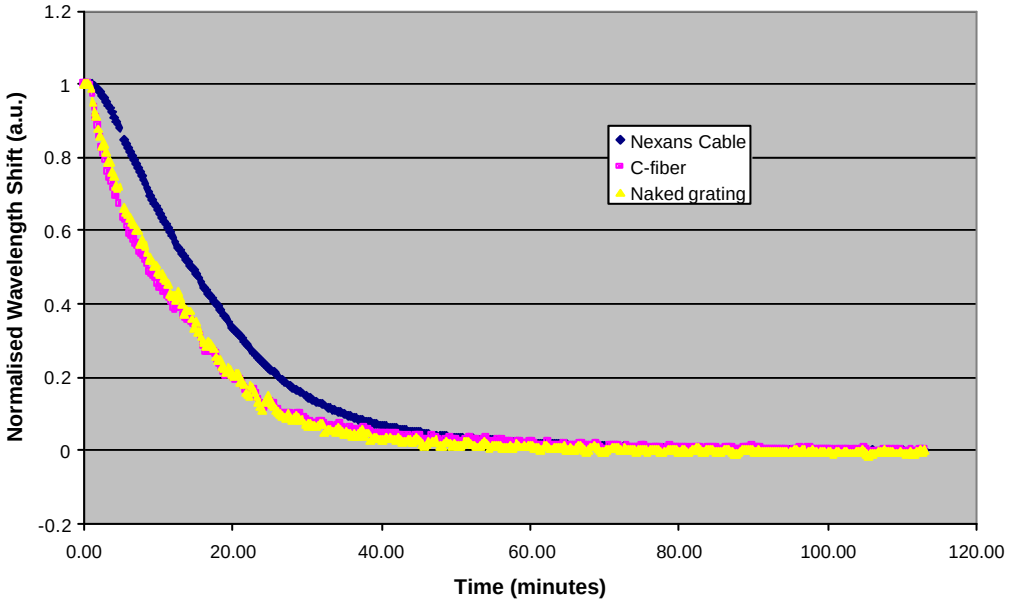

Fig. 1.5: Response time of temperature cable

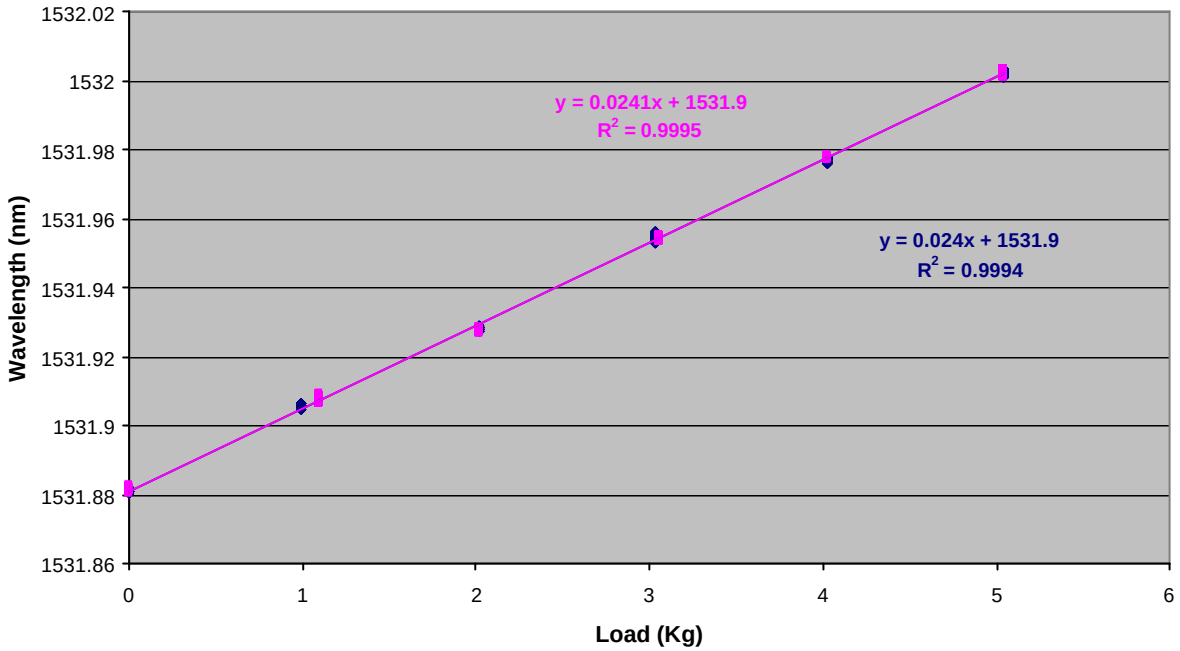

Fig. 1.6: Strain test on temperature cable

1.2. Fissurometer (mountable strain sensor)

The mountable strain sensor has been fine-tuned for an application at the Morsleben site. Compared to the displacement sensors used at the Konrad site, this sensor has the advantage that it has a higher sensitivity (and therefore also a better resolution) as is shown at the end of this paragraph. In Fig. 1.7 and Fig. 1.8, the design and a photo of the high sensitive fissurometer is shown.

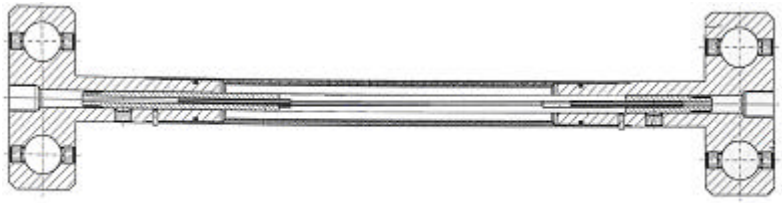

Fig. 1.7: Design fissurometer

Fig. 1.8: Photo fissurometer

The fissurometer consists out of two anchoring pieces in which between a fibre with a FBG is stretched. Both points are connected using a metallic tube in order to protect the fibre. The sensor is designed in such a way that the metallic tube can slide over the short inner tubes of the anchoring points. As a consequence, in opposite to the strain sensor, the metallic tube is not inducing a counter force when the sensor becomes longer. This makes the fixation of the sensor on the structure less critical and the measurements more accurate.

A second difference with the strain sensor is the mounting mechanism of the fissurometer. The fibre containing the FBG is not stretched during the assemblage of the sensor. The strain offset is put on the fibre during the mounting of the sensor. The fixation holes are larger than the bolts used to fix the sensor to the structure. In order to fix the sensor tightly, the bolts are fixed in the holes by imbus screws located at each side of the hole. By tightening first the outer imbus screws, a strain offset can be put in a controlled manner on the FBG. The advantage of this system is that the sensor can easily be reset for further measurements when the displacement has reached its maximum range. Finally, the fissurometer has a second FBG in an unstressed state for taking into account the temperature sensitivity of the strain-FBG.

The sensitivity of the fissurometer is determined by the length of the free fibre (L_f) and the sensitivity to strain of the strain-FBG (b):

$$S = (b/L_f) .10^6$$

With S the sensitivity (wavelength shift/displacement) in nm/mm

b the strain sensitivity of the FBG expressed in nm/με

L_f the free length of the stretched fibre in mm

(Remark: 1 με = 1 microstrain and is defined as an elongation of 1 μm over a length of 1m)

In order to determine the sensitivity factor experimentally, a calibration bench was constructed (Fig. 1.9). The calibration bench allows to displace one of the end points on a controlled manner while keeping the other end point fixed. The displacement is measured using a conventional displacement meter.

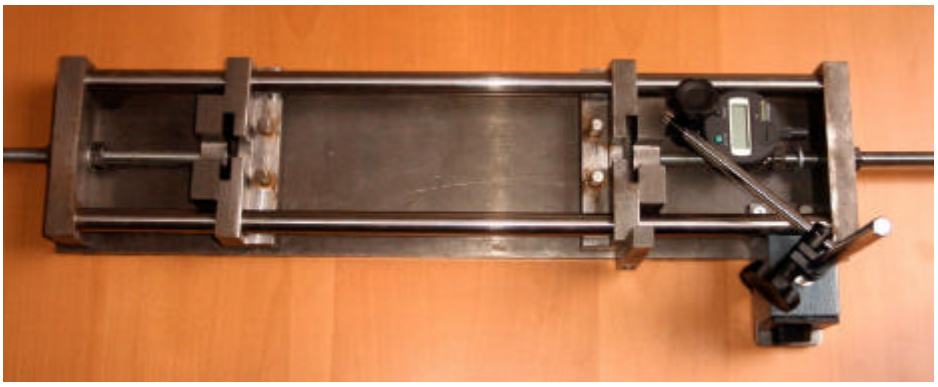

Fig. 1.9: Calibration bench fissurometer

A high sensitive fissurometer was built and characterised. Taking into account the length of the free fibre (100 mm) and the strain sensitivity of the FBG (1.2 nm/με) a sensitivity of 12 nm/mm is expected. The results of the calibration is shown in Figure 1.10. A sensitivity factor of 11.857 nm/mm was experimentally observed, which is in good correspondence with the theoretical value. Furthermore, a good linearity is observed (R^2 = 0.9998). The sensitivity can further be increased by decreasing the length of the stretched fibre.

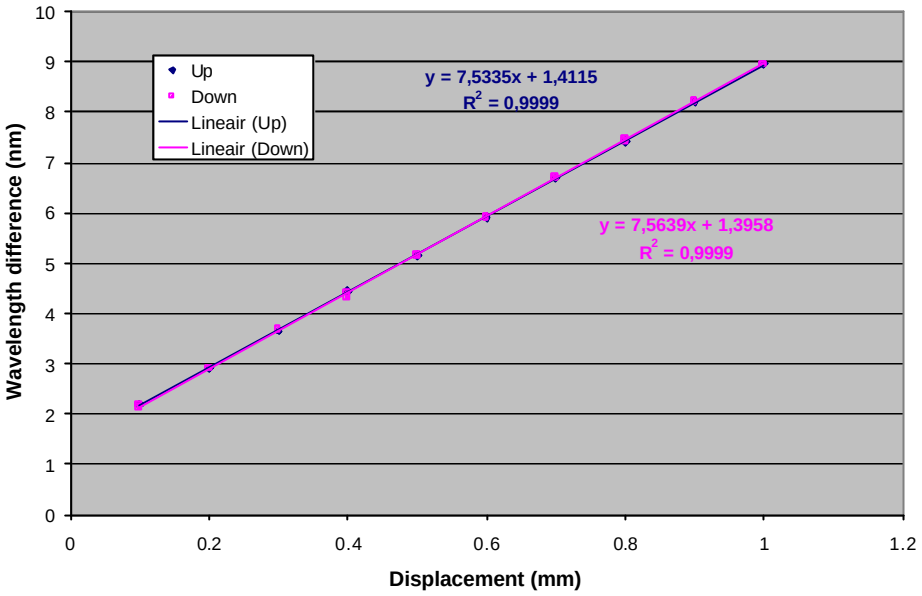

Fig. 1.10: Calibration results fissurometer

1.3. High resolution strain cable

A new type of strain cable has been developed for application at the Morsleben site. The sensor as well as the connection mechanism has been redesigned. Both parts will now be discussed.

1.3.1. The strain sensor

A schematic drawing of the opto-mechanical cell is shown in Fig. 1.11. The cell consists of a metallic tube with a fixation point on each end. Between both fixation points a fibre containing a Fibre Bragg Grating (FBG) is stretched. This FBG is called the strain-FBG. One fixation point of the cell can slide when it is pulled to the outward direction. As a consequence the FBG becomes more or less strained resulting in a wavelength shift. An other parameter influencing the wavelength shift is the temperature. A sensitivity of 10.46 pm/°C is expected. In order to compensate for these influences, a second FBG which remains all the time unstrained, is used. This FBG is called the temperature-FBG and allows monitoring the temperature.

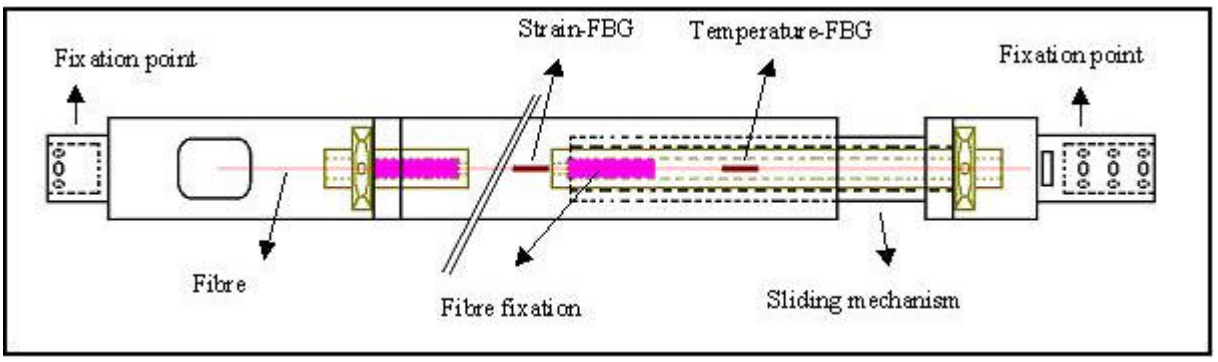

Fig. 1.11: Schematic drawing of opto-mechanical cell

The relative displacement (Δd) of the sliding fixation point can be calculated using the wavelength shift of the strain-FBG ($\Delta\lambda$), the strain sensitivity of the grating (=1.2 pm/με) and the length of the fibre under stress (L_{FBG}):

$$\Delta d = \Delta\lambda \,.\, L_{FBG} \bullet 10^{-6} \,/\, 1.2 \qquad (1.1)$$

with Δd and L_{FBG} expressed in mm and $\Delta\lambda$ expressed in pm.

The resolution of the sensor is mainly defined by the resolution of the interrogation unit and is as function of the length of the fibre under stress (L_{FBG}). The resolution of the interrogation unit is typically 1 pm. This corresponds to a displacement resolution (d_{res}) of the opto-mechanical cell of:

$$d_{res} = L_{FBG} \bullet 10^{-6} / 1.2 \qquad (1.2)$$

The range of the sensor is defined by the maximum strain that the strain-FBG can sustain. Special fabricated FBGs are used which can sustain a strain of up to 5%. In order to assure a reliable working of the sensor, only the half of the maximum strain level is used (2.5 %). This corresponds to a strain range of:

$$d_{range} = LFBG \bullet 0.025 \qquad (1.3)$$

Based on equation (1.1) and (1.2) it can be calculated that the resolution is $3.33 \bullet 10^{-4}$ of the full range.

This type of sensor can be customised very easily. Depending on the requirements requested by the application. L_{FBG} can be chosen between 10 cm and 1 m. Fig. 1.12 shows a photo of a strain sensor with L_{FBG} around 680 mm. The cell was calibrated using a calibration set-up special designed for this type of sensor. This result is shown in Fig. 1.13. As can be observed, a very good linear relation is observed (R^2 =1) and almost no hysteresis is present.

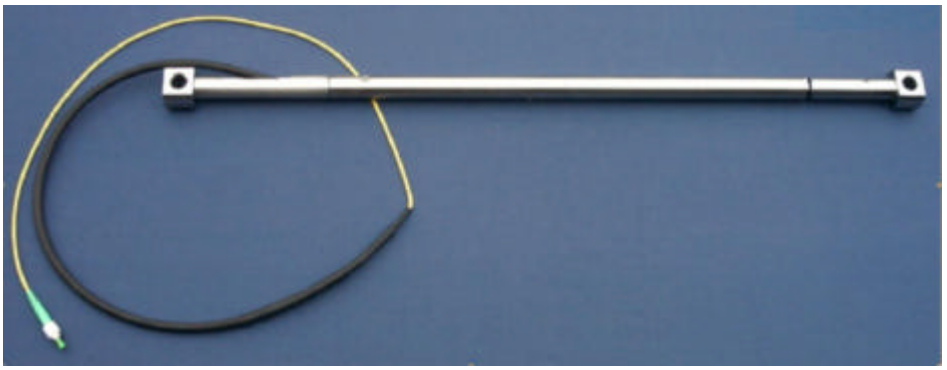

Fig. 1.12: Photo of strain sensor

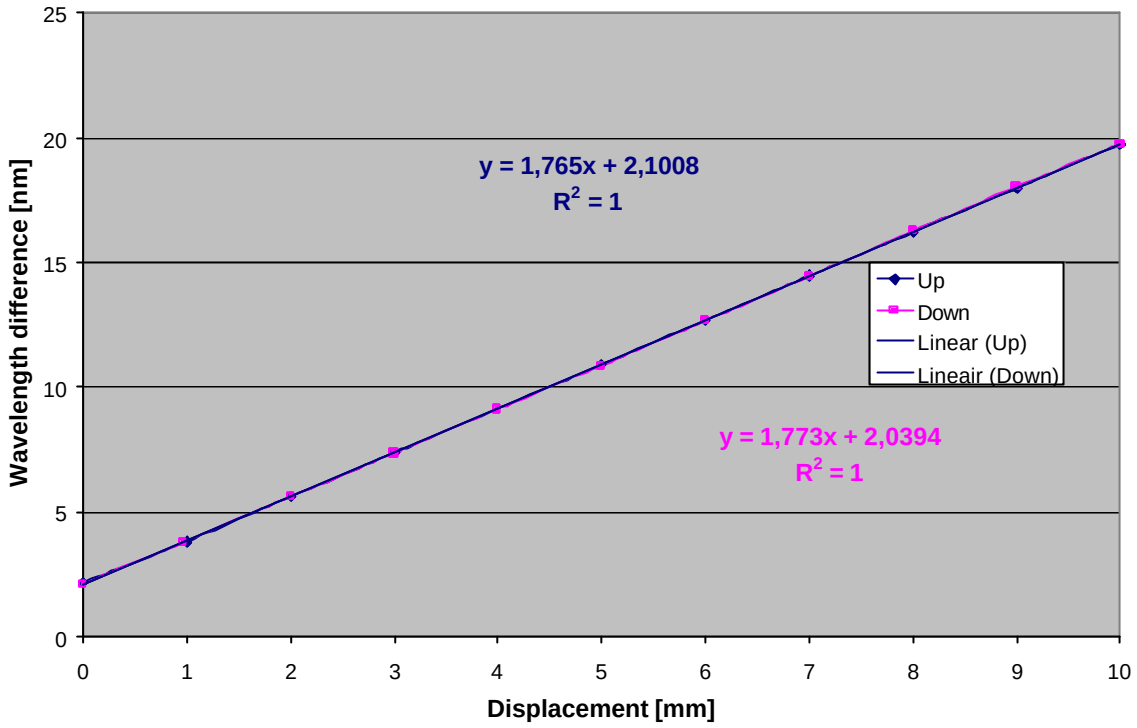

Fig. 1.13: Calibration curve of strain sensor

1.3.2. The strain cable connection mechanism

In order to transfer the displacement between two packers to the opto-mechanical cell, carbon tubes are used. The tubes do have an outer diameter of 22 mm, an inner diameter of 18 mm and a low thermal expansion coefficient of $6 \cdot 10^{-7}$. This low thermal expansion coefficient is especially important in order to minimise the displacement errors caused by temperature changes.

The carbon tubes have a length of 3 m. In order to cover longer distances between two packers, connection rods made of stainless steel are used (Fig. 1.14). At both sides of the connection rods, the carbon tubes are slide to the centre and screwed using 6 bolts each. In order to circumvent a bend of the carbon tube due to the weight of the stainless steel rod, a dummy packer in PVC is positioned at the centre. This dummy packer is foreseen of the necessary holes to guide the pressure and signal tubes of the strain cable.

Fig. 1.14: Connection piece for carbon rods and dummy packer

1.3.3. Adaptation packers

In order to obtain a high resolution strain cable, the knee coupling fixation mechanism between the rods and the packers of the former strain cable (applied at the Konrad mine) has been changed by a similar principle as the connection piece (Fig. 1.15). The carbon tube is also here fixed using six bolts.

Fig. 1.15: Carbon - Packer fixation mechanism.

1.4. Development fatigue testing system for pressure cells

A system for automatic fatigue testing of pressure cells has been developed to measure the fatigue behaviour of the pressure membranes. The system allows to test the sensor sequentially under 5 different pressure levels. Example: 1 bar – 2 bar –3 bar – 4 bar – 5 bar. After this sequence the pressure will be released and the next sequence will start. During the cycling, the system measures and saves the wavelengths together with the corresponding pressure levels. The system consists of 4 main parts:

1. Pressure board
2. Electronic module
3. Laptop + software
4. FBG-IS

Since the last part is well known, only the first three parts will be discussed. The pressure board is shown in Fig. 1.16. A high pressure level, produced by a compressor will serve as input on this pressure board (5). Before going down in the circuit, the inlet passes a double overpressure protection valve (1). This allows limiting the pressure to the maximum allowed value that the membrane can sustain (example 5 bar) in order to avoid plastic deformation of the membrane. Under the protection valves, five other pressure valves are used to set the individual pressure levels for the fatigue testing. After each pressure valve, a relay controlled ON/OFF valve is placed (2). This relay can be controlled using a 24 V signal. The different relays are controlled using the software and the electronic module. Each ON/OFF valve will sequentially be opened and the corresponding pressure level at that place will pass via the output line (4) to the sensor (sensor is connected with the right side of the output line. After one complete sequence is finished, the ON/OFF valve (3) will be activated what results in a pressure release of the sensor.

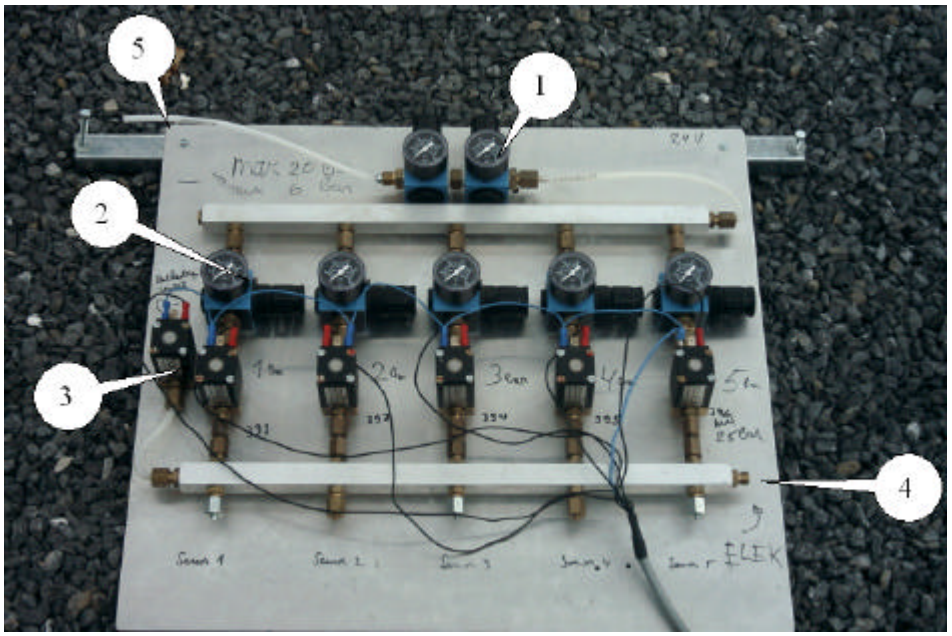

Fig. 1.16: Pressure board

The electronic module consist of different ON/OFF relays. These are controlled using a Labview program and a Data Acquisition Card (DIO 24). Before sending the signals of the DAQ to the relays, they will be first amplified to a 24 V signal using the electronic module.

The complete system is controlled using a Labview program. Fig. 1.17 shows the front panel of the software program. A brief explanation of the software settings :

Select measurement mode : After Time - During Time

This button is needed to select the measurement mode :

After Time: in this mode, the wavelengths are recorded for each pressure step after a stabilisation period. After the measurement, the next pressure step will be set.

During measurement: in this mode the wavelengths are continuous recorded during the fatigue testing.

Pressure steps : (default = 5)

Defines the number of pressure steps of one sequence.

 # (number) of lines to measure :

Different sensors can be tested simultaneously using an optical switch (GP 700 from Dicon). This number defines the total amount of lines that will be measured.

Time : (in minutes)

This array defines the setting time for each pressure step.

Path :

Defines the location where the file will be stored on the computer (TXT format)

'After time' and 'During measurement'

The 2 arrays 'after time' and 'during measurement' display the measured wavelengths. This allows checking the measurements at any time.

'STOP' button

The system can be stopped all the time using the stop button.

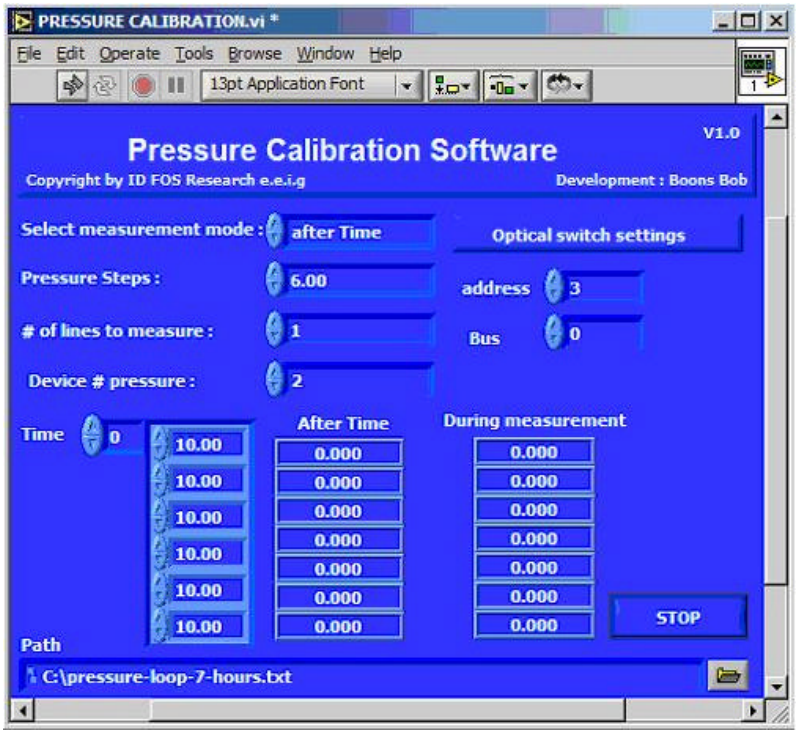

Fig. 1.17: Software control panel

1.5. Porewater pressure sensor

A new design for the pore water pressure sensor has been build. The sensor is designed for measuring pressures up to 50 bar at temperatures up to 180°C. For example, these specifications where required for the field experiments at Äspö. The sensor has been designed such that the dimension is kept as small as possible. Due to the high temperature levels a new calibration method and system set-up has been made.

1.5.1. Sensor design

The measurement principle of the fibre optical pressure cells is shown in Fig. 1.18. The membrane pressure sensor hosts a mechanism that aims to allow the dimensioning of the sensor and especially to improve its sensitivity. The mechanism consists in a circular membrane closing at one end the pressure sensing cell. The pressure to be measured is applied on the front of the membrane.

An optical fibre hosting two FBGs is glued in two capillaries. The pressure sensing FBG is glued between the first capillary and the second capillary whereas the temperature compensating FBG is located in the second capillary. The fibre pigtail is spliced to the temperature compensating FBG. At the output of the first capillary, the optical fibre is bevelled.

The first capillary is fixed onto the membrane, behind the membrane, at the centre and is perpendicular to the plane of the membrane. The second capillary is fixed at the end of the holder which is screwed to and behind the membrane.

Fig. 1.18: Basic design of the membrane pressure sensor

The pressure FBG is pre-stretched between the centre of the circular membrane and the holder. The pressure to be measured is applied onto the membrane and bends it slightly resulting in a displacement of its centre. The pressure FBG is thus released by increasing the pressure while it is stretched by decreasing the pressure. The FBG spectral shift $\Delta\lambda_{FBG}$ is proportional to the pressure difference $P - P_{atm}$ according to equation (1.4) :

$$\Delta\lambda_{FBG} = b_{FBG} \cdot \Delta\varepsilon_{FBG} = b_{FBG} \cdot \frac{\Delta d_{memb}(th_{memb}; Y_{memb}; \sigma_{memb}; (P - P_{atm}))}{L_{0FBG}} \qquad (1.4)$$

Δd_{memb} : displacement of the centre of the membrane
b_{FBG} : FBG strain sensitivity
$L_{0\,FBG}$: FBG length at rest
th_{memb} : membrane thickness
Y_{memb} : membrane Young' modulus
σ_{memb} : membrane Poisson ratio.

The displacement of the centre of the membrane is given by equation (1.5) with R_{memb} the radius of the membrane.

$$\Delta d_{memb} = \alpha R_{memb}^{3} \sqrt{\frac{(P - P_{atm}) R_{memb}}{Y_{memb}\ th_{memb}}} \qquad (1.5)$$

with:

$$\alpha = \sqrt[3]{\frac{6615(\sigma_{memb}^{2} - 1)}{2\ (2791\sigma_{memb}^{2} - 4250\sigma_{memb} - 7505)}} \qquad (1.6)$$

Based on this principle a new design has been made. The new pore water pressure sensor has a length of 260 mm and a maximal outer diameter of 30 mm. The dimensions of the new pore water pressure sensor are shown in Fig. 1.19.

Fig. 1.20 shows the different parts of the sensor. The sensor has been created in stainless steel as well as Titanium. Titanium does has the advantage that it is much more resistant against corrosion. The disadvantage is however the price aspect due to the higher material cost and the more extensive labour required for this material.

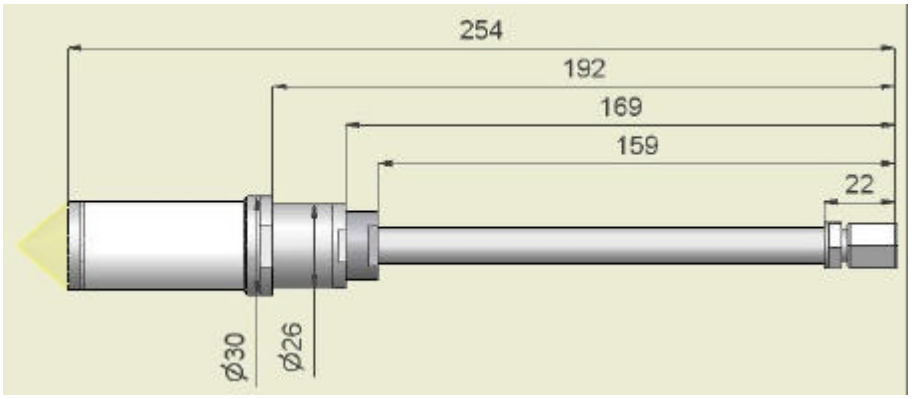

Fig. 1.19: Dimensions of the pore water pressure sensor

Fig. 1.20: Graphical presentation of all the parts of a pore water pressure sensor.

The new pressure sensor has the advantage that the required membrane thickness is much easier to fabricate compared to previous design. As can be seen in Fig. 1.20, the membrane is on top of part OT-SN 100 005. The thickness of this piece can very easily be modified using a polishing process. With the previous sensor design this needed to be done using a milling process what is much more difficult. As a consequence it is very easy to change the pressure range.

The maximum range of the pore water pressure sensor depends on the thickness of the membrane. For each thickness of a membrane there is a pressure where the material

undergoes a deformation. This is the maximum pressure that might be applied to the sensor in order not to damage the sensor.

Fig. 1.21 shows the calibration of a 0.9 mm membrane. It's very clear that the deformation takes place at a pressure of 110 bar. So this membrane would be perfect for a 100 bar pore water pressure sensor. Table 1.1 shows the deformation pressures for the different membrane thickness.

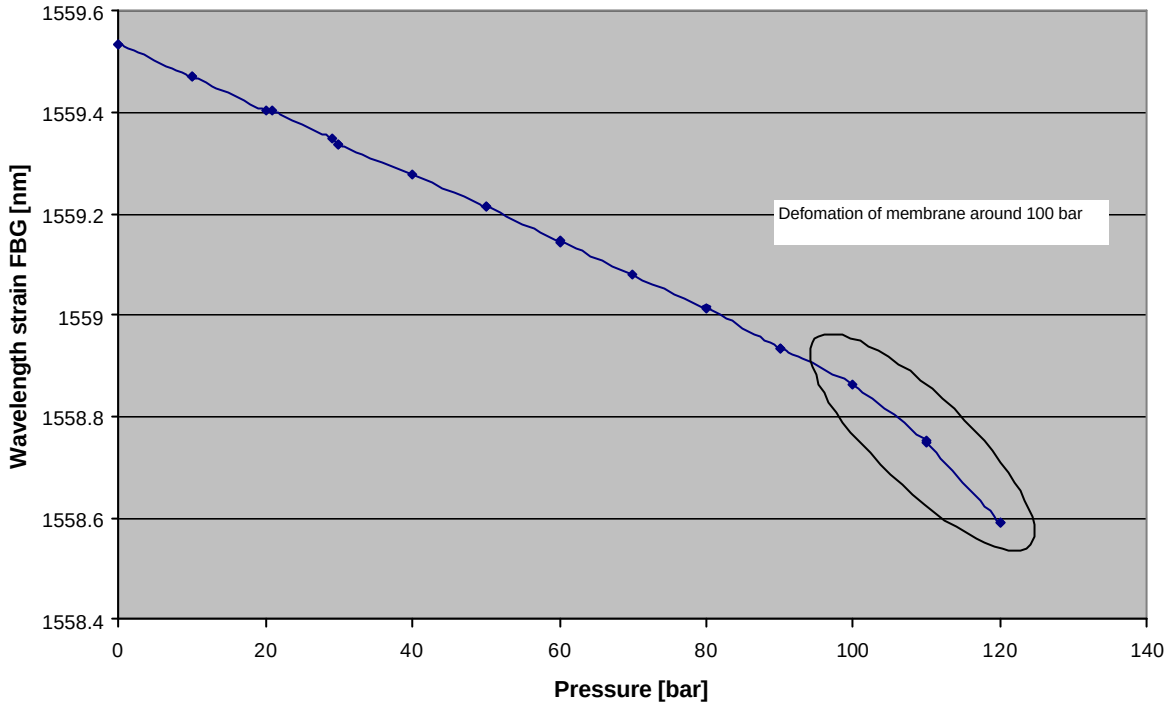

Fig. 1.21: Calibration of a 0.90 mm stainless steel membrane

Thickness	Deformation
0.280 mm	1.5 bar
0.340 mm	6 bar
0.350 mm	8 bar
0.420 mm	30 bar
0.700 mm	70 bar
0.900 mm	110 bar
1.000 mm	130 bar
1.250 mm	150 bar
1.400 mm	180 bar

Table 1.1: Deformation for different membrane thickness

In order to satisfy the high temperature conditions two problems needed to be resolved. The first problem was the fixation of the fibre into the capillaries. Our standard glue didn't resist the high temperature and created a lot of pre-strain losses. The solution is a new type of glue: EPO-TEK 353ND. This is a heat curing epoxy, designed for high temperature applications. Although this glue will work properly at 200°C, it will also endure temperatures in the 300-400°C range for several minutes.

The second problem was the use of the standard o-seals. These could only withstand a temperature of 90°C. At higher temperature the o-seal will melt and there would be a leakage from the outside of the sensor to the inside. This will damage the fibre and influence the

measured results. A new kind of o-seals gave the solution for this problem. It was the 'Viton' o-seal that can resist a temperature of 200°C.

The final pore water pressure sensor is available in three different versions as is shown in Fig. 1.22. The first version is the thread version. The pore water pressure sensor can be foreseen of a customised thread such that the sensor can be screwed on for example a pipeline. The second version is foreseen of a cylindrical porous stone and may be used for imbedding the sensor into all types of ground layers. The third version is with a flat porous stone. This type is used to measure liquid pressures in for example liquid tanks.

Fig. 1.22: Three possibilities for a pore water pressure sensor

1.5.2. Calibration method

The calibration method has also been changed. In the past, the pressure sensors were calibrated by recording the wavelength difference between the temperature and strain FBG as function of pressure. The wavelength difference was taken in order to compensate for the intrinsic temperature sensitivity of the gratings. However this method does not take into account the effect of the thermal expansion of the housing on the strain FBG. This problem is illustrated in Fig. 1.23. The wavelength of the strain FBG has been recorded for a stainless steel pressure cell at different temperatures but each time for atmospheric pressure. As can be observed, the wavelength difference is not constant at all. This can be explained by the thermal expansion of the inner tube (part OT-SN 100 008) in the housing which is causing a strain on the strain FBG when temperature increases, resulting into an extra wavelength increase.

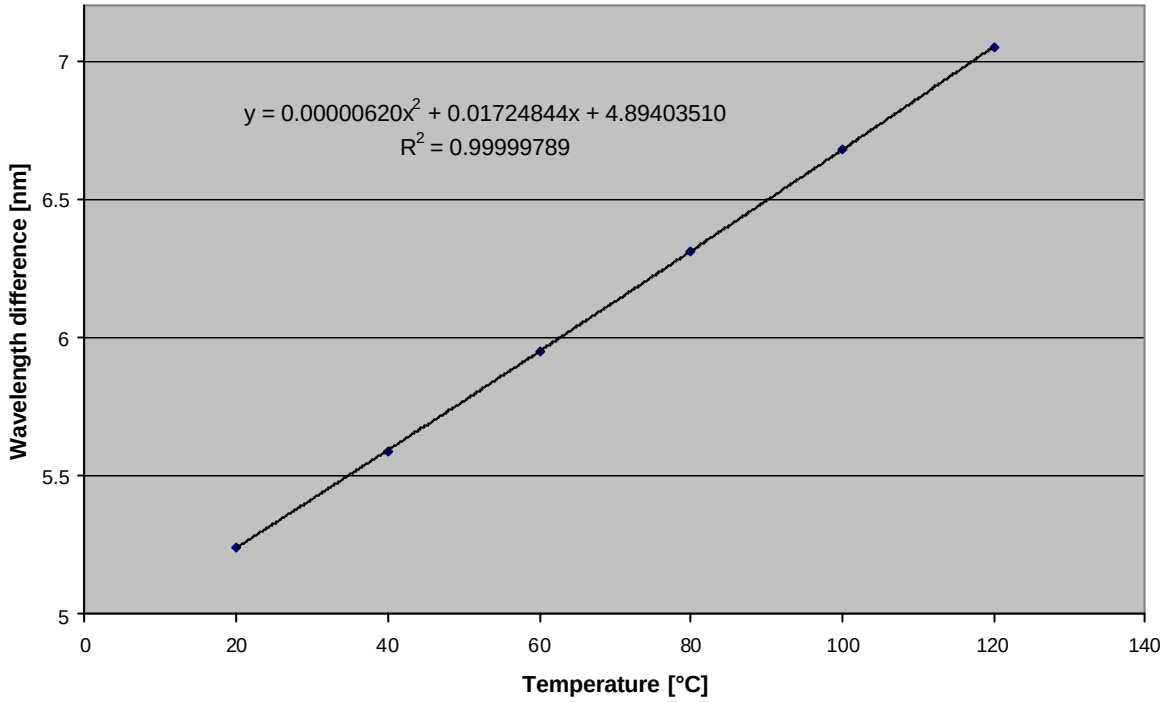

Fig. 1.23: Wavelength difference of a stainless steel pore water pressure cell at P=0 bar, measured at different temperatures.

In order to take these effects into account, a new calibration method has been used based on a more detailed study of the behaviour of the pressure sensors for different temperatures. Fig. 1.24 shows the different pressure calibration curves of a 50 bar stainless steel pressure sensor for different temperatures. For each temperature, the wavelength difference has been recorded as function of the pressure. As can be observed, a good linear relation is obtained for all curves that can be described as:

$$P = \Delta\lambda(P = 0) - D \,.\, \Delta\lambda \qquad (1.7)$$

As can be observed in Fig. 4.24, the parameter D is more or less constant for all different temperatures. The offset at the other hand (wavelength difference at P=0 bar) is strongly dependent on the temperature as has been shown in Fig. 4.23. As can be seen, the offset is parabolic dependent on the temperature:

$$\Delta\lambda(P = 0) = a + b \,.\, T + c \,.\, T^2 \qquad (1.8)$$

Since the temperature is directly linear as function of the wavelength of the temperature FBG (λ_T), the final equation of the pressure can be written as:

$$P = A + B \,.\, \lambda_T + C \,.\, \lambda_T^2 - D \,.\, \Delta\lambda \qquad (1.9)$$

with A, B, C and D constants.

With the new calibration method this equation is used. In order to determine the constants A, B, C and D, the pressure calibration curves at different temperatures are first recorded. Then, the simplex method is applied on this data set to determine the parameters A, B, C, and D. Table 1.2 shows the results of the simplex method applied on the data shown in Fig. 1.24. With these parameters a mean deviation of 0.6% full scale has been obtained.

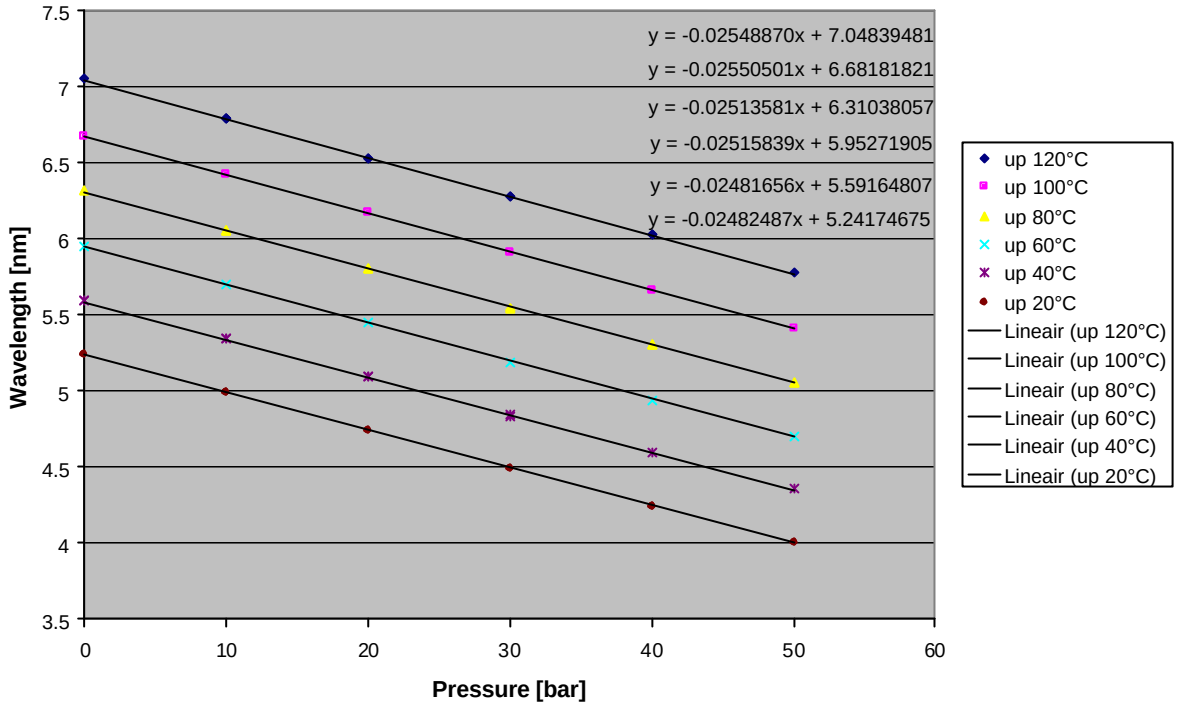

Fig. 1.24: Total calibration sheet of the stainless steel pore water pressure sensor

A =	-4067210.854994120
B =	5246.264175423990
C =	-1.691412004339330
D =	39.78759261059540

Table 1.2: Results of simplex calculation for stainless steel pore water pressure cell.

The same calibration method can also be used for the Titanium pore water pressure cells. Fig. 1.25 shows the wavelength difference for P=0 bar of a 50 bar titanium pore water pressure sensor at different temperatures. As can be observed, the wavelength difference shows also a parabolic dependence as function of the temperature. This can also be explained by the thermal expansion of the housing. It needs to be noticed that the temperature dependence is smaller than with the stainless steel sensor. This is due to the lower expansion coefficient of the Titanium material.

Fig. 1.26 shows the pressure calibration curves at different temperatures. Again, a good linear behaviour can be found with a similar slope at the different temperatures. As a consequence, a similar calibration method as with the stainless steel pressure cell can be used. Table 1.3 shows the results of the simplex method applied on the data in Fig. 1.26. With these constants, a mean deviation of 0.82% full scale is obtained.

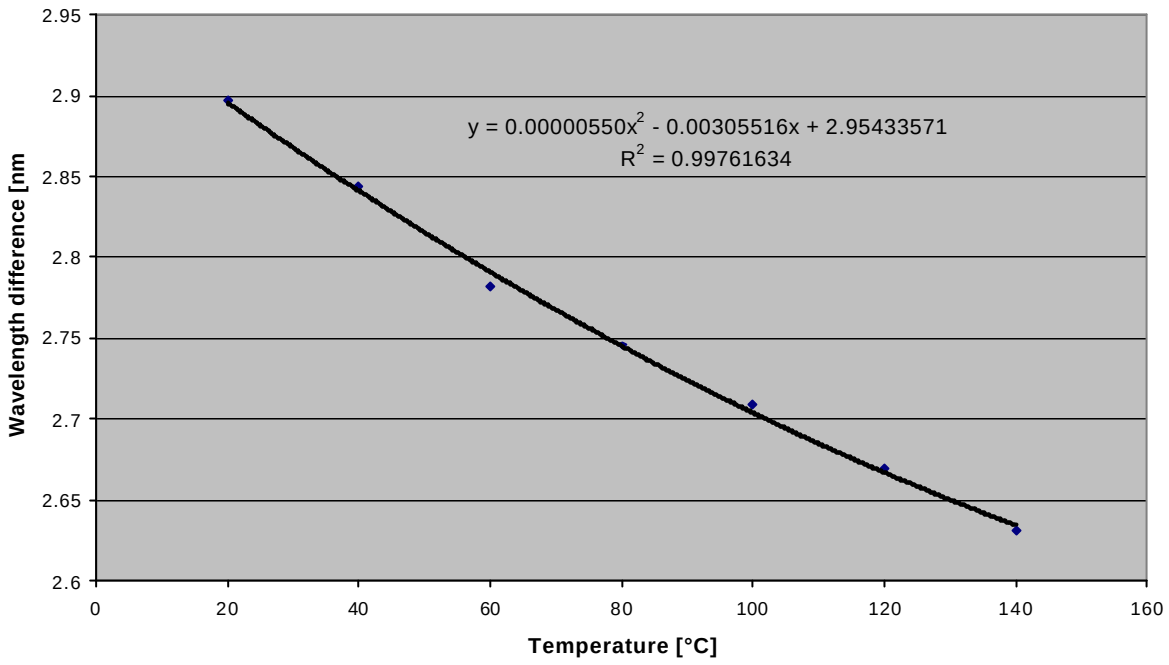

Fig. 1.25: Wavelength diff. of titanium pore water pressure cell at P=0 bar, at measured diff. temperatures.

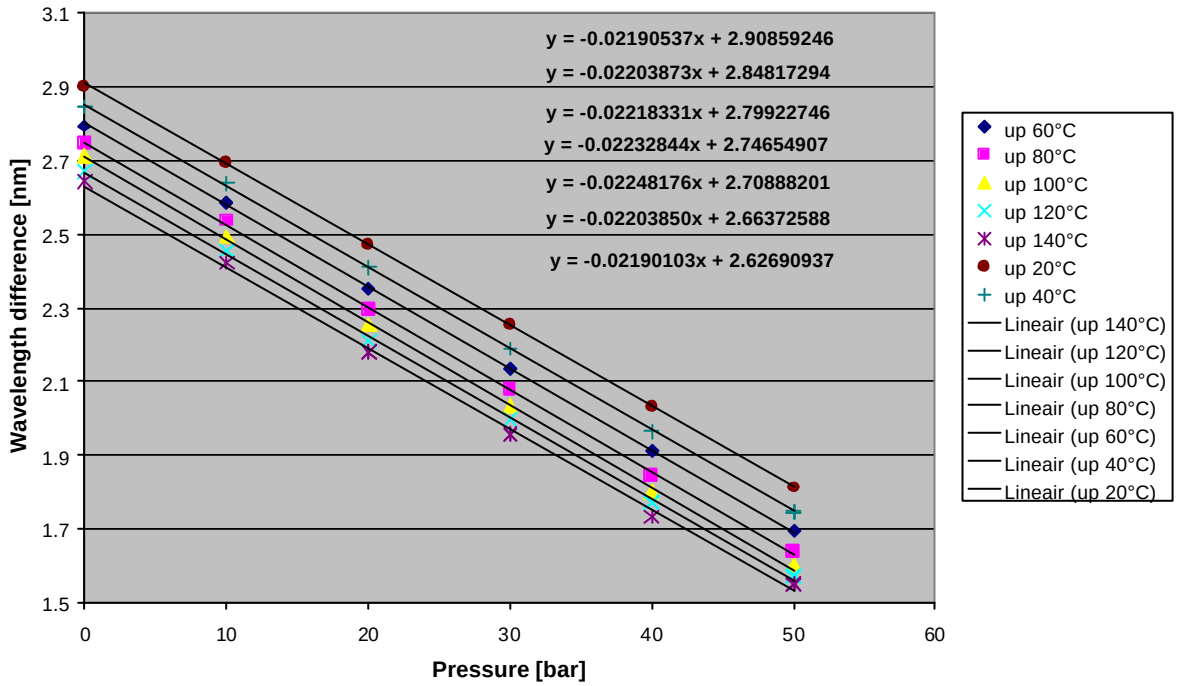

Fig. 1.26: Total calibration sheet of the titanium pore water pressure sensor

A =	7071945.848462790
B =	-9224.58742386890
C =	3.008168352978150
D =	45.16542223024020

Table 1.3: Results of simplex calculation for titanium pore water pressure cell.

1.5.3. Calibration setup

As has been discussed in the previous paragraph, the pressure calibration needs to be performed at different temperatures in order to be able to take the effects of the thermal expansion of the housing into account.

The calibration set-up is show in Fig. 1.27. The sensor is put into a temperature chamber and is connected to a hand oil pump using a standard tube. Through the tube it's possible to create oil pressure on the membrane of the pore water pressure sensor. This calibration set-up makes it possible to perform different pressure calibrations at different temperatures.

The set-up has the advantage that it's possible to calibrate different pressure sensors at the same time by putting them in a parallel on the standard tube of the hand oil pump.

Fig. 1.27: Calibration set-up, pore water pressure sensor

1.6. Total pressure sensor

A new design for the total pressure sensor has been build. The sensor is designed for measuring pressures up to 150 bar at temperatures up to 180°C. The total pressure sensor cell has the same design as the pore water pressure sensor. The only difference is the connection of the membrane with an oil filled pressure plate that is transferring the load on the pressure plate to the membrane. So each pore water pressure sensor has the capability to be transformed to a total pressure sensor.

A new element on this sensor is the design of the oil filled pressure plate, and how to fill it with hydraulic oil.

1.6.1. Sensor design

Fig. 1.28 shows the dimensions of the total pressure sensor. As can be observed, the total pressure sensor has the same design as the pore water pressure sensor. The oil filled pressure plate is just an extra component.

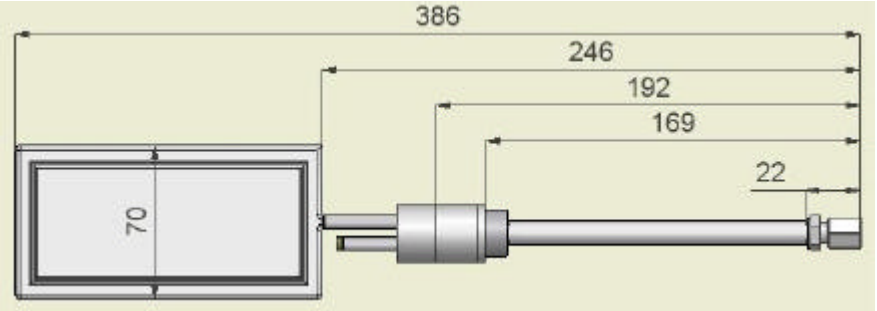

Fig. 1.28: Dimensions of a total pressure sensor

The pressure plate exists of 2 stainless steel (or titanium) plates that are welded to each other. A little gap between the two plates need to be foreseen. This gap will be filled with hydraulic oil which is used to transmit the pressure on the pressure plate to the surface of the membrane. Fig. 1.29 shows a photo of the pressure plate.

Fig. 1.29: Photo of the pressure plate

When filling the pressure plate with oil, it is very important that there are no air-bubbles in the plate. An air-bubble will cause a perforation of the oil pad at high pressures. This will damage the oil pad and the measurements.

In order to obtain this, a special set-up and procedure has been used. Fig. 1.30 shows the set-up for filling the oil pad. The pressure plate is first mounted on the membrane and is then connected to the oil pad connection using the short filling tube (see Fig. 1.28). From then on the following procedure will be repeated several times:

1. Making pressure plate vacuum using a vacuum pump
2. Connect pressure plate to oil hand pump by opening valve
3. Pump oil into pressure plate using the oil hand pump
4. Let escape the air-bubbles

This procedures takes more or less 4 hours to fill the oil pad correctly. At the end of this process, an internal pressure of +/- 1.4 bar will be maintained. This will guarantee the well functioning of the oil pad.

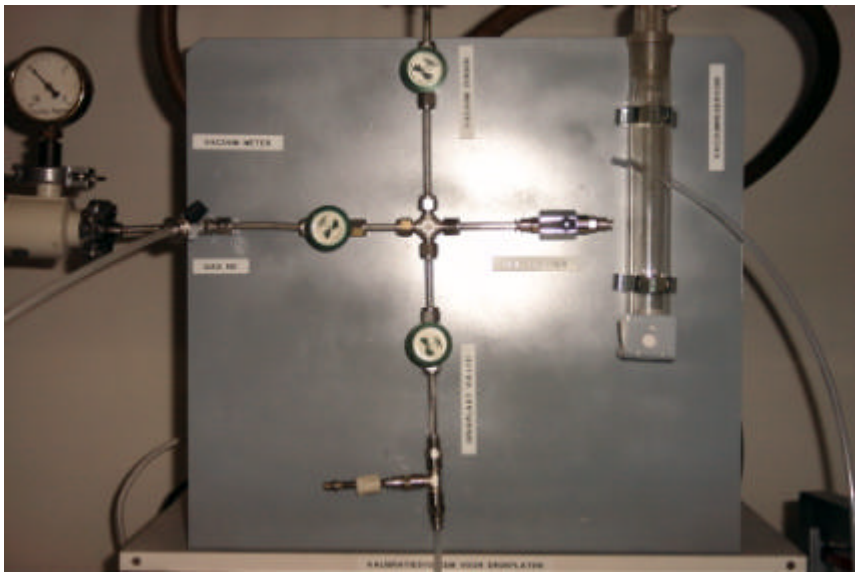

Fig. 1.30: Set-up for filling the pressure plate with hydraulic oil.

1.6.2. Calibration method

The calibration method is identical to this from the pore water pressure sensor. Fig. 1.31 shows the wavelength difference for P=0 bar at different temperatures for a 150 bar stainless steel total pressure sensor. As can be observed, the wavelength difference shows also a parabolic dependence as function of the temperature. This can also be explained by the thermal expansion of the housing.

Fig. 1.32 shows the pressure calibration curves at different temperatures. Again, a good linear behaviour can be found with a similar slope at the different temperatures. As a consequence, a similar calibration method as with the pore water pressure sensor can be used. Table 1.4 shows the results of the simplex method applied on the data in Fig. 1.32. With these parameters a mean deviation of 0.44 % full scale is obtained.

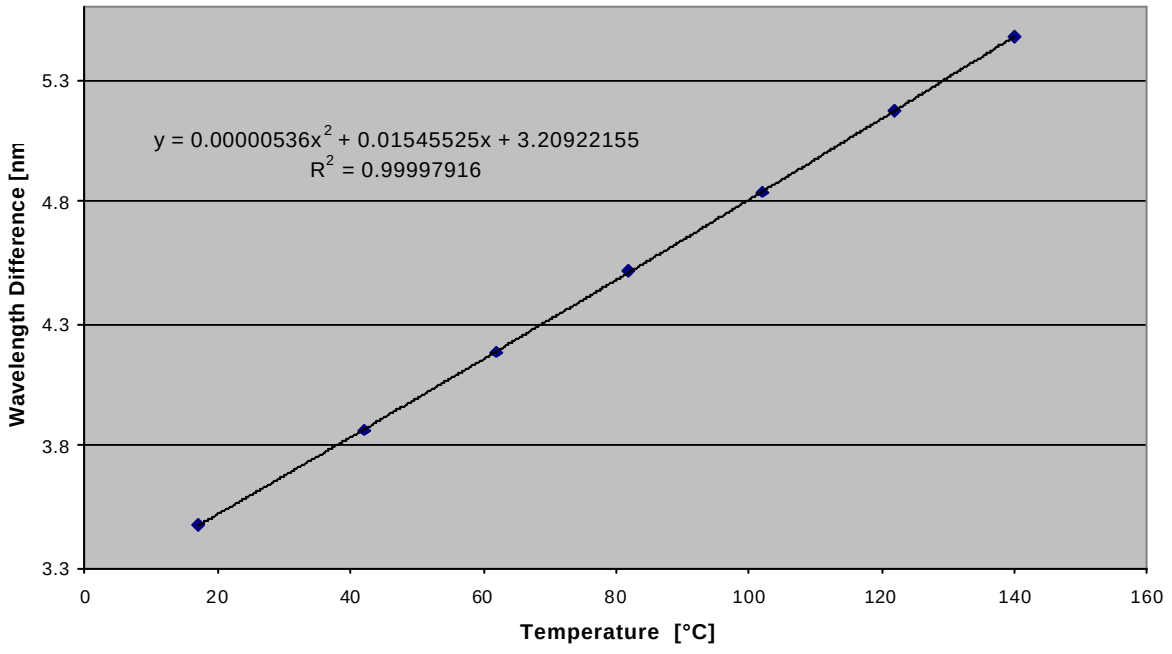

Fig. 1.31: Wavelength difference of a stainless steel total pressure cell at P=0 bar, measured at different temperatures.

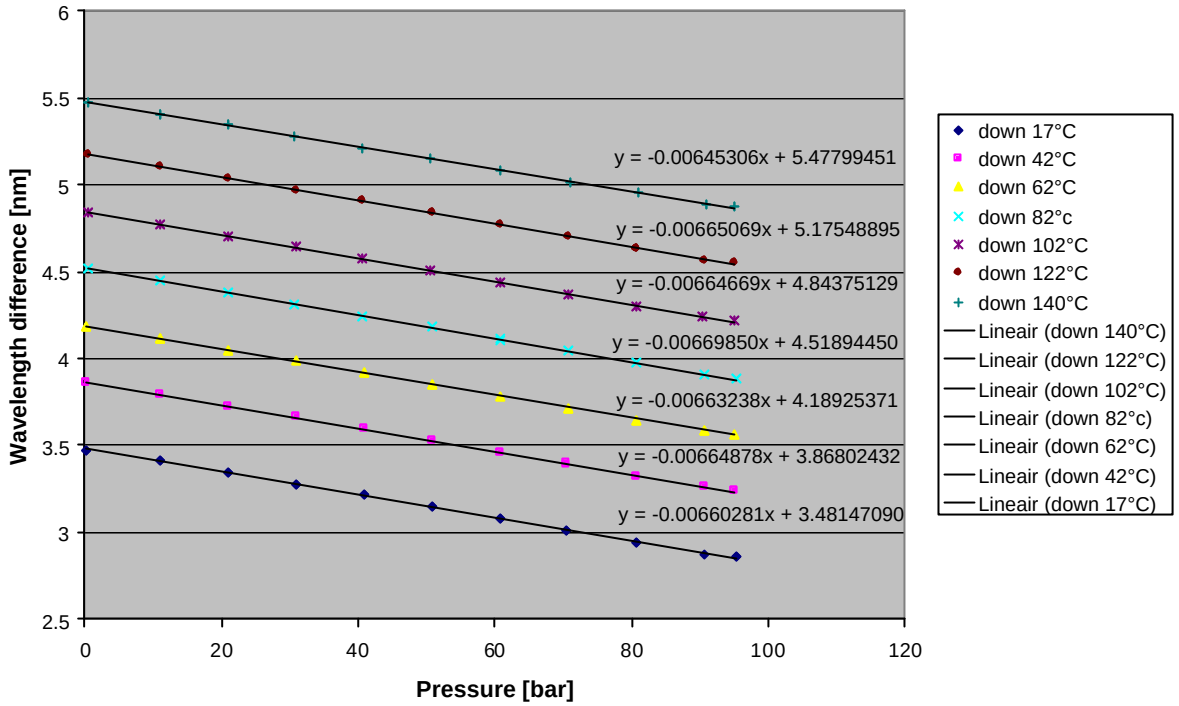

Fig. 1.32: Total calibration sheet of the stainless steel total pressure sensor

A =	12789595.85721270
B =	-16918.72122018680
C =	5.594596003284880
D =	151.0805170665950

Table 1.4: Results of simplex calculation for stainless steel total pressure cell.

Finally, the results of a 150 bar Titanium total pressure sensor will be discussed. Fig. 1.33 shows the wavelength difference for P=0 bar at different temperatures for a 150 bar titanium total pressure sensor. As can be observed, the wavelength difference shows also a parabolic dependence as function of the temperature. This can also be explained by the thermal expansion of the housing.

Fig. 1.34 shows the pressure calibration curves at different temperatures. Again, a good linear behaviour can be found with a similar slope at the different temperatures. As a consequence, a similar calibration method as with the pore water pressure sensor can be used. Table 1.5 shows the results of the simplex method applied on the data in Fig. 1.34. With these constants a mean deviation, of 1.2% full scale is obtained.

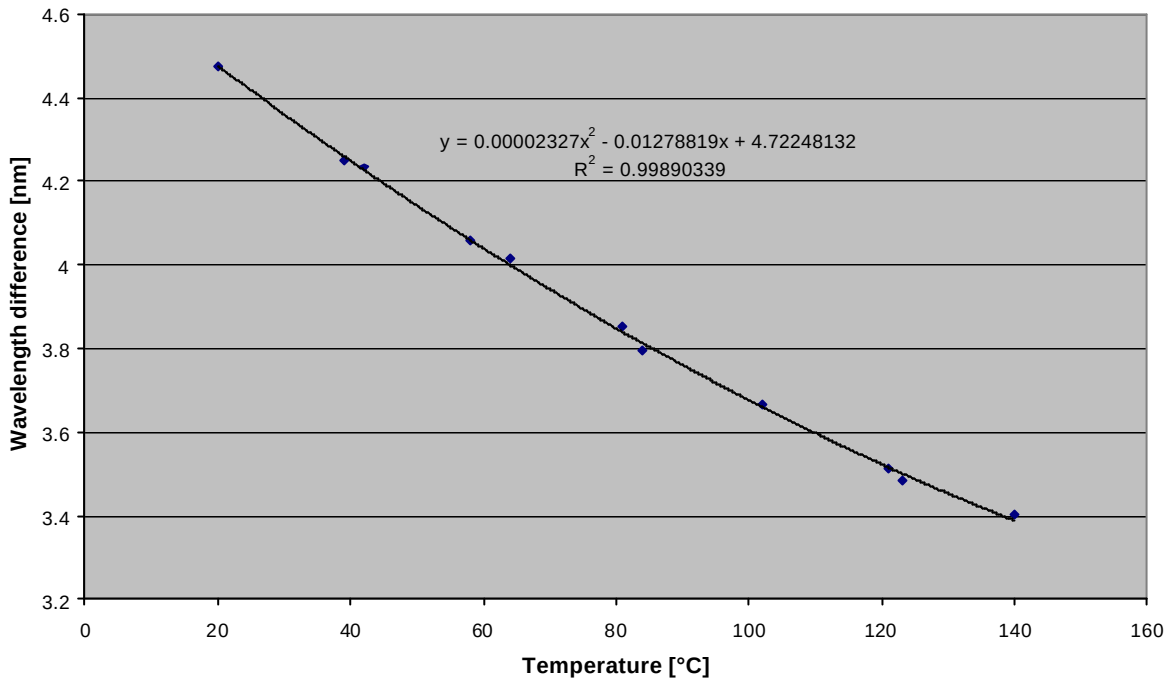

Fig. 1.33: Wavelength diff. of a titanium total pressure cell at P=0 bar, measured at different temperatures.

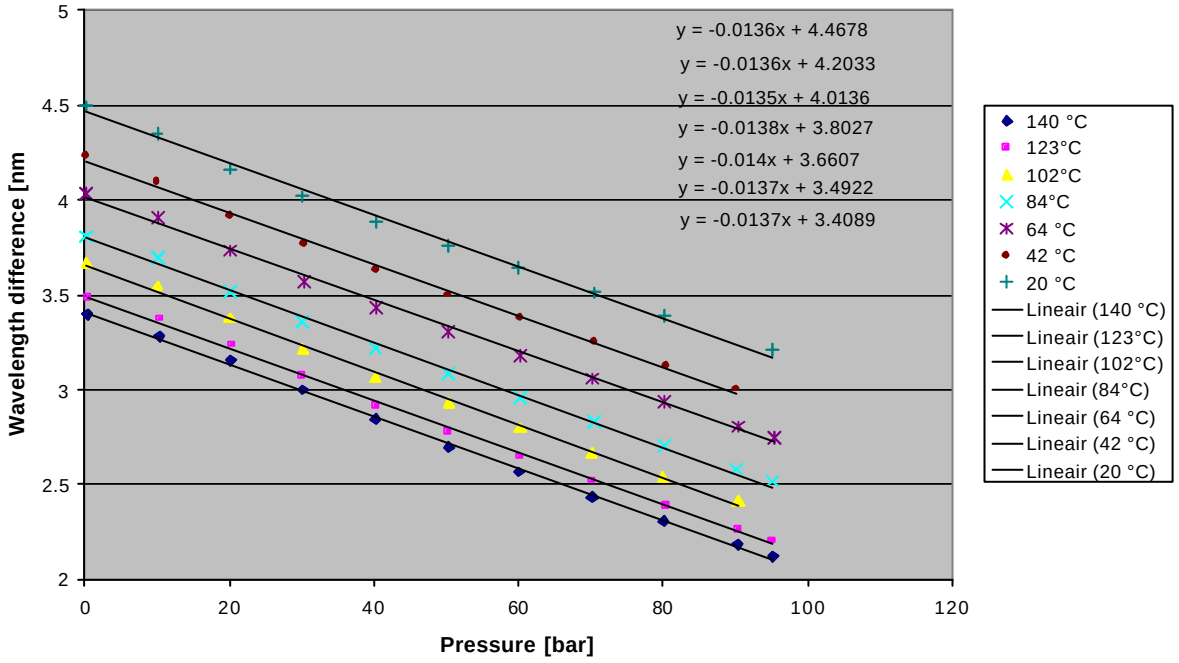

Fig. 1.34: Total calibration sheet of the titanium total pressure sensor

A =	39226446.8655982
B =	-50821.908817283
C =	16.4613461509393
D =	72.3472668810292

Table 1.5: Results of simplex calculation for titanium total pressure cell.

1.6.3. Calibration set-up

In order to calibrate the total pressure cell a barrel with a double wall is used, see Fig. 1.35, in which the total pressure sensor can be positioned. The barrel is filled with oil that can be put under pressure using an automatic pressure pump, see Fig. 1.36. The temperature is controlled by circulating oil on the desired temperature through the double wall. The oil is heated using a heating bath of the type 'Haake F3', see Fig. 1.37. The temperature in the barrel is measured using a PT-100 sensor. As a consequence, it is possible with this set-up to establish the desired pressure and temperature into the barrel.

Fig. 1.35: Barrel with double wall

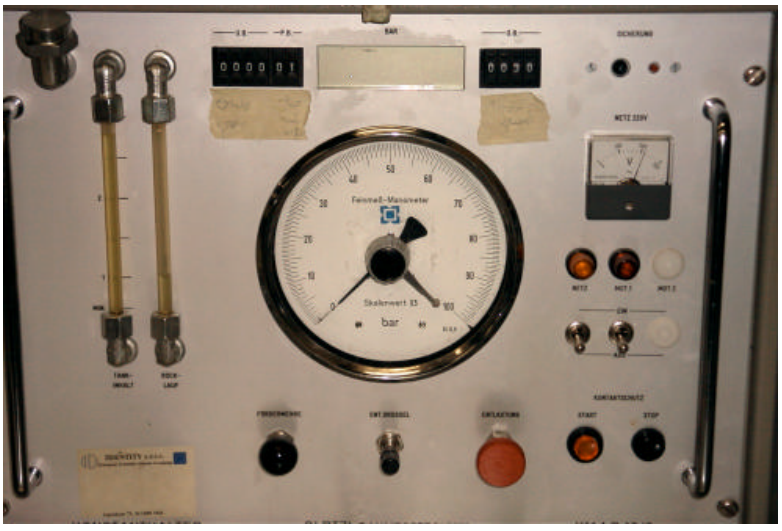

Fig. 1.36: Automatic pressure pump

Fig. 1.37: Heating bath 'Haake F3'

1.7. Series configuration design for pressure sensors

The problem with the pressure cell design is that the fibre can not pass trough the sensor due to the presence of the membrane. The fibre enters the pressure sensor at one side and is stopped just before the membrane. The only way to obtain a series configuration is turning the fibre over 180°C such that the fibre can leave the sensor along the same way as it enters the sensor. This design is shown in Fig. 1.38. There is one major problem with this solution. Due to the strong bend that the fibre needs to make (radius 8 mm) the losses of the standard SMF28 fibres become too much such that no signal can be detected anymore. The maximum bend radius of a standard SMF28 fibre is around 2 cm which is much higher than the available bend radius.

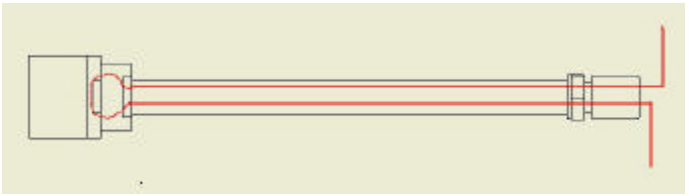

Fig. 1.38: Fibre path for establishing series configuration.

In order to solve this problem, tests have been performed using a special fibre from StockerYale: BIF-1550-L2. This fibre is a bend insensitive fibre (< 0.01 dB loss for 30 loops with 6mm radius). A serial configuration has been build using this fibre after splicing the fibre to a standard fibre containing the gratings. Fig. 1.39 shows a photo of the serial configuration. No significant losses have been observed with this set-up and a proper functioning of the sensors could be established.

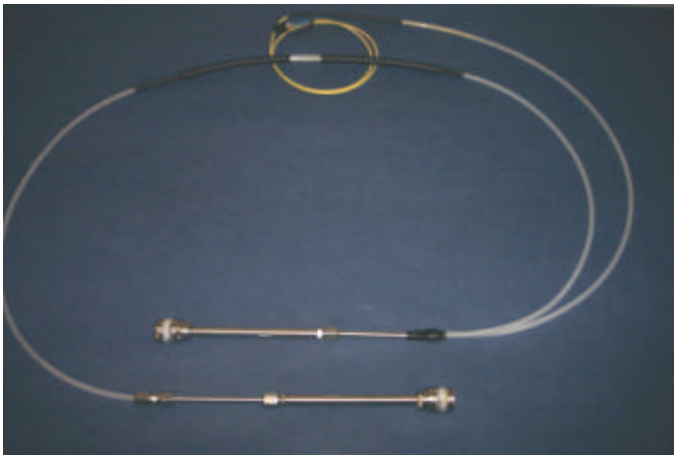

Fig. 1.39: Serial configuration of two pore water pressure sensors

1.8. Humidity sensor

1.8.1. State at the beginning of the project

The design of the hydrogel sensor is shown in Fig. 1.40. The sensor consists of a stainless steel tube, which has at one end a hydrogel film. At each end side of the tube, a mechanism is foreseen to fix a capillary. Between both capillaries a FBG is stretched. When the hydrogel film comes into contact with high humidity levels, the film will swell and an elongation of the fibre occurs. This results in an increase of the strain on the FBG, what results into a wavelength shift:

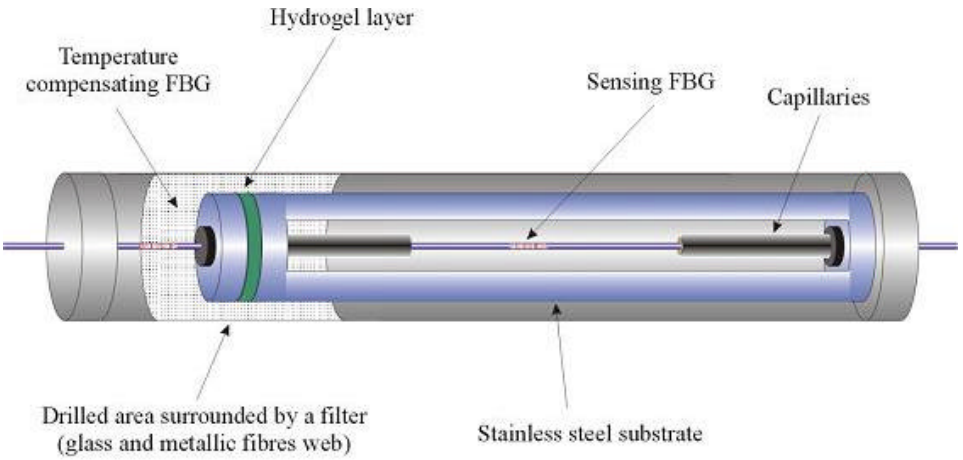

Fig. 1.40: Design of humidity sensor

The temperature effects of the strained grating are compensated using a second FBG which remains in an unstressed condition. However, this compensation does only take into account the intrinsic temperature sensitivity of the FBG but does not take into account the effect of the thermal expansion of the sensor housing.

During the project, the hydrogel has further been characterised. The complete temperature behaviour has been analysed. A new interpretation method is proposed that does take into account the thermal expansion of the housing. Furthermore, the influence of pH levels, salt solutions and radioactive radiation has been analysed.

1.8.2. Total temperature compensation

So far, no thermal expansion effect had been taken into account when looking to the response of the different wavelengths. Nevertheless, a significant influence can be expected. Therefore, a new calibration method needs to be used that does take into account this thermal expansion. The method will be indicated by 'Total Temperature Compensation'.

In order to examine the influence of the thermal expansion on the wavelength response, the wavelengths was measured for different temperatures between 0°C and 60°C at a constant humidity level of 50%. Fig. 1.41 and Fig. 1.42 show the results of the temperature calibration for the temperature compensating FBG and the stressed FBG. For both FBG's a linear wavelength response as function of temperature has been found. The slope of this linear relation of the temperature compensating FBG is in very good correspondence with the theoretical value given by the FBG supplier: 9.8 pm/°C. However, the slope of the stressed FBG is much higher, around 26.7 pm/°C. This is 16.9 pm/°C more then expected. It will be shown that this deviation is caused by the thermal expansion of the housing.

The experimental deviation corresponds to a strain influence of:

$$S = \frac{d(\Delta l)/dT}{b} = \frac{16{,}995\frac{pm}{°C}}{1{,}2\frac{pm}{\mu e}} = 14{,}1625\frac{\mu e}{°C} \qquad (1.10)$$

with b the strain sensitivity of the FBG. Taking into account the distance between the two capillaries (free fibre length) of 40 mm, this strain sensitivity corresponds to a elongation ΔL of the stressed fibre equal to:

$$\Delta L = 5{,}666 \times 10^{-4}\frac{mm}{°C} \qquad (1.11)$$

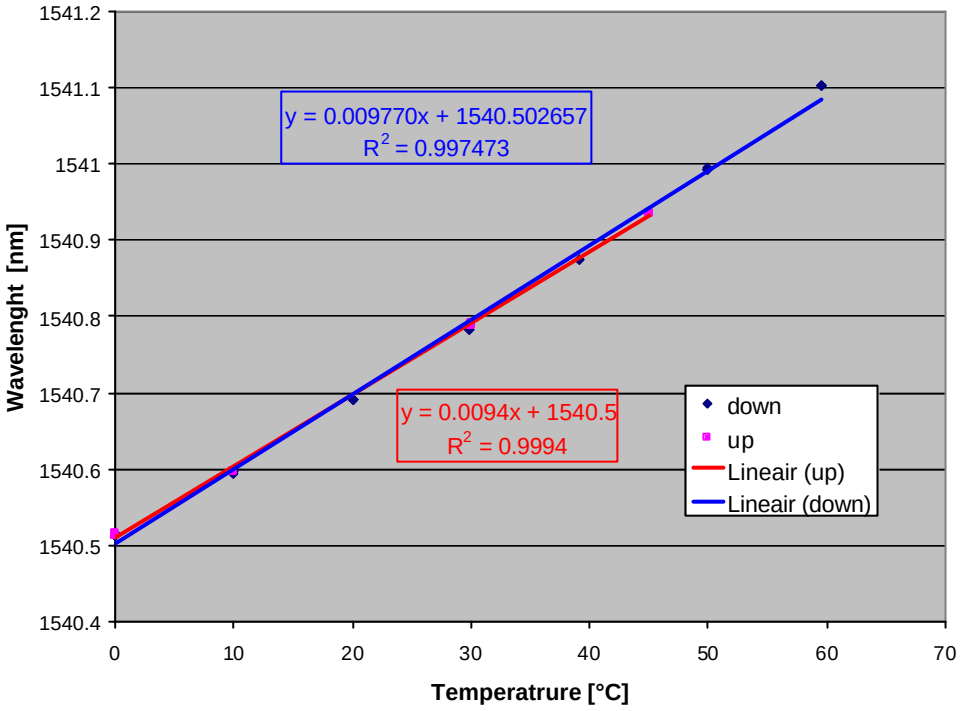

Fig. 1.41: Temperature calibration of temperature compensating FBG.

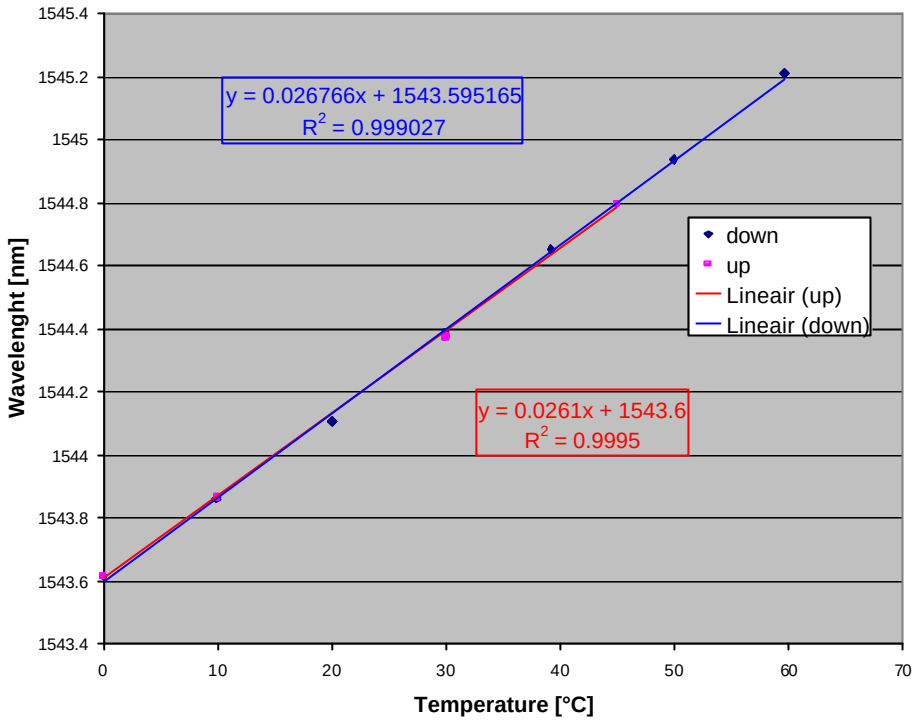

Fig. 1.42: Temperature calibration of stressed FBG.

This experimental value can be compared to the theoretical expected value. Fig. 1.43 shows the schematic representation of the thermal expansion of the housing. Due to the increasing temperature, the capillaries as well as the inner stainless steel tube will elongate resulting in a net elongation of the stressed fibre of:

$$\Delta L = \Delta L_1 - \Delta L_2 - \Delta L_3 = L_1 \cdot \alpha_{SS} - (L_2 + L_3) \cdot \alpha_{cap} \qquad (1.12)$$

with ΔL_1 the elongation of the inner tube between the two capillary fixation points, ΔL_2 and ΔL_3 the elongation of the capillaries starting from the fixation point, α_{ss} and α_{cap} the thermal expansion coefficients of the inner tube and the capillaries. For the current sensor, L_1=140 mm, L_2=L_3=50 mm, α_{cap} = 16 x 10^{-6} and α_{ss} = 16.5 x 10^{-6}. Based on these data, the expected elongation can be calculated:

$$\Delta L = 140 \cdot 16{,}5 \times 10^{-6} - (100) \cdot 16 \times 10^{-6} = 7{,}1 \times 10^{-4} \frac{mm}{°C} \qquad (1.13)$$

As can be observed, a good correspondence with the experimental results is obtained. The small difference that does exist might be caused by the fact that the capillaries are filled with glue, influencing the thermal expansion of these capillaries.

It can be concluded that the influence of the thermal expansion of the housing does induce a significant effect on the response of the hydrogel sensor. Therefore, a new method is proposed to interpret the results of the hydrogel sensor. In future, the temperature sensitivity of the temperature FBG (S_T) and the stressed FBG (S_S) will be measured at low humidity level (ex. 50%). The total temperature compensated sensor response can then be given by:

$$\text{Response} = \Delta(\lambda_S - \frac{S_S}{S_T}.\lambda_T) \qquad (1.14)$$

With λ_S the wavelength of the stressed FBG

λ_T the wavelength of the temperature compensating FBG

This response does take into account the thermal expansion of the housing and will only be influenced by changes in humidity level.

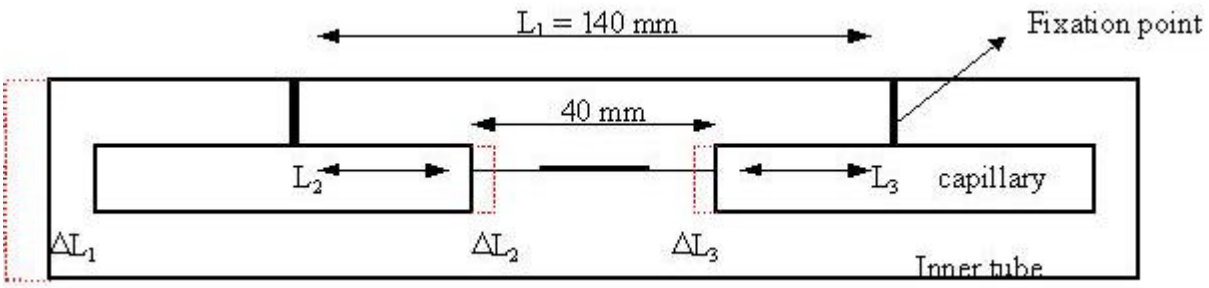

Fig. 1.43: Schematic representation of thermal expansion.

1.8.3. Influence pH-level

The influence of the pH-level of the fluid that comes into contact with the hydrogel film has been investigated. Two pH levels have been tested: pH 2 and pH 8. Fig. 1.44 shows the sensor responses for pH 2 and pH 8 solution. The sensors have been put for 1 day into the solution after which they where taking out the solution for drying during another 3 days. It can be observed that both responses do show a similar behaviour. The sensors also do show a hysteresis effect after drying but this is also present for normal pH levels. It can therefore be concluded that the humidity sensor is reacting very well on solutions with a pH level of 2 and 8.

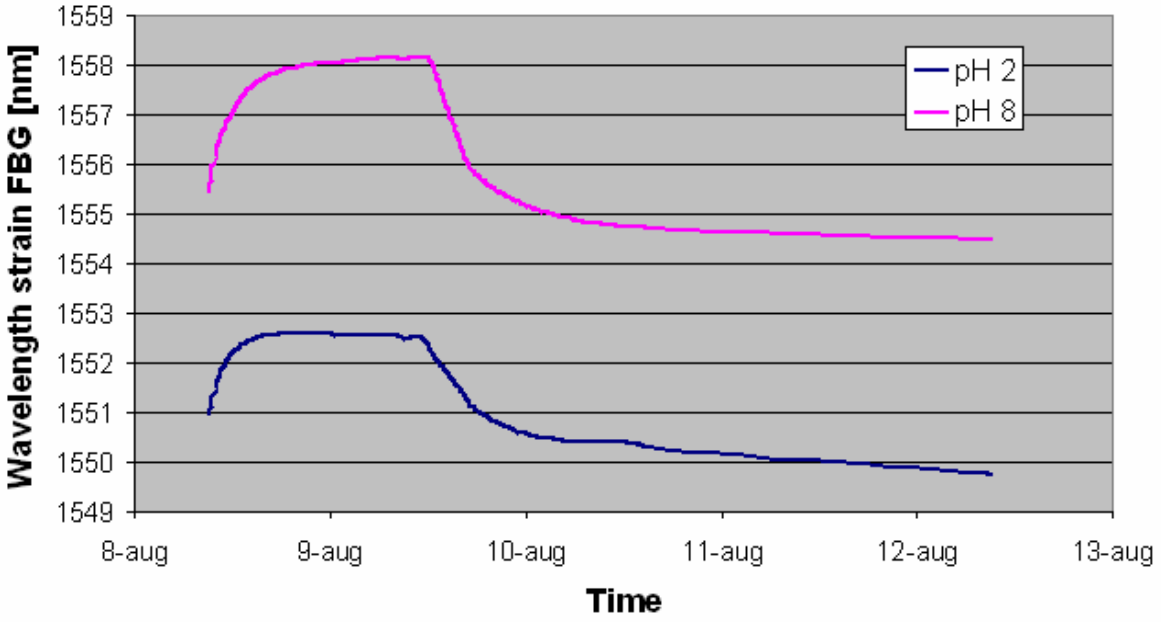

Fig. 1.44: Influence of pH level on humidity sensor response

1.8.4. Response in salt water environment

The response of the hydrogel sensor in a salt environment has been investigated. A hydrogel sensor containing 3 hydrogel films had been fabricated. The sensor was put into a salt solution coming from the Morsleben repository. The test set-up and results are shown in Fig. 1.45. As can be seen, a good response does occur. An increase in wavelength difference from 2.2 to 4 nm has been observed. Nevertheless, the sensor does show a high hysteresis

for the salt solution. After drying the sensor, the wavelength was even increased up to a level of 5.5 nm. This can possibly be attributed to the crystallisation of the salt in the hydrogel films, causing additional strain on the FBG. The water leakage sensor is as a consequence only a 1 way sensor in this environment.

Fig. 1.45: Test set-up water leakage sensor in salt solution.

1.8.5. Influence of radioactive radiation

The influence of radioactive radiation on the hydrogel film has been analysed. Two hydrogel films where radiated with γ-radiation: the first sensor with a dose of 100 GY and the second with a dose of 1 KGY. After the radiation, the sensor was mounted into a hydrogel sensor and analysed into a climatic chamber. The humidity was initially set at 50%. After stabilising, the humidity level was increased with a slope 0.02%/min up to a final level of 95%. This value was fixed for one day after which the initial value of 50% was reset. Fig. 1.46 (100 GY) and Fig. 1.47 (1KGY) do show the responses of the sensors together with the applied humidity level. It can be observed that both sensors start reacting at a humidity level around 80%. Furthermore, the signal stabilises very slowly at a humidity level of 95% and a hysteresis effect can be observed when going back to the initial humidity value of 50%. This behaviour is quite similar as with the non-radiated hydrogel films. It can therefore be concluded that the radiation with a dose lower or equal to 1 KGY does not show a significant effect on the response of the hydrogel film.

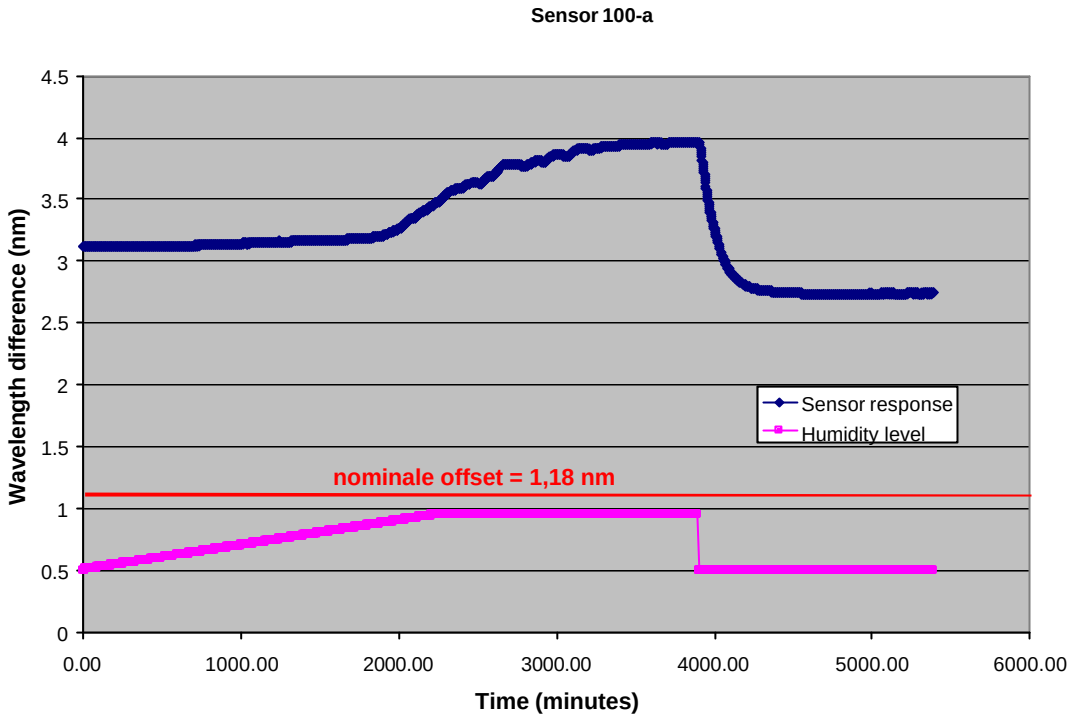

Fig. 1.46: Response humidity sensor after radiation of 100 GY

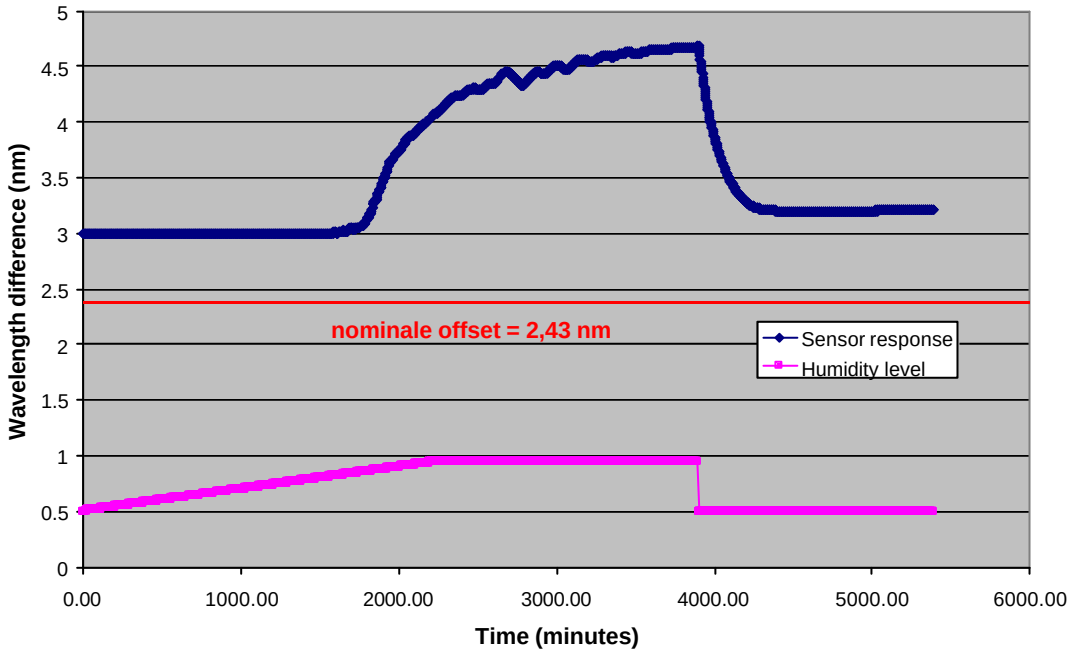

Fig. 1.47: Response humidity sensor after radiation of 1 KGY

1.9. Hydrogen sensor

1.9.1. Basic theory

The metal-hydrogen system consists of a metallic material, hydrogen gas, and an interface region between them (see Fig. 1.48).

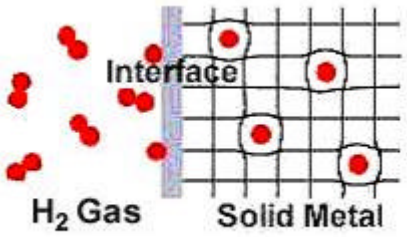

Fig. 1.48: Simplified Model of Metal-Hydrogen Interaction

Hydrogen gas adsorbs onto the interface region. At the interface, the molecule is dissociated into individual hydrogen atoms that are able to absorb or dissolve into the metal phase. The random dissolution of hydrogen atoms in the metal phase is known as the α-phase. Within the metallic phase, the hydrogen atoms can start to arrange themselves in a specific configuration with the metal atoms, forming the metal hydride phase, called the β-phase. Where and how the β-phase is nucleated and grows is a characteristic of the material.

The reaction of hydrogen with a metal can be written as a chemical reaction:

$$M + x/2\ H2 \longleftrightarrow MHx + Heat \qquad (1.15)$$

The double arrow indicates that the reaction is reversible and exists as an equilibrium state. In other words, by changing conditions, the reaction can be made to go in either the forward or reverse direction. The heat on the right-hand side indicates that heat or energy is released when the metal hydride is formed, and thus, heat must be put in to release hydrogen from the metal hydride phase. The heat is the enthalpy (heat of formation) of the reaction and is an indication of the strength of the metal-hydrogen bond in the metal hydride phase.

The equilibrium between hydrogen and metals is best described by a Pressure – Composition – Isotherm plot, called a “PCT” curve. Idealised PCT curves are shown in Fig. 1.49.

The sloping part on the left side of the PCT curves shows that when only the α-phase is present, large changes in hydrogen pressure only slightly change the concentration of dissolved hydrogen within the metal matrix. However once nucleation of the β-phase starts and both the α and β-phases exist simultaneously, a large increase in the hydrogen concentration within the metal matrix occurs over a very small change in hydrogen pressure. Once the material has become saturated with the β-phase, again only slight hydrogen uptake occurs with large changes in hydrogen pressure. The flat region, which is characteristic of the coexistence of two phases in equilibrium, is called the equilibrium plateau pressure and is a characteristic of the material. Also note that at higher temperatures, it takes higher hydrogen pressures to cause the large uptake of hydrogen gas.

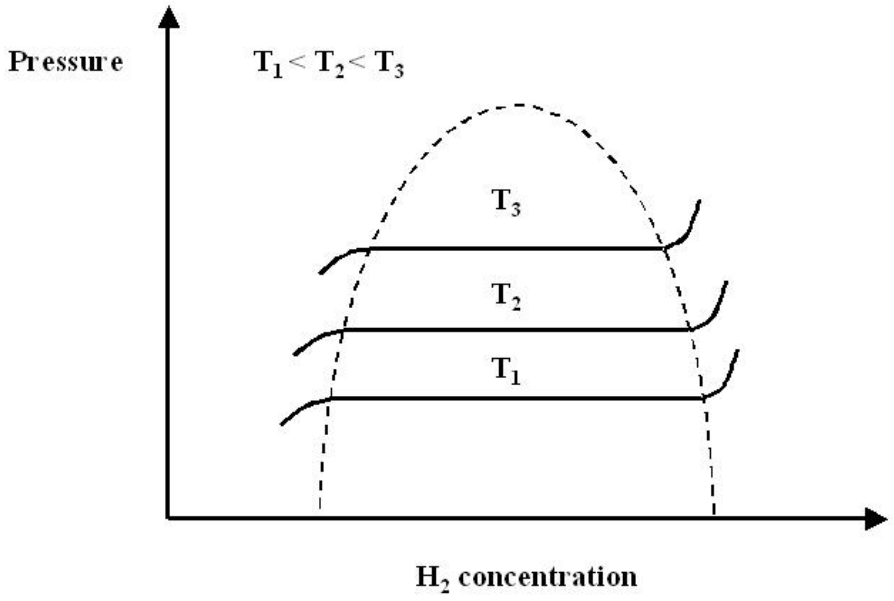

Fig. 1.49: Idealised PCT Curves for 3 Temperatures

The Palladium-hydrogen system has the property that at normal temperature, palladium can absorb up to 900 times its own volume of hydrogen. This absorption is accompanied by extensive plastic deformation of the metal, but without mechanical or chemical disintegration.

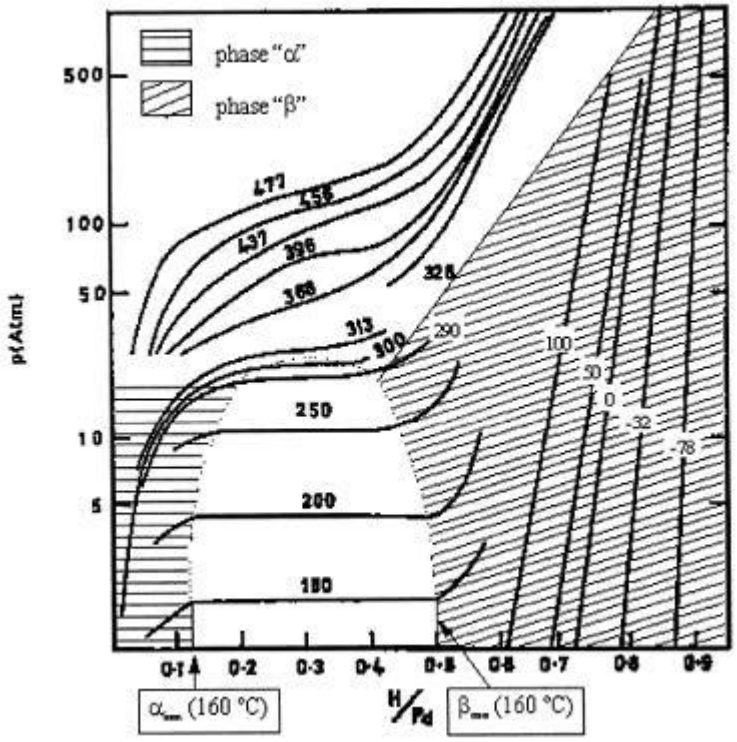

Fig. 1.50: 'Pressure-composition' isotherms of palladium versus the adsorption of hydrogen.

Fig. 1.50 shows the Pressure-Composition isotherms of Palladium versus the absorption of molecular hydrogen [1]. For each isotherm corresponding to temperature lower than 300°C, one can find two different phases separated by an iso-pressure zone. For temperatures higher than 300°C, the iso-pressure zone disappears and the coexistence of the two phases is no more possible. Without hydrogen, palladium is in the α phase whatever the

temperature. At room temperature the hydration of palladium leads quickly to the β phase. Experimental results reported by Bévenot et al. [2] show that the equilibrium plateau pressure is located between the 15 and 20 mbar hydrogen. As a consequence, a low sensor response is expected for hydrogen pressures lower than 15 mbar. A strong sensor response can be observed for pressures between 15 and 20 mbar. An additional increase of hydrogen above this 20 mbar results in small changes in hydrogen content.

It has been shown by Mueller et al. [3] that at low (< 200 Pa) hydrogen pressures and normal laboratory temperature (295 K), the strain in the Pd is given by:

$$\varepsilon_P = e \,.\, \mathrm{sqrt}(P) \qquad (1.16)$$

with $e = 8.5 \bullet 10^{-6}$ and P the pressure expressed in Pa. Furthermore, it is also known that the β-phase has the same faced centred cubic symmetry of pure Pd but with a lattice parameter increasing of up to 3.5 %.

Studies by Eriksson et al. [4] demonstrate that a CO exposure of a hydrogen covered Pd surface can yield a simultaneous desorption and absorption of adsorbed hydrogen. There is a repulsive interaction between adsorbed CO and hydrogen. The induced absorption can as a consequence give the falls impression that the hydrogen concentration has increased. This process is strongly dependent on the CO exposure and temperature. The CO induced hydrogen dissolution is only observed when the conditions are such that the CO adsorption rate is higher than the hydrogen desorption rate. This can be understood since steady state conditions are obtained faster between the bulk and the surface than between the surface and the gas phase, simply because desorption involves a desorption energy of around 0.9 eV (per molecule), while the energy barrier between the surface and the bulk may be as low as 0.4 eV (per atom). Thus, if the CO adsorption rate is large compared to the hydrogen desorption rate, a temporary increase in the local surface hydrogen coverage may be obtained, leading to an increased hydrogen concentration also in the Pd bulk. If on the other hand the CO adsorption rate is low, the bulk concentration will have time to adjust the gas phase condition.

Furthermore, it is also observed that for high CO coverages (higher than around 0.3 Mono-Layers) hydrogen dissociation and desorption will totally be blocked [5]. This may result in a hydrogen disclosure wherein the CO acts as a barrier between hydrogen in the gas phase and hydrogen dissolved in Pd. In this case, the sensor is ‘dead’.

It is also shown by Eriksson et al. [5] that high CO coverage’s on the Pd surface, do increase the time needed to obtain equilibrium between the gas phase hydrogen pressure and the response of the Pd device. Fig. 1.51 shows the hydrogen response of a Pd based hydrogen sensor (a Pd-MOS device) with and without the presence of CO. It can be observed that the adsorption as well as the desorption response is much slower in the presence of CO. In order to investigate this in detail a new term is introduced: the impeding factor. This factor is the ratio of the slope of the response without the presence of CO on the slope of the response with the presence of CO. The impeding factor is by definition equal to 1 at zero CO coverage. The impeding factor is experimentally defined for different CO coverage’s. This result is shown in the insert of Fig. 1.51. It can be observed that the impeding factor is very small below CO coverage’s of 0.2 ML, while it increases exponentially above this coverage. This strong increase can not be explained by site blocking by the CO molecules but is due to an increase of the activation energy for hydrogen dissociation and hydrogen desorption with increasing CO coverage.

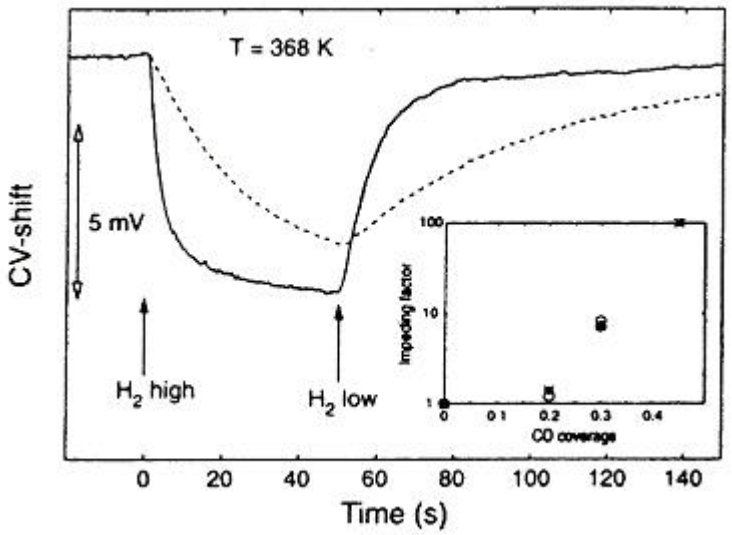

Fig. 1.51: Sensor response at 368K for a hydrogen pressure pulse between t=0 and t=50 s, in the absence (full line) and presence (dashed line) of CO. The insert shows the impeding factor as a function of CO coverage for hydrogen adsorption (*) and desorption (o).

The results described here are not in complete agreement with previous published articles. Kiskinova and Bliznakov argued that a Pd (111) surface saturated with CO (coverage = 0.6 ML) is still capable of dissolving hydrogen relatively easily [6]. Kok et al. [7] at the other hand showed that already at lower CO coverage's the Pd surface is almost incapable of dissolving hydrogen. Ratajczykowa [8] observed that at a CO coverage of 0.33 ML, the hydrogen dissolution rate was not affected by the adsorbed CO, while the desorption rate of dissolved hydrogen was strongly reduced. The reason for these anomalies is not clear at this moment.

1.9.2. Hydrogen sensor design

Two sensor designs were developed and tested. They will further be indicated as Sensor I and Sensor II.

The design of sensor I is shown in Fig. 1.52. The sensor consists of a stainless steel tube, which has at one end a Palladium disc. At each end side of the tube, a mechanism is foreseen to fix a capillary. Between both capillaries a FBG is stretched. When the Palladium disc absorbs hydrogen, the disc will swell and an elongation of the tube occurs. This results in an increase of the strain on the FBG, which gives at his turn a wavelength shift of:

$$\Delta\lambda = 1.2 \bullet 10^{6} \,.\, \varepsilon_P(P_{H2})\, th_{Palladium} / L_{FBG} \qquad (1.17)$$

With $\Delta\lambda$ the wavelength shift in [pm]; $\varepsilon_P(P_{H2})$, the strain on the Palladium material caused by the hydrogen pressure P_{H2}; $th_{Palladium}$, the thickness of the Palladium disc; L_{FBG} , the length of the fibre hosting the stretched FBG.

The sensitivity and dynamic range of the hydrogen sensor can be applied by choosing the thickness of the Palladium disc or the length of the stretched FBG.

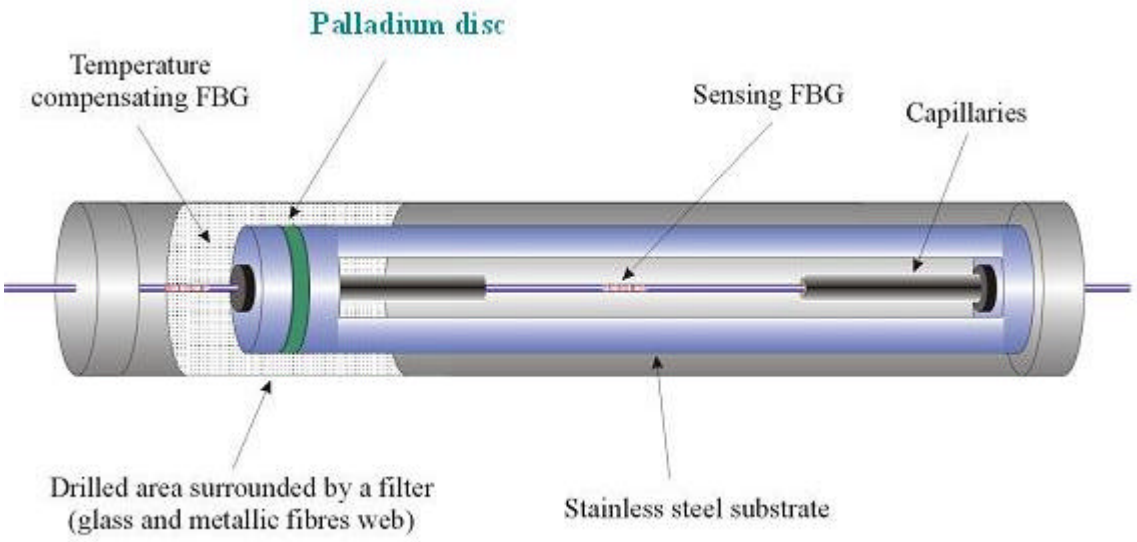

Fig. 1.52: Prototype design of Hydrogen sensor I

A picture of the different parts of the sensor is shown in Fig. 1.53. The Palladium disc has a thickness of 0.5 mm and the length of the fibre hosting the FBG is equal to 45 mm. As a consequence, the wavelength shift due to hydrogen presence is given by:

$$\Delta\lambda = 1{,}2 \cdot 10^{6} \cdot \varepsilon_{P}(P_{H2}) \cdot (1/90) \qquad (1.18)$$

It needs also to be mentioned that temperature effects of the grating are compensated using a second FBG which remains in an unstressed condition. However, this compensation does not take into account the effect of the sensor housing since the distance between both capillaries is also influenced by the thermal expansion coefficient of this housing. Therefore, a similar compensation method as with the humidity sensor was applied. The sensor has been put in a climatic chamber and the wavelengths have been recorded for different temperatures. The wavelength response of the temperature and stressed FBG is shown in Fig. 1.54 and Fig. 1.55. As can be seen, the stressed FBG is much more sensitive compared to the temperature FBG.

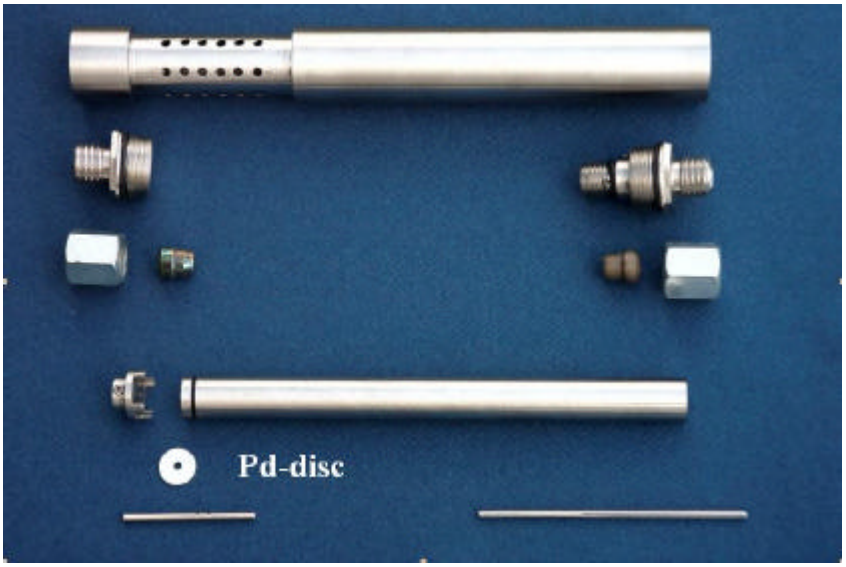

Fig. 1.53: Different parts of the Hydrogen sensor

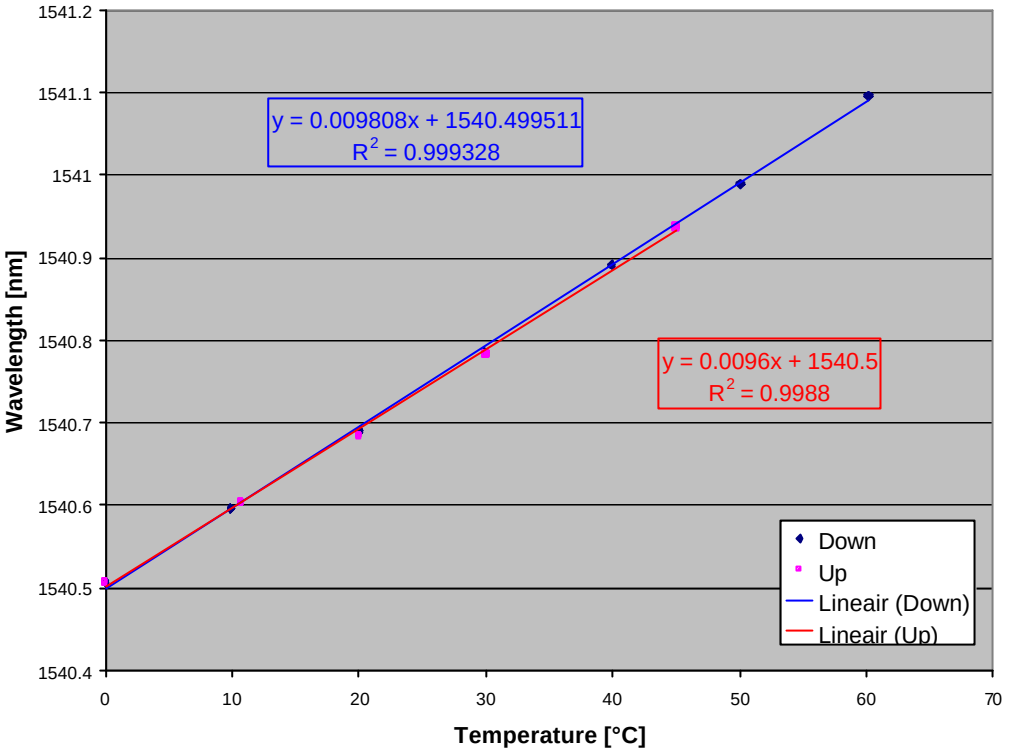

Fig. 1.54: Temperature calibration of the temperature compensating FBG of hydrogen sensor I.

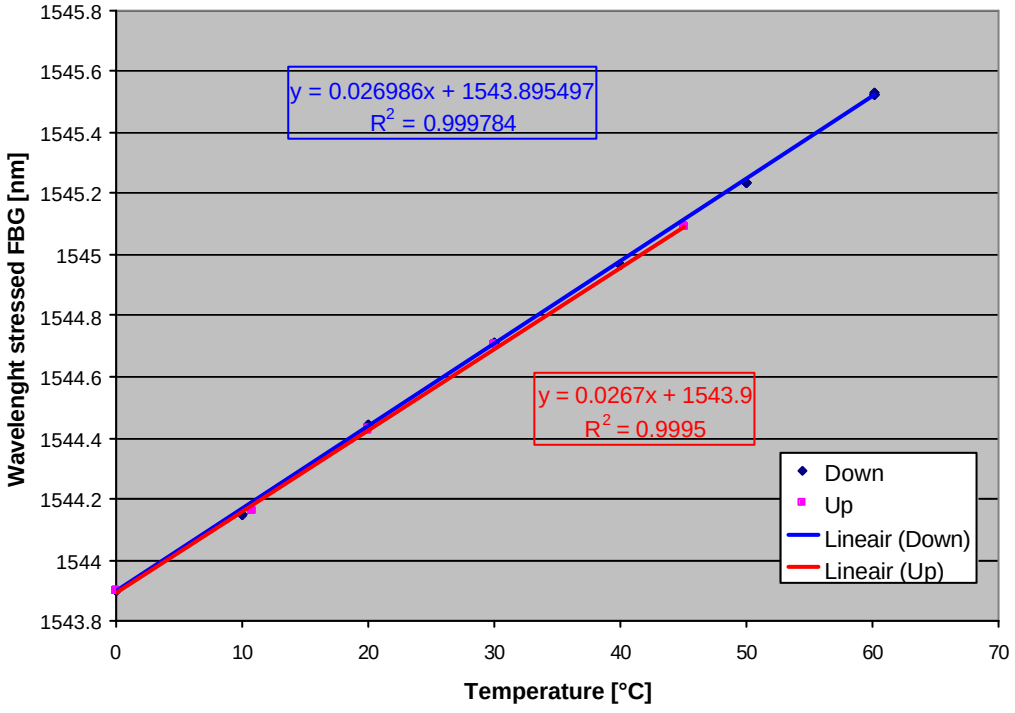

Fig. 1.55: Temperature calibration of the stressed FBG of hydrogen sensor I.

The design of sensor II is based on the concept of the temperature sensor. Fig. 1.56 shows the design of the sensor. As can be seen, the sensor exists of 3 capillaries. The small capillaries are made of stainless steel and are used to fix the fibre (gluing). These capillaries have an outward diameter of 2 mm at one end and an outward diameter of 1.5 mm at the other end. This allows to put these capillaries into the larger Pd capillary which has a purity of 99.95%, an outward diameter of 2 mm and an inner diameter of 1.6 mm. Fig. 1.57 shows a photo of the sensor. When now the Pd capillary absorbs hydrogen, the capillary will expand what results in a strain on the fibre.

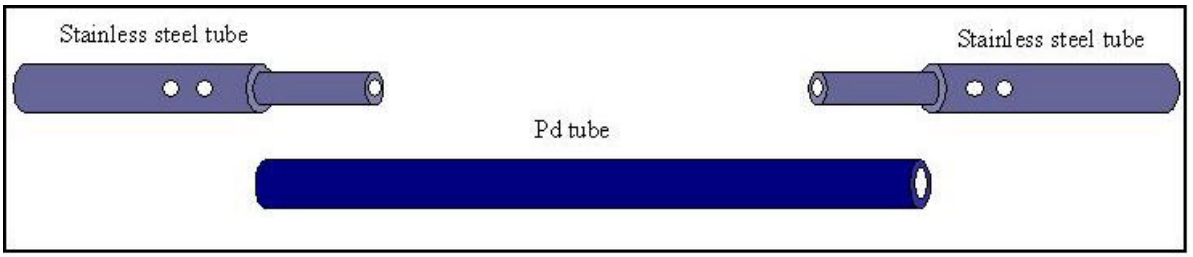

Fig. 1.56: Design of hydrogen sensor II

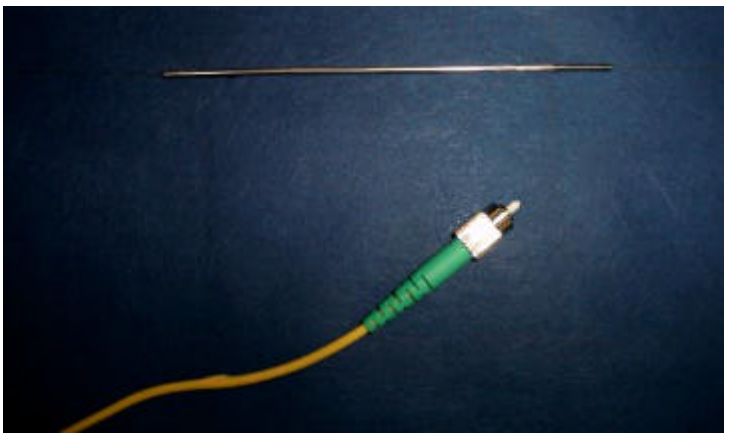

Fig. 1.57: Photo of the hydrogen sensor II.

The wavelength shift on the grating due to the presence of hydrogen is given by:

$$\Delta\lambda = 1.2 \bullet 10^6 \,.\, \varepsilon_P(P_{H2})\, L_{Palladium} / L_{FBG} \qquad (1.19)$$

With $\Delta\lambda$ the wavelength shift in [pm]; $\varepsilon_P(P_{H2})$, the strain on the Palladium material caused by the hydrogen pressure P_{H2}; $L_{Palladium}$, the length of the Palladium tube; L_{FBG} , the length of the fibre hosting the stretched FBG. This length is equal to the distance between the fixation points on the two stainless steel capillaries. As a consequence, by changing the position of these fixation points, the sensitivity can be changed. For the prototype, we did chose $L_{palladium}$ equal to L_{FBG}. As a consequence, the wavelength shift is given by:

$$\Delta\lambda = 1.2 \bullet 10^6 \,.\, \varepsilon_P(P_{H2}) \qquad (1.20)$$

If we compare this with the prototype of sensor I, we expect that sensor II will be 90 times more sensitive.

Furthermore, a separate FBG has been used during the experiments. For the final design this should also be included in order to take into account the temperature dependence of the FBG wavelength. Also the influence of the thermal expansion of the sensor should be investigated and be taken into account.

However, for the experiments discussed in this report, the temperature compensation is not that important to interpret the behaviour of the sensor since the temperature is kept more or less stable during the experiments.

1.9.3. Calibration set-up

Fig. 1.58 shows the experimental set-up used for the first experiments. The system consists of a vacuum chamber, which is equipped with a rotary pump (Trivac, type D4A) and a Turbo pump (Balzers, type TPH 170). The base pressure of the vacuum system is equal to 10^{-6} mbar. In order to bring hydrogen into the vacuum chamber, forming gas with a composition of 10% H_2 and 90% N_2 is used. The calibration was performed by measuring the wavelength change in function of the partial hydrogen pressure. The temperature was kept stable at 23°C during the experiments. Finally, in order to measure the hydrogen sensors, a special flange with a fibre throughput was built.

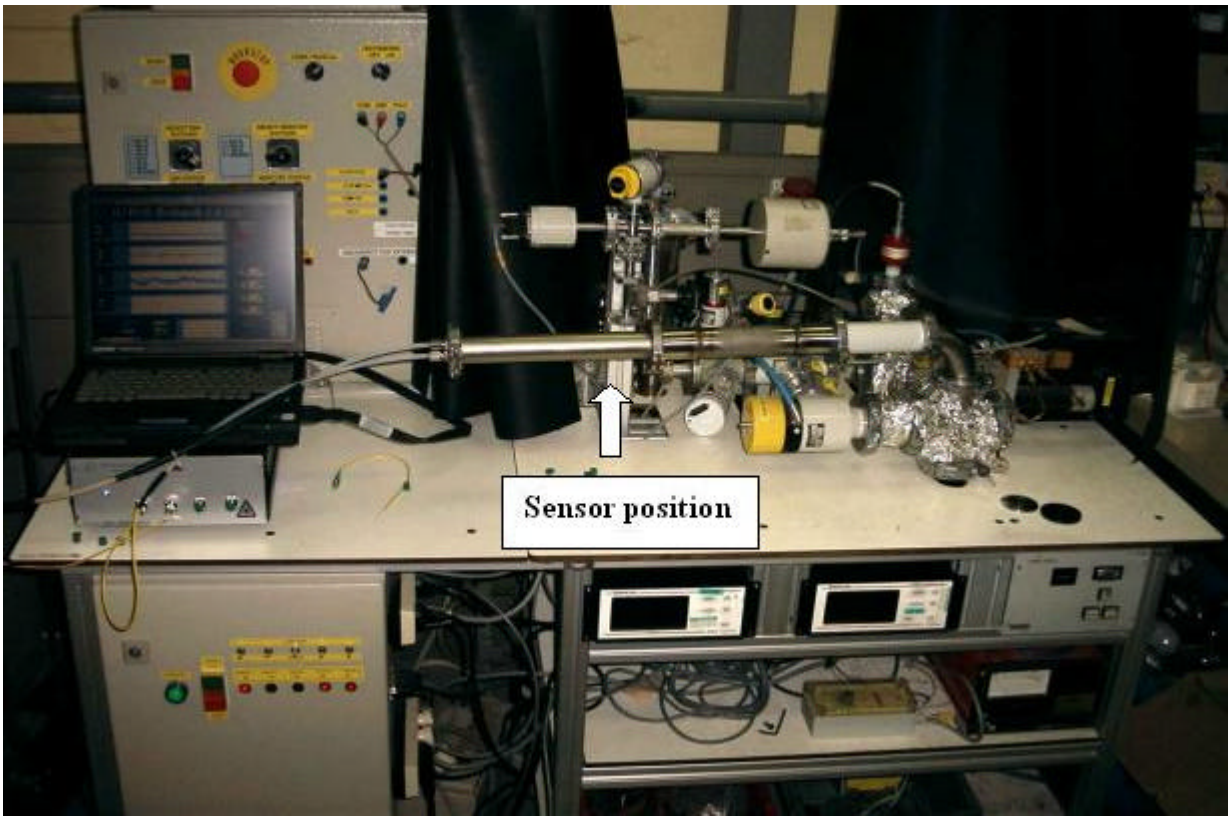

Fig. 1.58: Calibration set-up for hydrogen sensors

In a later phase of the project an own calibration system has been built at the I.D. FOS Research lab, see Fig. 1.59. The system consists of a chamber that can be filled with forming gas. This is a mixture of H_2 in N_2. A calibration can be performed by using different mixtures of forming gas or by changing the pressure in the chamber. The pressure can be changed between 1 and 8 bar. This allows to change the partial pressure of the hydrogen concentration using 1 mixture. In order for safety reasons, the hydrogen concentration will not be higher than 4.2% H2.

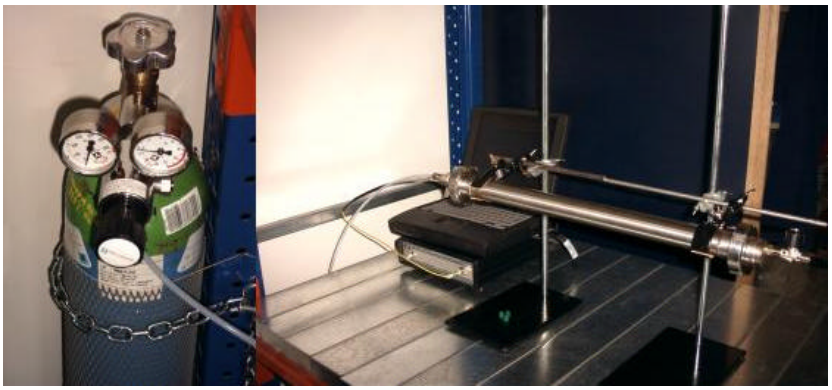

Fig. 1.59: Calibration system at I.D. FOS Research lab.

1.9.4. Experimental results

Test sensor I: The wavelength of sensor I was measured for partial hydrogen pressures ranging between 0 and 100 mbar. Unfortunately, this sensor was not able to detect a response under the given experimental conditions. A possible explanation for this might be that the contact surface of the Pd-disc with the hydrogen molecules is much to small. The design of sensor I needs therefore to be modified in order to increase this contact surface.

Test sensor II: The wavelength of sensor II was measured for partial hydrogen pressures ranging between 0 and 50 mbar. In Fig. 1.60 the wavelength response is shown in function of the partial pressure. The vertical lines in the plot are caused by a slow absorption process of the hydrogen by the Pd (When the hydrogen pressure is increased, the wavelength increases very slowly). It can be observed that a strong response is becoming visible starting from hydrogen pressures around 18 mbar. This strong response can be explained by the formation of the β-phase at this pressure. Notice that this is also in good agreement with the results of Bévenot et al. [2] who observed that the β-phase is formed between the 15 and 20 mbar. By further increasing the hydrogen pressure up to 50 mbar, a wavelength shift of 180 pm could be observed.

The time response during the hydrogen uptake is shown for three pressures: 18 mbar, 25 mbar and 50 mbar (see Fig. 1.61, Fig. 1.62 and Fig. 1.63). These measurement points are also marked with A, B and C in Fig. 1.60. As can be observed, the sensor reacts very slowly. No saturation level could be observed within 1 hour. Fig. 1.64 shows the response time of the dehydrogenation of the Pd surface when taking the sensor out the 50 mbar environment into air. Again a slow response time is observed. It did take more or less 10 hours in order to fall back to 50% of the maximum response. The low response times can possibly be explained by the presence of contaminants on the Pd-surface. This can be solved by using a pre-heat treatment in air of the Pd surface.

Finally, some remarks about the sensitivity. According to the results of Mueller et al., a hydrogen concentration of 10^{-5} bar (1 Pa) should already result in a strain in the Pd-material of 8.5 με. This should correspond to a wavelength shift of 10.2 pm. Unfortunately, this is not observed. A possible reason is again the low response time of the sensor.

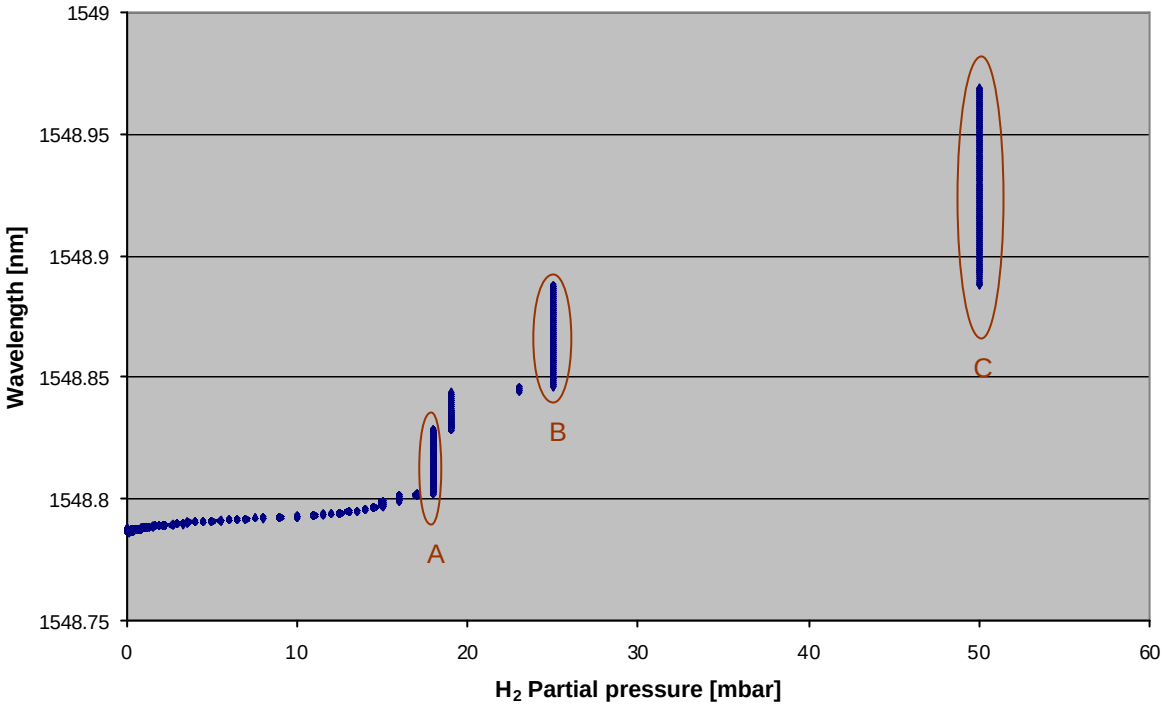

Fig. 1.60: Response of sensor II

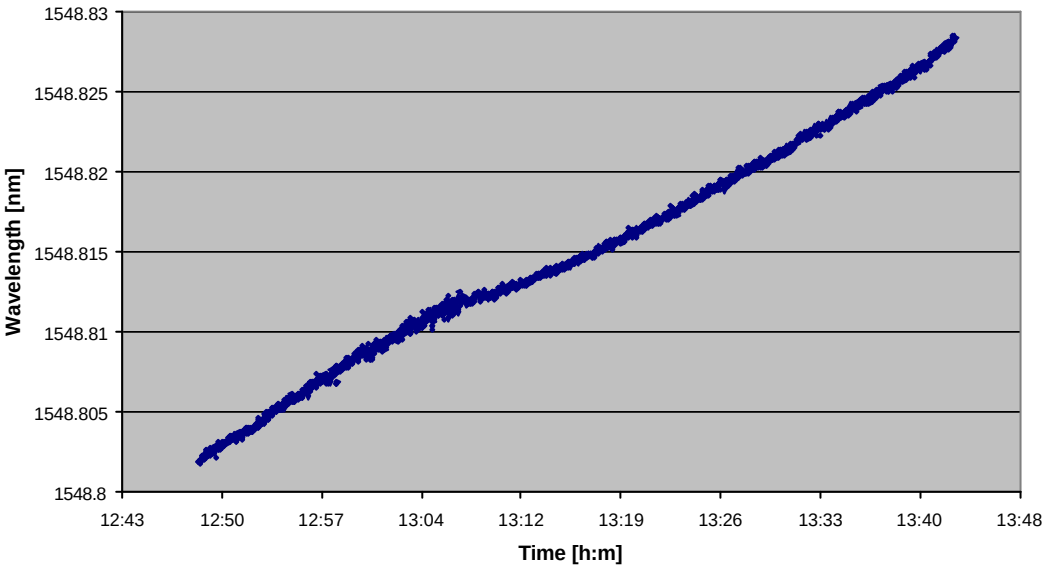

Fig. 1.61: Time response of sensor II at a hydrogen concentration of 18 mbar (Plot A)

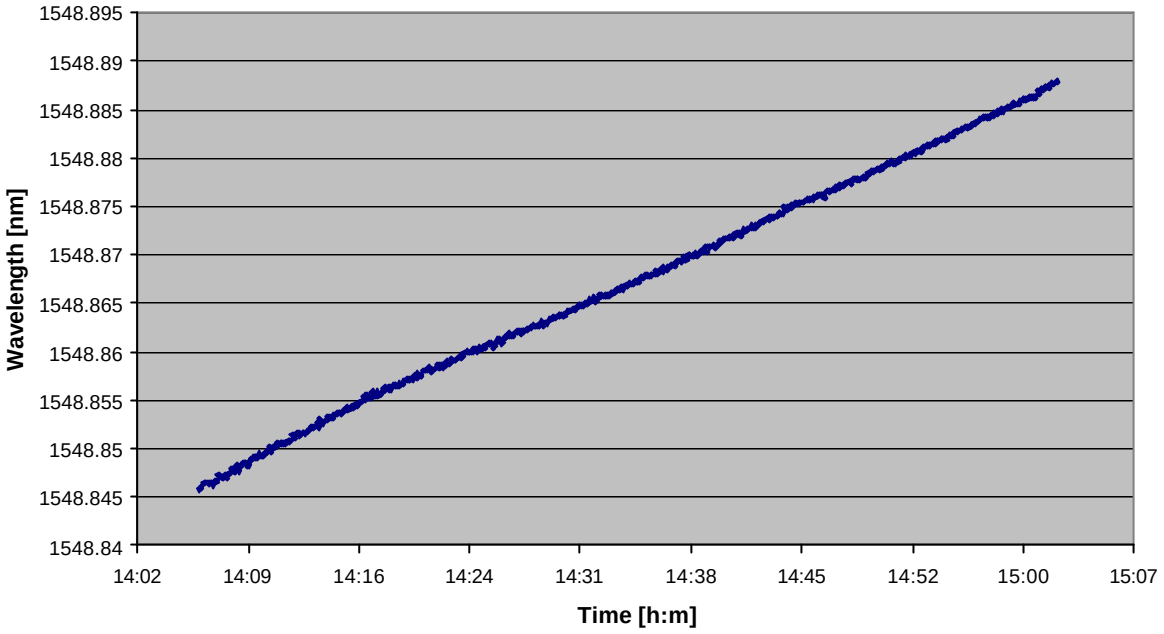

Fig. 1.62: Time response of sensor II at a hydrogen concentration of 25 mbar (Plot B)

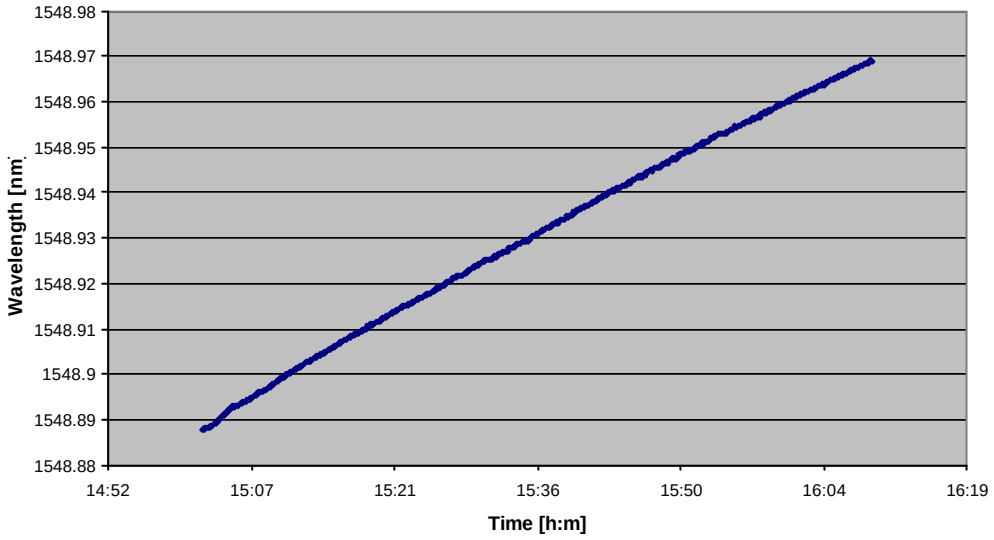

Fig. 1.63: Time response of sensor II at a hydrogen concentration of 50 mbar (Plot C)

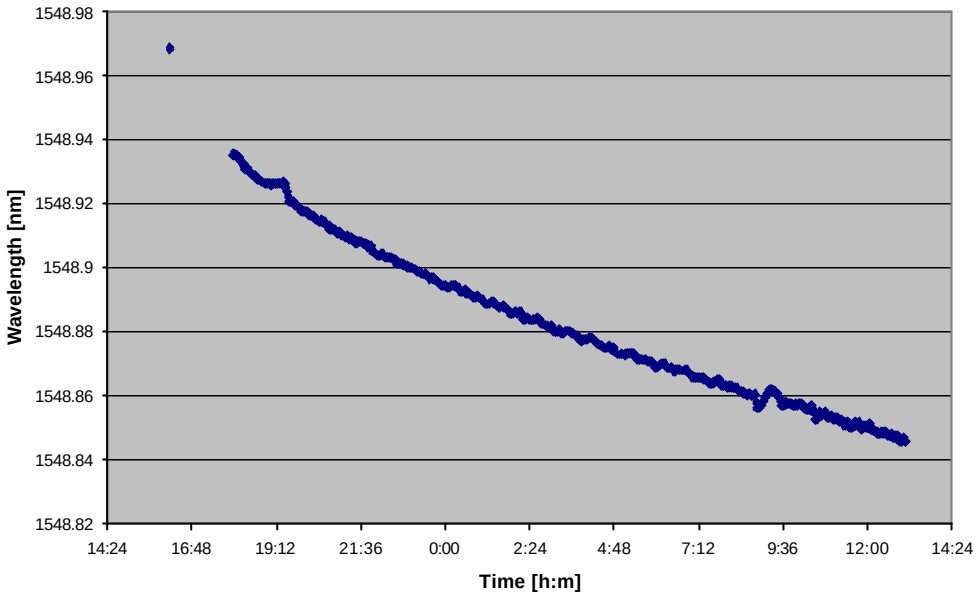

Fig. 1.64: Sensor response after taking the sensor out the 50 mbar hydrogen environment into the atmosphere.

In a second series of experiments the response of the hydrogen sensor II was recorder for a longer time period. This was done using the calibration set-up developed at I.D. FOS Research.

Fig. 1.65 shows the response of sensor II in a hydrogen atmosphere of 5 mbar during 11 days. As can be observed, a wavelength increase of 493 pm has been recorded over 11 days. In the first 3 days, there's already an increase of 203 pm. It can be seen that the Pd is even not completely saturated after 11 days. Fig. 1.66 shows the sensor response at a partial pressure of 20 mbar. First of all it can be observed that the absorption happens much faster at this pressure. After the 3$_{rd}$ day there's already a wavelength difference of 540 pm. The response seems to saturate faster compared to the 5 mbar experiment. The total response is around 952 pm. However, this saturation level seems to be an intermediate saturation level. This can be seen in Fig. 1.67 where the measurement is redone but now over a period of 1225 hours. As can be observed, the response seems to saturate again after 60 hours giving an offset level around 1 nm. However, the signal starts increasing again at 120 hours. After 1040 hours, the partial hydrogen pressure was put at zero. A steep decay can from then on be observed. 170 hours later, the sensor is back at it's initial value. As a consequence, it can be concluded that the depletion process is going much faster as the absorption process. Finally, it needs to be noticed that the small bumps in the plot are caused by temperature changes (day/night).

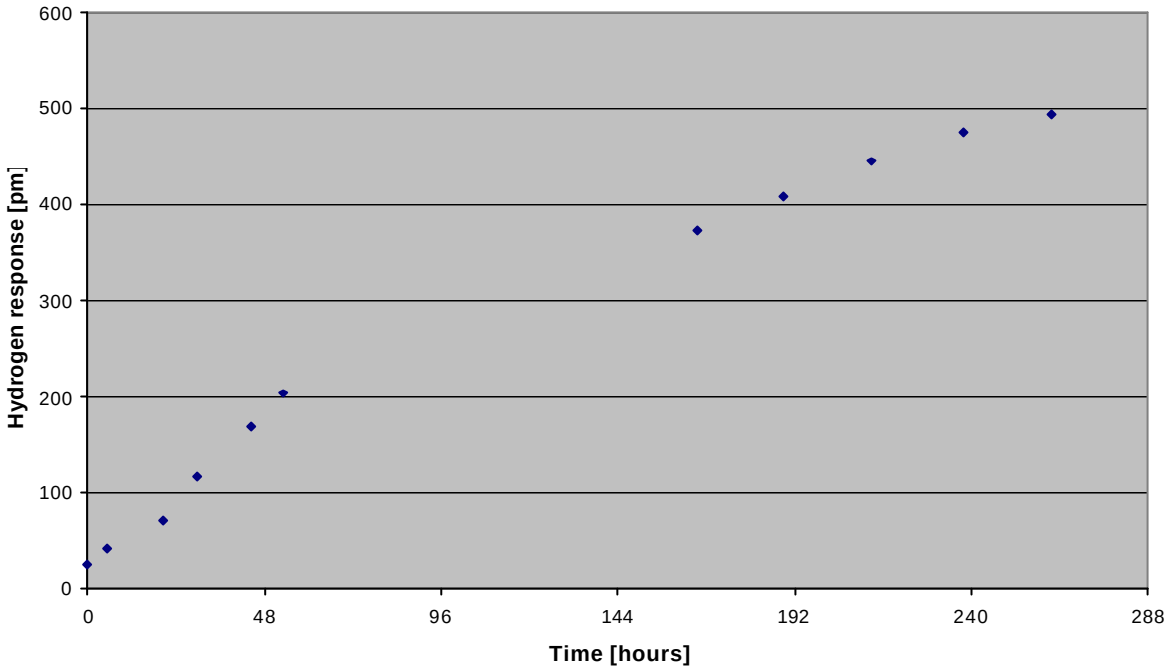

Fig. 1.65: Measured hydrogen response at a partial pressure of 5 mbar.

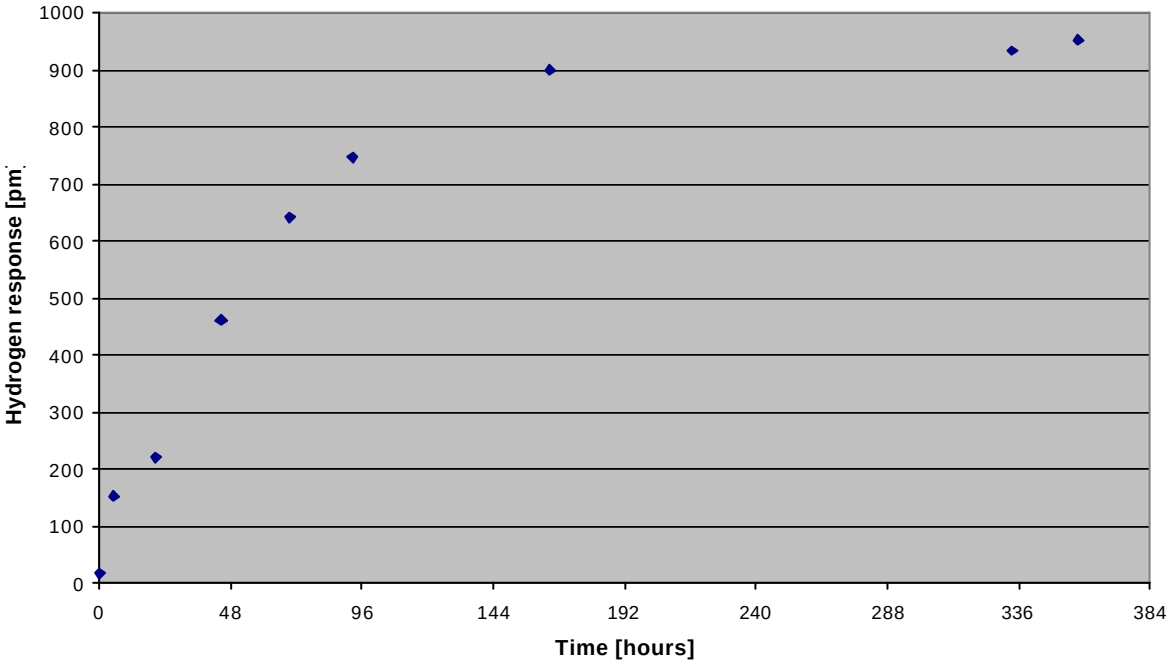

Fig. 1.66: Measured hydrogen response at a partial pressure of 20 mbar.

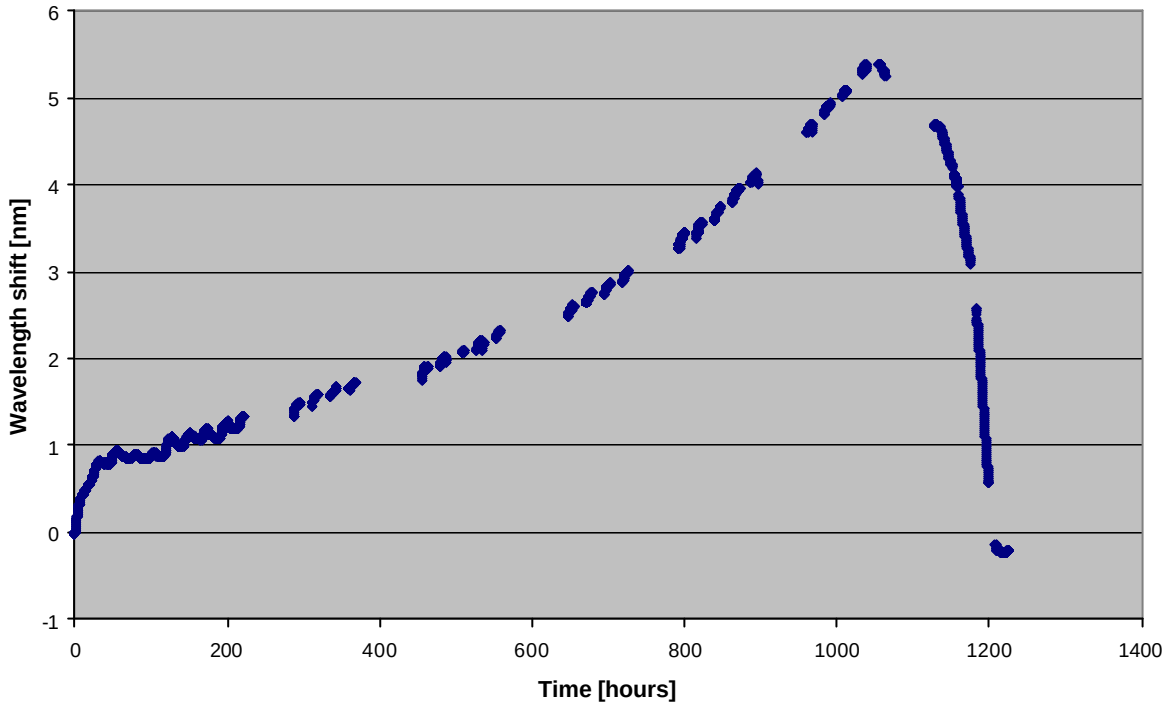

Fig. 1.67: Measured hydrogen response at a partial pressure of 20 mbar over a period of 50 days.

1.9.5. New design

The major problem with the previous hydrogen sensor is the very slow response time. This is due to the small surface/volume ratio of the Pd material. In order to enhance the response time a new design of the sensor lay-out has been tested with a small surface volume ratio. The sensor consists of a naked FBG that directly has been coated using Pd. Due to the presence of hydrogen, the Pd will swell and induce a strain on the FBG, resulting into a wavelength shift.

So far, a lot of effort has been put into the production method of this type of sensor. The Pd is deposited using a plating technology. Unfortunately, some problems still remain. The problem is that the stress becomes too high in the Pd deposit which then curls the fibre. The deposit finally cracks and relieves the stress on the fibre.

In order to solve these problems, more testing should be performed using an intermediate layer between the glass fibre and the Pd coating that acts as a buffer between the glass and the Pd. It is for example known that when a thin Ti layer as intermediate layer is used, a good adhesion can be achieved [9].

1.10. pH sensor

1.10.1. Working principle

The pH system consists of a probe containing methyl red. Methyl red has the properties that the reflection of light is dependent on wavelength but also on the pH level witch which the probe is into contact. As a consequence, by measuring the reflection characteristics of the methyl red as function of the wavelength, the pH value can be determined.

1.10.2. Measurement principle of the opto-electronic unit (hardware).

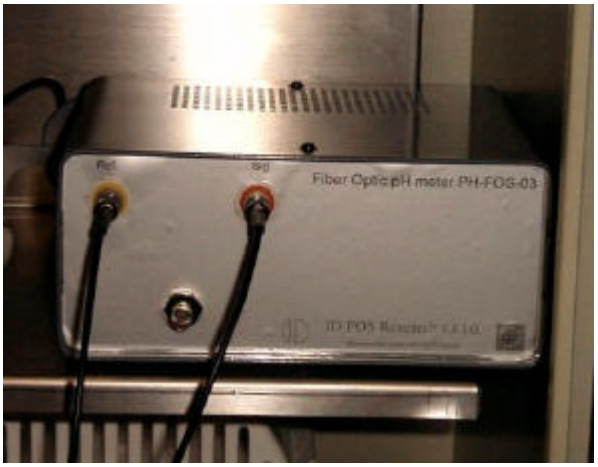

Fig. 1.68: Opto-electronic unit

Fig. 1.68 shows the opto-electronic unit that has been developed. The system is based on the utilisation of only one LED, which is modulated in order to allow a referenced measurement.

The modulation is carried out by driving the LED in two different states with two different currents. By changing the driving current the emission of the LED changes: the change is roughly 10 nm. The difference between the detected signals in correspondence of the emission at these two different wavelengths gives the possibility of measuring the slope of the absorption spectrum which is dependent on the pH level. The method is more sensitive at the wavelength at which the absorption curve has a higher slope. In the case of methyl red the wavelength is around 505 nm.

Therefore, with this method the slope of the absorption curve is measured: clearly there is a different slope for each pH value. The important aspect is that any interferences and fluctuations, which do not modify the slope of the absorption spectrum, do not give rise to changes in the detected signal. Hence, bending of the fibre, fluctuations of the source, turbidity (if it introduces a constant contribution at the wavelengths of interests) do not interfere with the measurement. This can be understood as follows:

The unit measures the reflected signals at two different wavelengths which are 10nm separated. These reflected signals are called R_1 and R_2. The difference between both signals is used to calculate the slope. Actually, a normalized slope is measured according to:

$$\text{slope} = \frac{R_2 - R_1}{R_1} \tag{1.21}$$

When now for instance an external loss occurs of x% due to a strong fibre bending, then the slope can be given by::

$$\text{slope} = \frac{R_2.(1-x) - R_1.(1-x)}{R_1.(1-x)} = \frac{R_2 - R_1}{R_1} \tag{1.22}$$

what is exactly the same as the first slope. Notice that each signal is affected by the same loss factor due to the fact that both signals are generated by the same LED and make use of the same fibre, fibre connections, etc. As a consequence, changes in losses will not affect the slope. This is true also for coloured solutions which have flat absorption spectra at around 505 nm.

The first test has been carried out in order to see if the measured caused a drift due to the photo decomposition of the immobilised dye. Test has been carried out for ten days and the result is shown in Fig. 1.69. Notice that the ambient temperature has also been measured.

During the whole experiment, the sampling time has been set to one hour. In the first 72 hours the LED is turned on for 100 seconds, whereas after the 72nd hour the LED is turned on only for 20 seconds (which means that the optical power which goes on the reflector, is decreased by a factor 5).

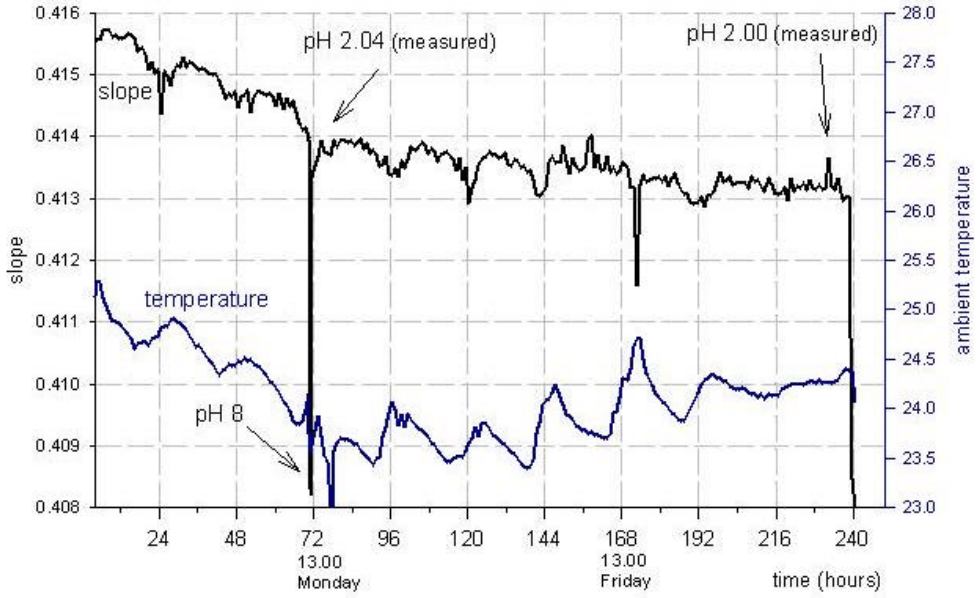

Fig. 1.69: Drift of the probe characterised with the new opto-electronic unit

We should consider that methyl red, the dye immobilised on the CPGs, is characterised by a negative coefficient $\Delta(\text{slope})/\Delta T$ where T is the temperature: the detected slope at a definite pH value increases if the temperature decreases. In the first 72 hours, the drift is apparent: the temperature decreases and also the detected slope decreases, although the probe is always dipped at pH 2.04. After the hour 72, the optical power is decreased of a factor 5 and the decrease in the slope is considerably smaller; moreover, in this period the temperature increases and the decrease of the detected values of the slope is perfectly in agreement with the increase of temperature; this means that from hour 72 to hour 240 (six days) the drift due to the photo decomposition of the immobilised dye is absent or negligible.

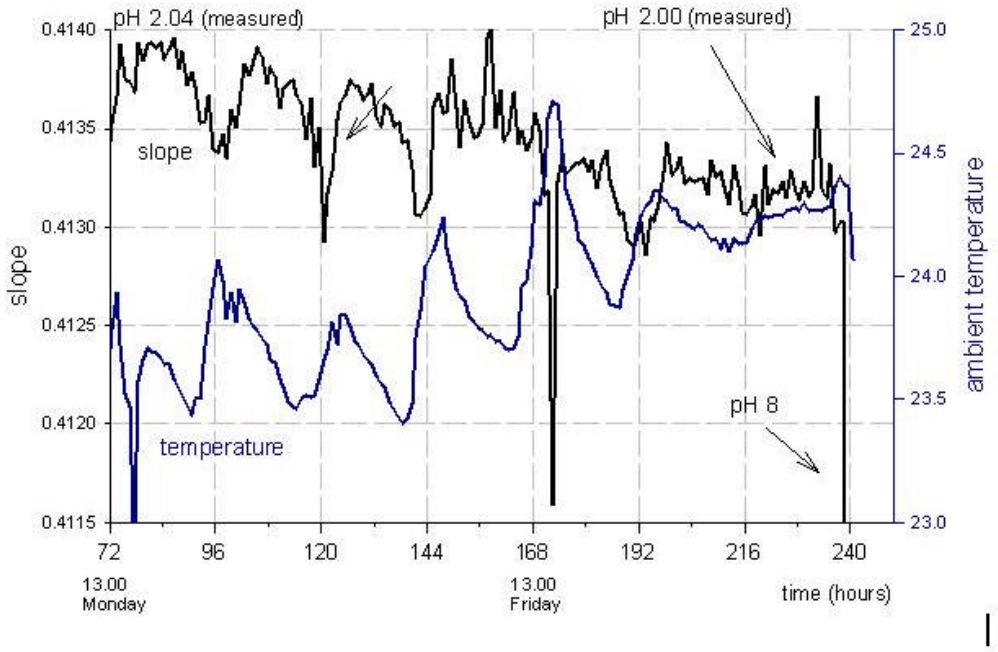

Fig. 1.70: Detail of the drift of the probe characterised with the new opto-electronic unit: sampling time 1 hour, LED turned on for 20 seconds.

This measurement also shows a not negligible dependence of the probe response to temperature. Every increase of the ambient temperature (in correspondence of the warmer hours of the day) corresponds to a decrease in the detected signal.

An accurate temperature characterisation has been carried out, by dipping the probe in buffer solutions kept at constant temperature by means of a thermocryostat. Calibration curves have been obtained for three different temperatures: 10°C, 20°C and 30°C.

Fig. 1.71 shows the details measured at a temperature of 20°C. Measurement has been carried out with a sampling time of one minute and with the LED turned on for 30 seconds: the recorded value is the average on the last 10 seconds.

In Table 1.6, the detected values for each pH step are given. It is noteworthy to observe that the hysteresis is negligible. The error on the detected slope has been evaluated considering the standard deviation on the last five detected values. It is $\leq 10^{-4}$.

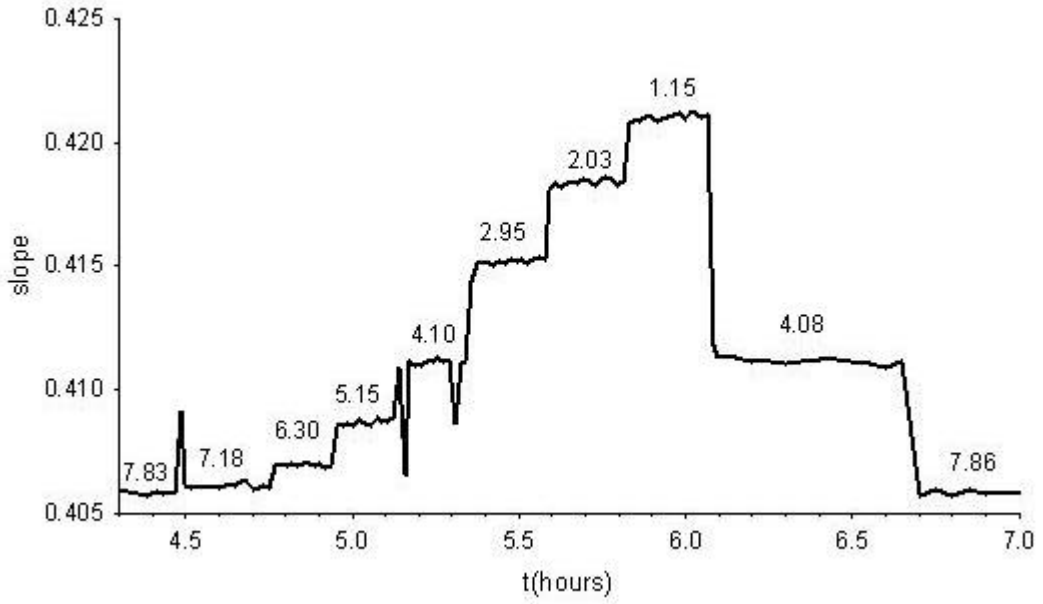

Fig. 1.71: Detail of the temperature characterisation for the 2nd cycle at T= 20°C.

T=10°C				T=20°C				T=30°C			
7.75	0.4056	7.83	0.4055	7.83	0.4058	7.86	0.4058	7.90	0.4059	7.94	0.4058
7.16	0.4059			7.18	0.4061			7.27	0.4062		
6.28	0.4070			6.30	0.4069			6.28	0.4070		
5.26	0.4085			5.15	0.4087			5.06	0.4086		
4.20	0.4112	4.22	0.4114	4.10	0.4111	4.08	0.4111	3.95	0.4108	3.95	0.4108
3.09	0.4158			2.95	0.4152			2.82	0.4143		
2.20	0.4189			2.03	0.4185	2.06*	0.4182	1.88	0.4177		
1.19	0.4212			1.15	0.4211			0.95	0.4206		

Table 1.6: pH values and related detected values of the slope for the three different cycles.

The resolution in terms of pH can be evaluated around 0.03 pH units for pH below 5. The accuracy becomes worse and worse with the increase of pH; it can be considered roughly 0.08 pH units between 5 and 7. Fig. 1.72 shows the three calibration curves at 10°C, 20°C and 30°C.

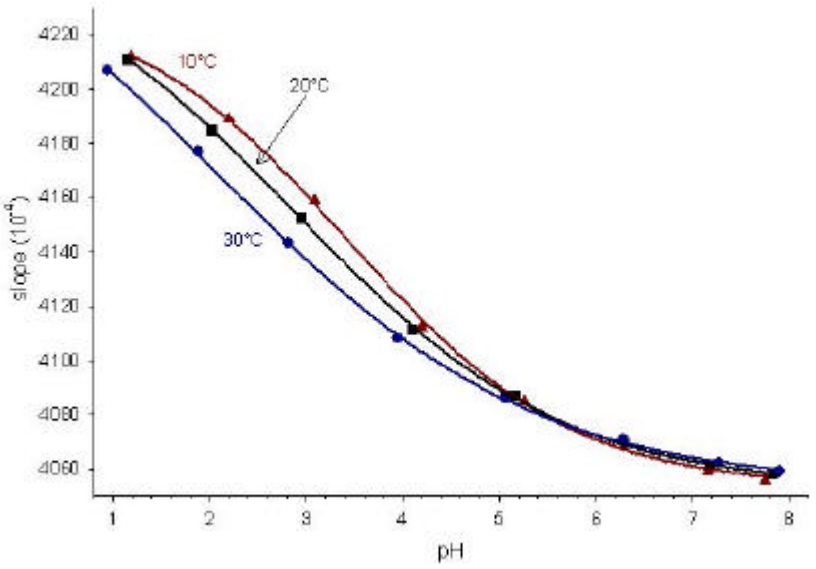

Fig. 1.72: Calibration curves for the three different temperatures.

The curves that are drawn in Figure 1.72 are exponential functions of the type:

$$f = y_0 + a/(1 + \exp(-(x - x_0)/b)) \qquad (1.23)$$

With this function, the best with the recorded data is obtained, but this implies a calibration with four pH values.

These curves pointed out that it is necessary to know exactly the temperature of the probe. With this knowledge in principle it could be possible to perform an automatic correction of the pH value.

In order to test the calibration equations, the probe has been dipped in a buffer solution at pH=2.06, kept at the temperature constant of 20°C. The sampling time has been equal to 90 minutes with the LED turned on for 30 seconds and the average time equal to 10 seconds. It is noteworthy to consider that the measured value of the slope has been 0.4182 that was very close to the measured value during the second cycle. The stability has been checked for 24 hours and no drift has been observed (Fig. 1.73). A noticeable improvement of the measurement has been carried out by using the same LED for the signal probe and for the reference probe. This improvement has been possible thanks to the use of a suitable optical fibre connection inside the instrument. This improvement was necessary since the use of two different sources could cause an intrinsic error due to the fact that two sources are characterised by different drifts and fluctuations.

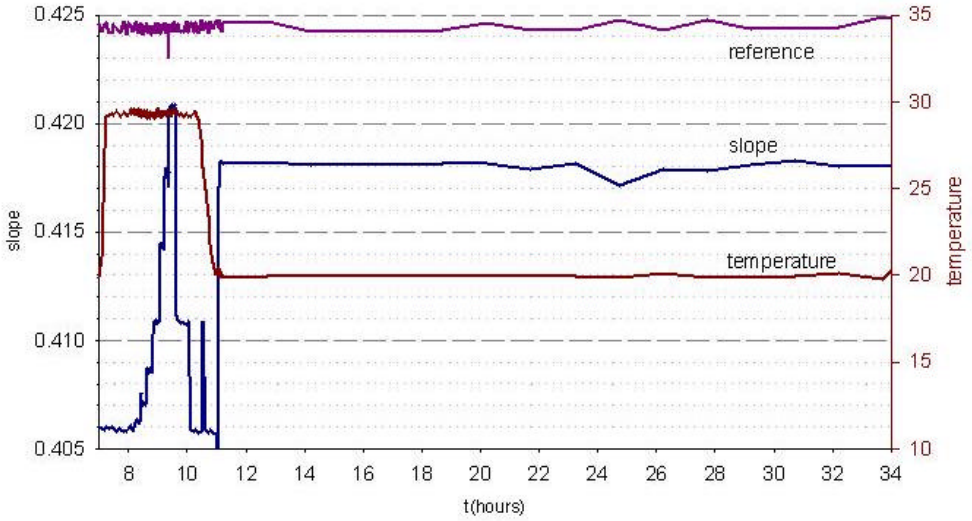

Fig. 1.73: Stability test of 24 hours.

1.10.3. Software

The interrogation software is written in Labview and can be controlled using a front panel (Fig. 1.74). The front panel is also used to calibrate the unit.

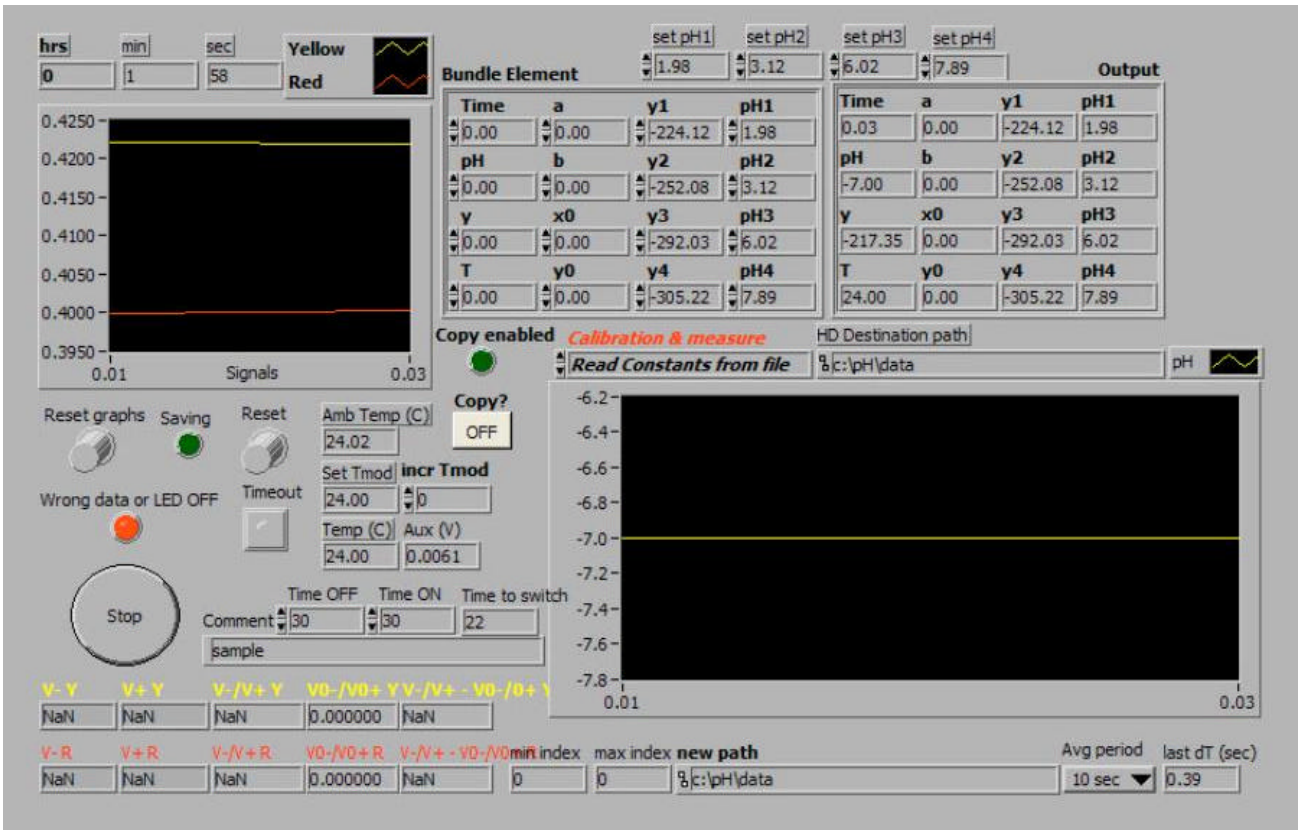

Fig. 1.74: Front panel optical pH-meter.

To calibrate the pH meter you need a conventional pH meter and pH buffers (2, 3, 4, 6, 7 and 8). To calibrate the unit:

1. start the new prototype_pH1LED_1.vi' vi its located on c:\pH\vi\vi_1
2. Fill in 30 for TimeON. (This is the time the unit is measuring)
3. Avg. Period = 10
4. Measure the pH value of the buffer with the conventional pH-meter and fill in at setpH1
5. Now put the pH probe in the pH=2 buffer
6. Choose in the menu pH1
7. Start the vi
8. Repeat steps 4 to 7 for all the different pH buffers
9. At this point the software has all data to calculate the calibration constants. Choose calculate constants to calculate them.

Once the calibration has been done, the constants are automatically filled in the Bundle Element field. Before starting measuring some parameters need to be defined:

1. For TimeOFF choose the time between two measure points.
2. Put timeOn on 30
3. Set Tmod on 25°C
4. Choose in the HD destination path field the path and filename to save the measurement.
5. Start the vi

1.10.4. Chemical details

The methyl red (MR) has been immobilised on controlled pore glass (CPG): the surface of the controlled pore glass (CPG) has been silylated by means of γ-aminopropyltriethoxysilane (γ-APTS) and, after proper chemical reactions, MR has been bound in a covalent way to the glass support, see Fig. 1.75.

Fig. 1.75: Reflector detail

Fig. 1.76 shows the sequence of the chemical reactions. The glass support has been oven-dried at 120°C for 1 h and added to a 10% γ-APTS solution in toluene; after refluxing for 22 h, it has been washed with toluene, methanol, acetone and then oven-dried at 80°C for 1 h.

The amidisation procedure was the following: the dried carrier has been soaked in a solution of p-nitrobenzoyl chloride in chloroform containing triethylamine. Initial amine, acid chloride and triethylamine were present in an approximately 1:3:4 mole ratio. This mixture has been refluxed for 24 hours and, after cooling, the carrier has been washed with chloroform.

Reduction of the nitro group has been carried out in a boiling dithionite for 1h: an approximately 3-fold molar excess of dithionite (as compared to the original amine) has been used, resulting in 3-5% dithionite solution. After the reaction, the product has been washed with water.

The carrier has been placed in a 2% sodium nitrite solution in 2 M HCl in a ice bath (0-3°C), stirred for 30 minutes, washed with water and immediately added to 50 ml of water containing 0.05 g of the indicator. The pH of the solution has been basic in order to maximise dye solubility and to have the dye in anionic form. The reaction has been carried out at 4°C for 24h.

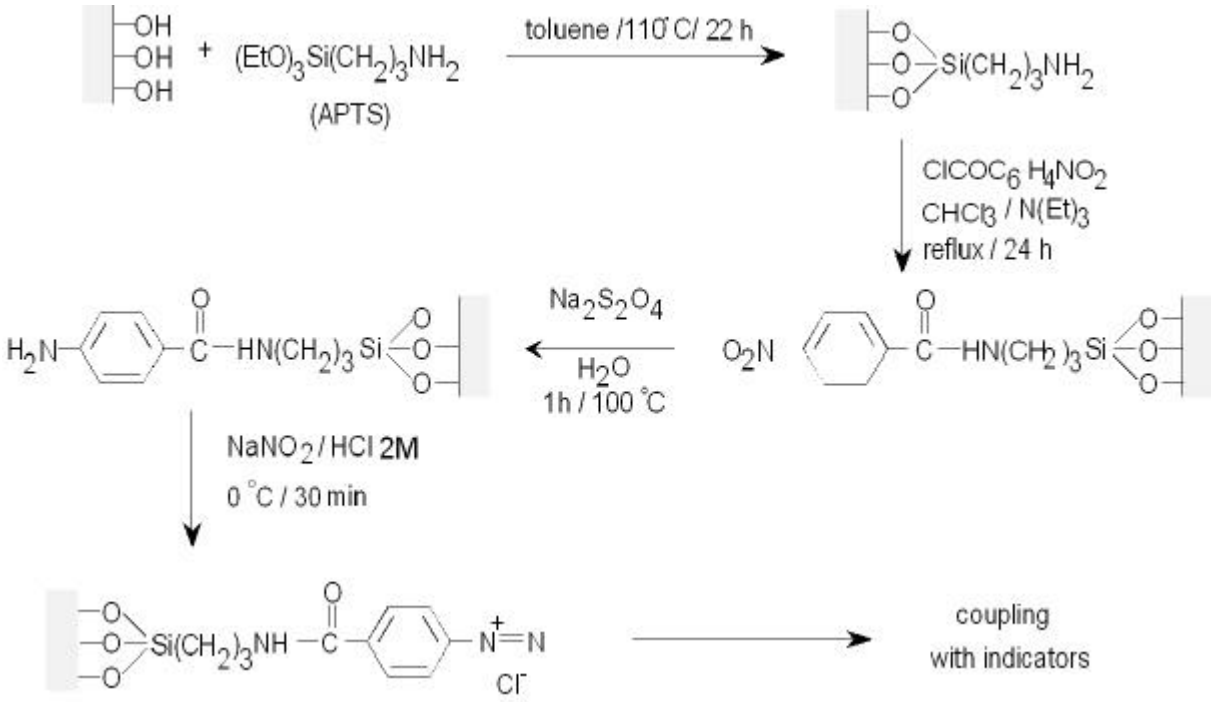

Fig. 1.76: Sequence of the chemical reaction used to immobilise methyl red on CPG.

The treated CPG has been immobilised by means of a melting process that made it possible to embed the glass support in a plastic reflector. This reflector has been brought in contact with a heated surface on which a uniform layer of CPG has been placed. Near the melting point, the plastic material softened, and by exertion of a light pressure, CPG penetrated inside the reflector. When the reflector became cold, the granules of CPG remained entrapped on the plastic reflector.

The plastic support has been characterised with a spectrophotometer, fixing the reflector in front of plastic fibres connected to a spectrophotometer, Fig. 1.77.

The absorption spectra for different pH values are shown in Fig. 1.78, which also shows the relationship between absorbency A (evaluated at the absorption peak at 556 nm) and pH. The connection with the fibres between the opto-electronic unit and the reflectors is shown in Fig. 1.79.

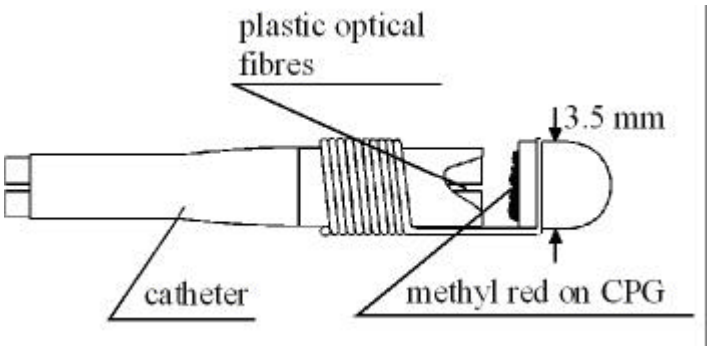

Fig. 1.77: Sketch of the optical fibre pH probe used for the spectrophotometry characterisation.

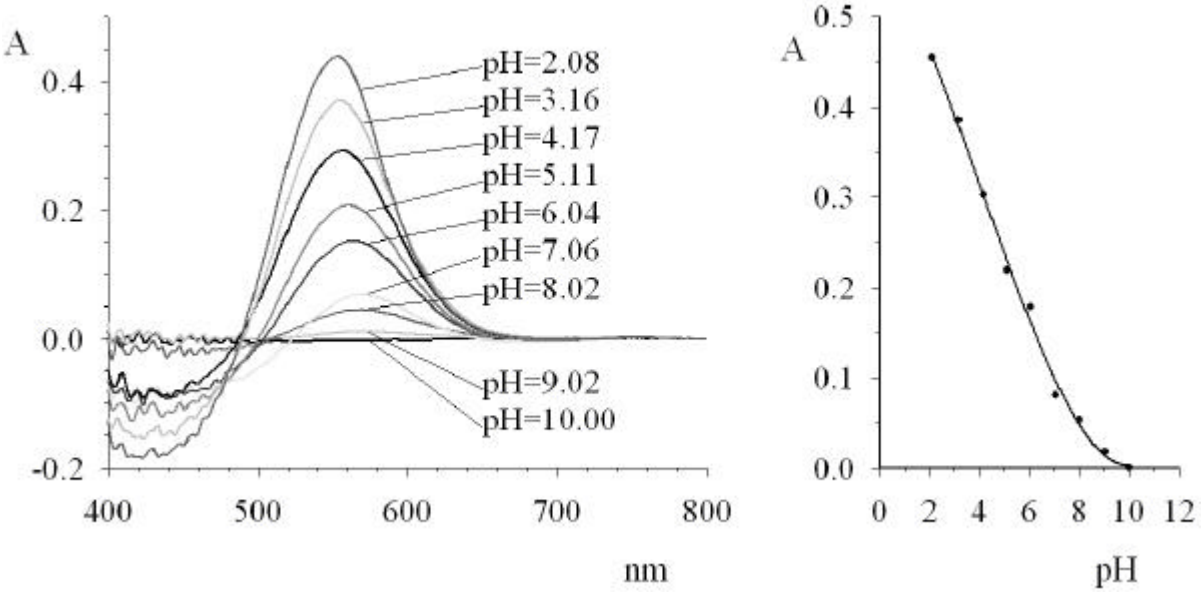

Fig. 1.78: Absorption spectra of methyl red on CPG for different pH values (on the left) and absorbency at 665 nm vs pH (on the right).

Fig. 1.79: Picture of the optical fibre pH probe.

2. Multiplexing techniques and interrogation units

2.1. Interrogation system

Within an former project, the FBG-based sensors have been interrogated with a broadband optical source (40 nm wide) and the spectral responses of the different sensors in the network are demodulated (sensor wavelength measured) with a standard Fabry Pérot (SFP) filter from Newport. The instrument has been named as FMUB-SFP The SFP demodulator has been delivered on a board together with the driving /interface electronics, linearisation/temperature stabilisation, opto-electronics and driving /interface software modules. The calibration has been applied every scan using two reference gratings at the beginning and the end of the spectrum.

This system shows however some shortcomings:

1. The reference gratings are temperature sensitive. A drift of the environmental temperature of the measurement unit will as a consequence also influence the calibration process.
2. Deviations from the linear behaviour of the SFP can not be corrected using only the 2 reference FBGs.
3. The SFP is rather large and composed using different mechanical components that require from time to time a realignment. These misalignment problems are very time consuming and reduce the reliability of the system.

In order to improve the system, the integration of a new system has been performed. The new system is based on the FBG-IS from Micron Optics. The schematic diagram of the system is shown in Fig. 2.1. As can be observed, the system is similar as the FMU-B-SFP lay-out. The major difference is the type of filter device and type of reference device.

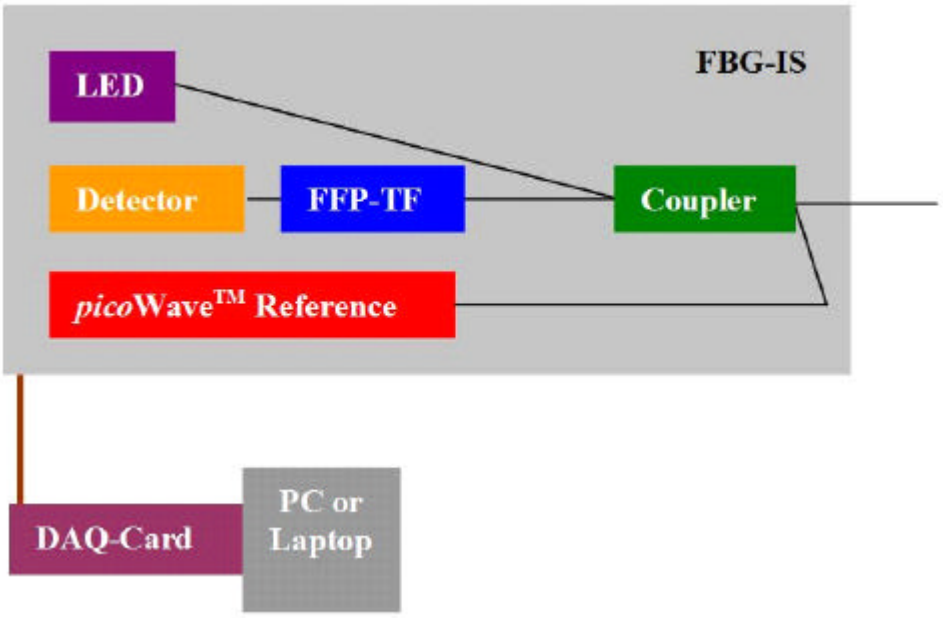

Fig. 2.1: Schematic lay-out of the FBG-IS

The filter device is a Fibre Fabry Perot Tunable filter (FFP-TF) which is shown in Fig. 2.2. The FFP-TF is an optical cavity composed within an optical fibre which is used to scan the wavelength range. No lenses, no collimating optics, just simply fibre and mirrors.

This true fiber cavity constitutes Micron Optics FFP Technology. All the high optical resolution advantage of the "old", bulk optic device is preserved, but with three critical distinctions:

• Micron Optics FFP Technology has optical fiber inside the etalon which guides the light with each bounce between the mirrors. The extreme alignment, temperature, and vibration sensitivities of the "old", bulk-optic Fabry-Perot interferometers are gone. In fact, the alignment sensitivity of FFP technology is no more than that of an individual single-mode optical fiber splice or connector.

• Micron Optics FFP Technology has natural fiber connection compatibility unlike lenses or integrated waveguides, which encounter fundamental connection difficulties.

• Micron Optics FFP Technology is combined with the highest resolution mechanical positioning devices, Piezoelectric Transducers (PZTs), to position the mirrors in Micron Optics' FFPs. PZTs are used in atomic force microscopes to position elements to sub-atomic dimensions. This level of mechanical resolution ensures stable, smooth, repeatable tuning of any FFP filter.

These three critical innovations allow the FFPs optical response to truly follow the Airy function from the top of its low-loss peak down to the very bottom of its stop band, and to be smoothly and precisely controlled over all points in between.

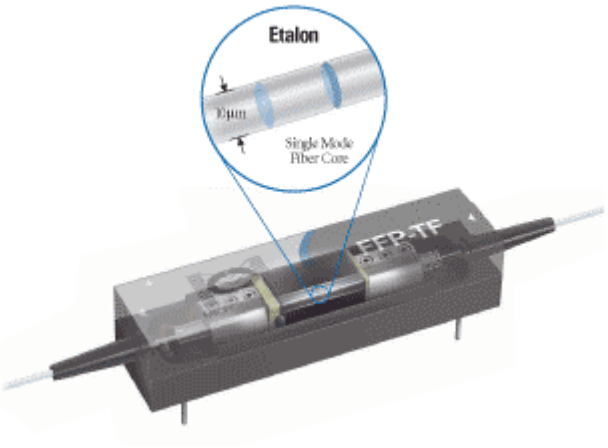

Fig. 1.2: Schematic design FFP-TF

Furthermore, the FBG-IS makes use of the picoWave reference module. This is a Fiber Fabry-Perot Interferometer (FFP-I), based on a fixed interferometer design with smooth, uniformly spaced transmission peaks. The FFP-I consists of a lensless plane Fabry-Perot interferometer with a single-mode optical fiber waveguide between two highly reflective multilayer mirrors. The FFP-I is manufactured with fiber pigtails so no alignment or mode-matching is required. The distances between peaks (FSR) may be fit exactly to customer specifications and a TEC package is available for thermal stability and minor adjustments of the bandpass frequency or wavelength.

The picoWave gives a multi-wavelength reference that enables real time wavelength calibration to picometer accuracy. Combining the uniform spacing of the FFP-I, a wavelength marker of a Fiber Bragg Grating, and a built-in TEC for thermal stability, the picoWave® makes an ideal calibrated wavelength reference over the entire scanning interval of the FBG-IS. As a consequence, a very good compensation for linearity effects can be carried out. Notice that due to the TEC, no ambient temperature influence is present here.

These both components make from the FBG-IS a high resolution and reliable system. The specifications are shown in Table 2.1.

Optical	
Number of Optical Channels	1
Maximum Number of FBG Sensors/Channel	31
Wavelength Range	1528 - 1568 nm
Calibrated Accuracy	+/- 10 pm
Repeatability	+/- 5 pm
Optical Power/Channel	-55 dBm (approximate)
Dynamic Range	12 dB
Resolution	< 1 pm
Scan Frequency	52.4 Hz
Minimum FBG Spacing	0.5 nm
Optical Connector	FC/SPC
Computer Interface Card	PC or PC Card (PCMCIA)
Operating Temperature	10° - 40° C
Dimensions	69 x 277 x 267 mm
Weight	2.7 kg

Table 2.1: Specifications of the FBG-IS

2.2. Software

The complete software, developed for the FMU-B-SFP has been adapted for this new hardware of MOI and further extended. Three different types of software programs have been developed: control software, calibration software and monitoring software. All developments have been done in Labview.

Note: the flow charts below describes the overall architecture of the different software programs developed to control, calibrate and interrogate the FBG-FOSs. The most critical modules are also described by a flow chart. It is not intended to report every small details on each chart but only the important steps to understand. This means that some steps in each module are sometimes voluntary omitted (e.g. save data) on the chart to keep it easy to read. These steps are simple and obvious when one's reads the diagram. When a flow chart does not explain much about a module, the module is described in a small paragraph.

2.2.1. Control software:

The control software aims to detect the position and the amplitude of the spectral responses on an optical line along which FBGs are connected. Fig. 2.3 shows the front panels of the Control software. As can be observed, the software displays the amplitude responses and can also measure the FBG wavelengths. Its main objective is to allow the user to control the integrity of an optical line. However, this software allows to calibrate the FBG(s) of an optical line vs an applied parameter. But it calibrates each FBG independently from the others. Fig. 2.4 shows the Flow chart diagram of the main module of the control software. The flow chart diagrams of the sub programs “2 Channels Oscilloscope – Optical Source & Switch” and “FBGISv35 Measurement Loop” are shown in Fig. 2.5 and Fig. 2.6. “2ch Oscilloscope – Optical Source & Switch.vi” performs the acquisition of the analogue signals of the FMU-B – MOIS (demodulator scan voltage, synchronisation signal, reflected optical spectrum), display the signals and drives the optical source and the optical switch of the FMU-B – MOIS. “FBGISv35 Measurement Loop” performs the measurement of the FBG wavelengths on the optical line, displays the results and drives the optical source and the optical switch of the FMU-B – MOIS.

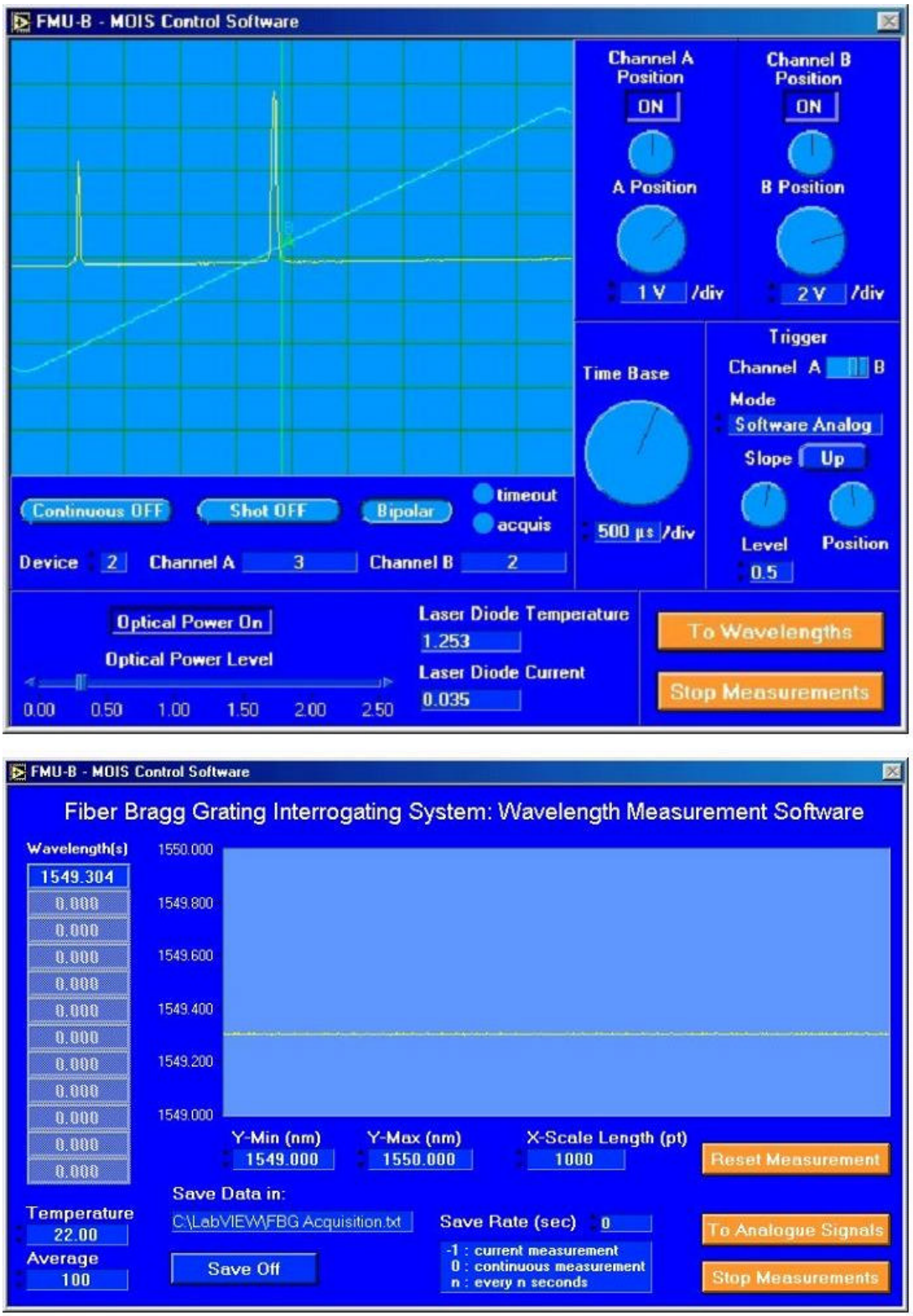

Fig. 2.3: Front panels of the FMU-B – MOIS control software

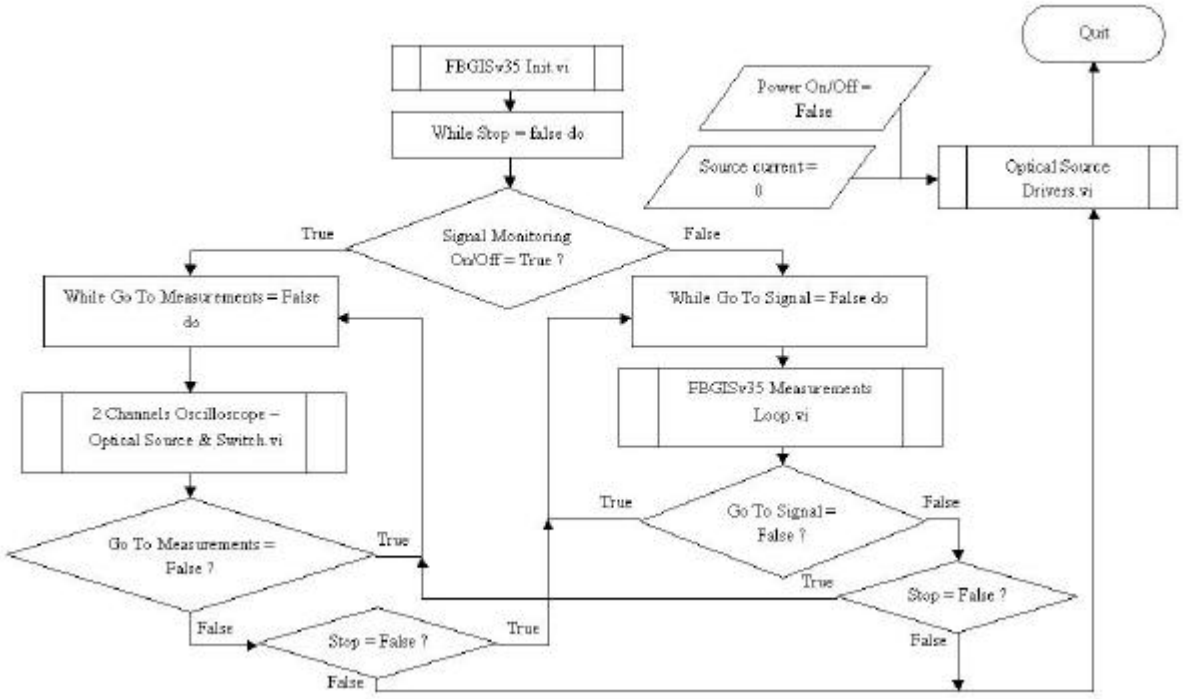

Fig. 2.4: Main module Control software for FMU-B-MOIS

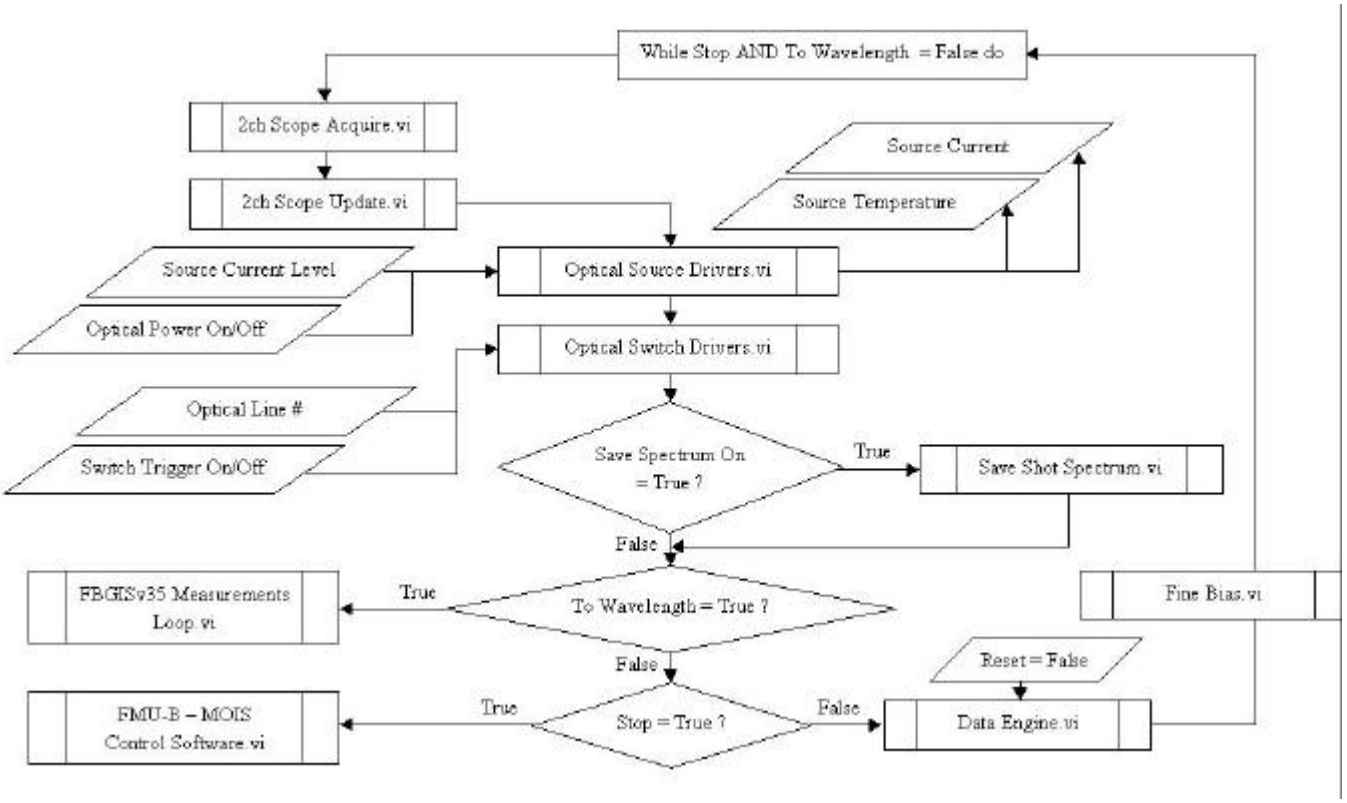

Fig. 2.5: "2 Channels Oscilloscope – Optical Source & Switch"

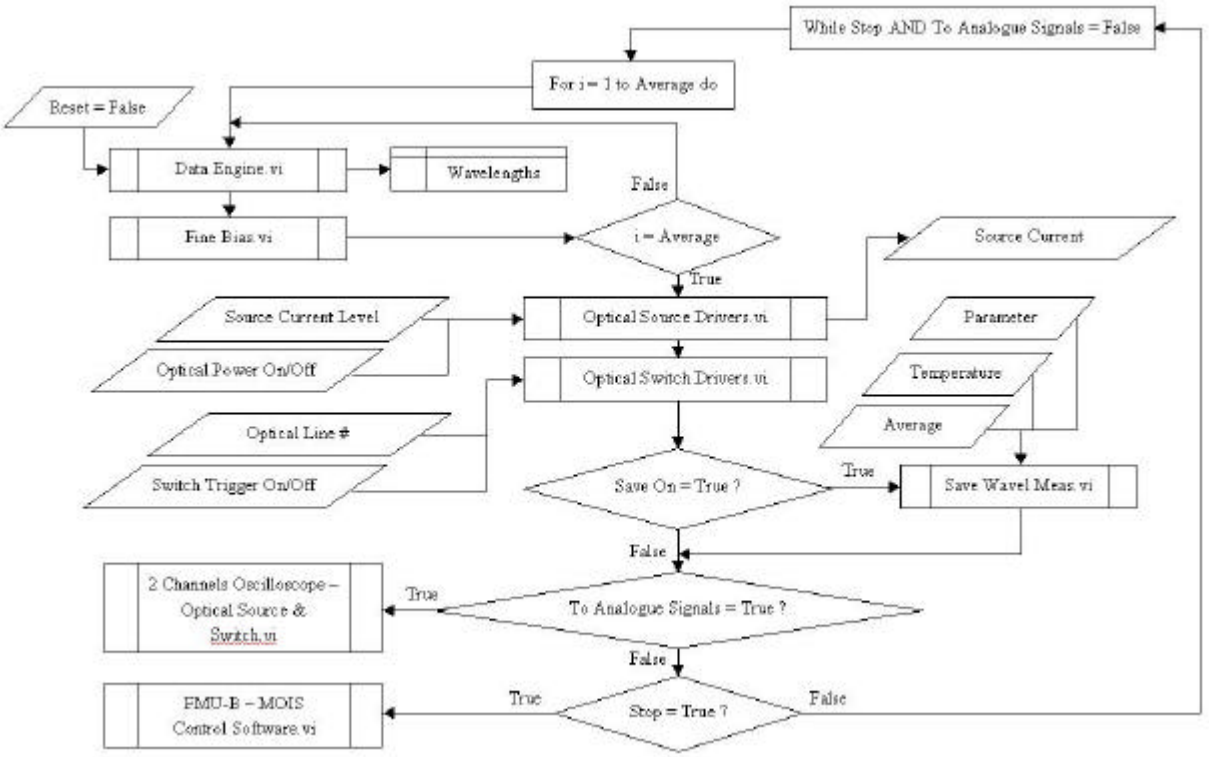

Fig. 2.6: "FBGISv35 Measurement Loop"

- FBGISv35 Init.vi, initialise the demodulator (MicronOptics board) loading the characteristics of the demodulator board integrated in the FMU-B – MOIS.
- Setup Parameters.vi, loads from the demodulator calibration file the settings of the demodulator A
- Address & Device #.vi, asks the user for the software and hardware configuration of the FMU-B – MOIS (which filter, which source, which switch, which interface cards, which input/output channels, which DIO ports, which communication kind etc.) and fetches the address of the interface cards in the system.
- Init Course Bias.vi, initial coarse tuning of the demodulator to stabilise its spectral window.
- Init Fine Bias.vi, initial fine tuning of the demodulator to stabilise its spectral window.
- 2ch Scope Acquire.vi, acquires the analogue input signal of the acquisition card according to the trigger mode selected on the front panel by the user.
- 2ch Scope Update.vi, updates the display on the front panel according to the mode selected by the user (continuous update or shot update).
- Data Engine.vi, acquires the wavelengths measured by the demodulator board through the DIO port of the acquisition card.
- Fine Bias.vi, stabilises the spectral window of the demodulator i.e. tunes the demodulator to compensate for its thermal drift.
- Optical Source Drivers.vi, stores the drivers of the different sources (possibly) implemented in the FMU-B – MOIS.
- Optical Switch Drivers.vi, stores the drivers of the different switches (possibly) implemented in the FMU-B – MOIS.

- Save Shot Spectrum.vi, save once the display.
- Save Wavel Meas.vi, save the measurements in a simple text file together with some parameters like date, time, environmental temperature, number of acquisition for averaging, possible parameter acting on the FBGs etc.

2.2.2. Calibration software

The calibration software allows to calibrate one FBG based sensor. Fig. 2.7 shows the front panel of the calibration software. As can be observed, the software allows to visualise and measure the signal the same way as the control software. But it can perform the calibration of a true FBG based sensor as developed at I.D. FOS Research and not only of one FBG or several FBGs. If the FBG is temperature compensated, the FBG-FOS implements two FBGs. To achieve differential temperature compensation, the wavelength difference between the FBGs is be measured along with its standard deviation. To achieve total temperature compensation, each FBG wavelength is measured separately along with its own standard deviation.

The calibration software has the same modules and diagrams as the control software and performs thus the same operations except that:

1. It calculates the difference between the two first Bragg wavelengths on the optical line which should also be the only Bragg wavelengths available in a temperature compensated FBG-FOS; It also calculates the standard deviation of the difference;
2. It saves the Bragg wavelengths and their difference along with their respective standard deviations, the parameter addressed by the FBG-FOS, environmental temperature and number of acquisitions for averaging through the module Save Calib Meas.vi;

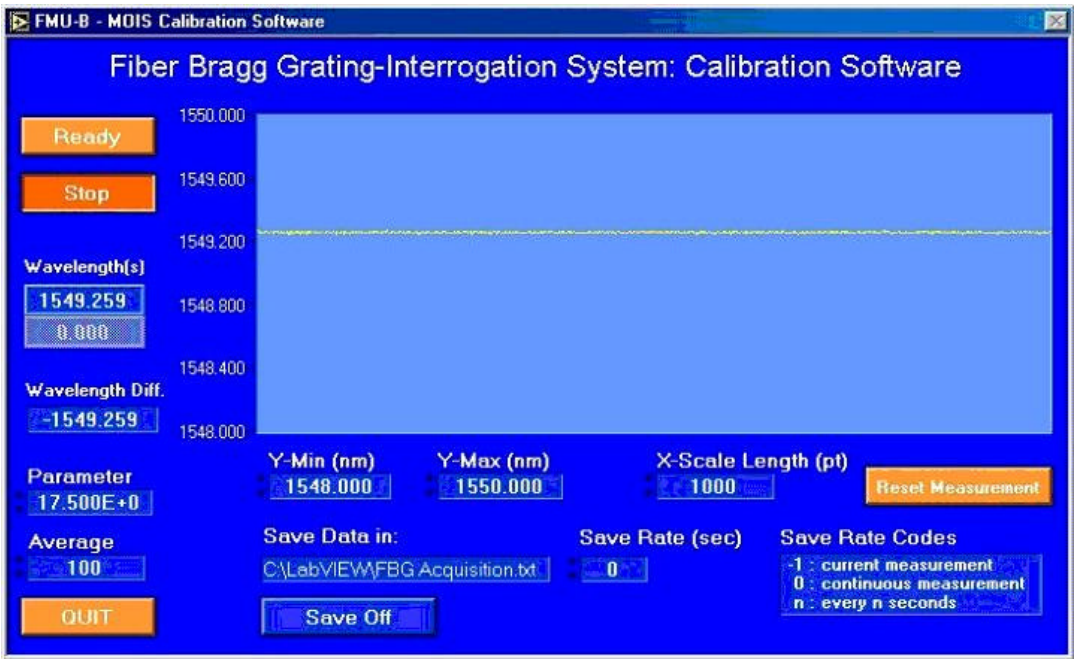

Fig. 2.7: Front panel of the FMU-B-MOIS calibration software.

2.2.3. Monitoring software

The monitoring software performs automatically continuous or periodical acquisition and storage of the measurements of FBG based sensors multiplexed in an fibre optic sensing network along several optical lines. A similar software program has also been developed for the FMU-SFP unit during a former project. Fig. 2.8 shows the flow chart diagram of the main module of the Monitoring Software. Three main setting parts can be distinguished: system settings, sensor settings and network settings. Once everything has been initialised, the measurements can be started. At this moment the "continuous measurements" subprogram starts working. "FBG continuous measurements" initialises the measurements sequence, starts "FBG Loop Measurements" and closes the acquisition sequence. The flow chart is shown in Fig. 2.9. Fig. 2.10 shows the FBG loop measurements flow chart which is a subprogram of the continuous measurements. "FBG Loop Measurements", performs continuously and/or periodically the demultiplexing of the FBG-FOSs (Wavelength Division Multiplexing) and performs continuously and/or periodically the measurements of the parameter addressed by the sensors on each optical line in the Fibre Optical sensing network, one line after each other.

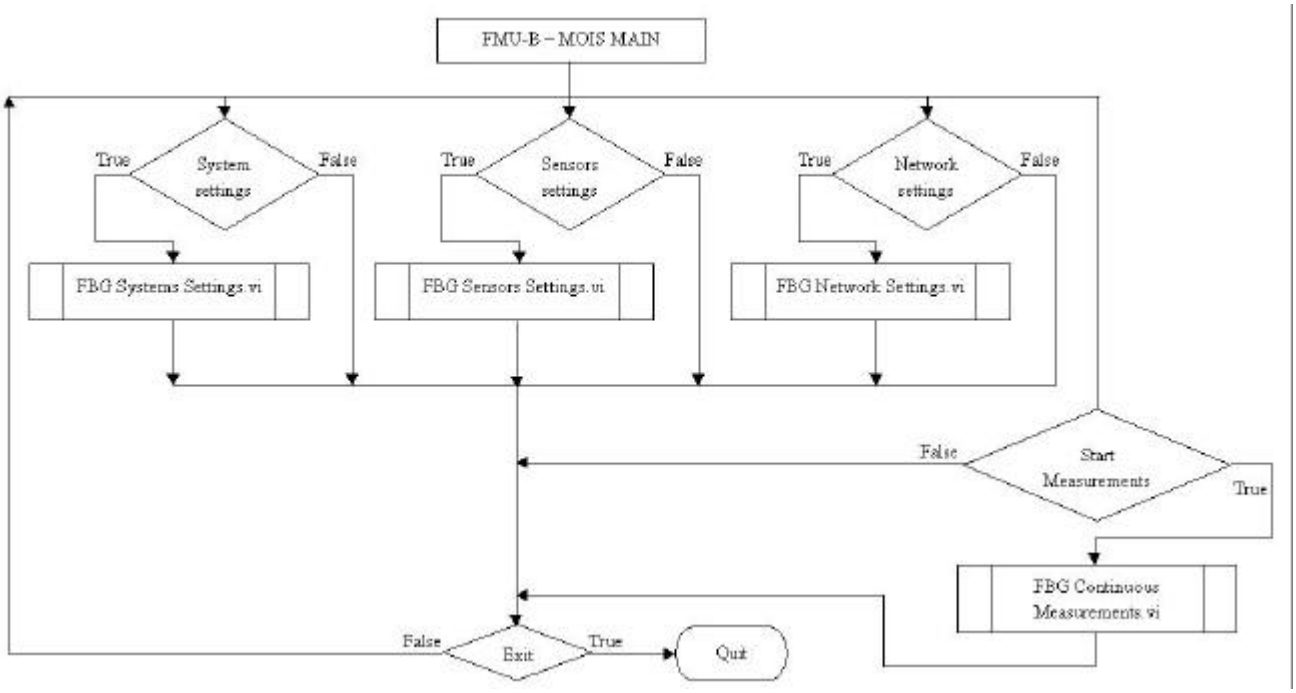

Fig. 2.8: Main module Monitoring Software

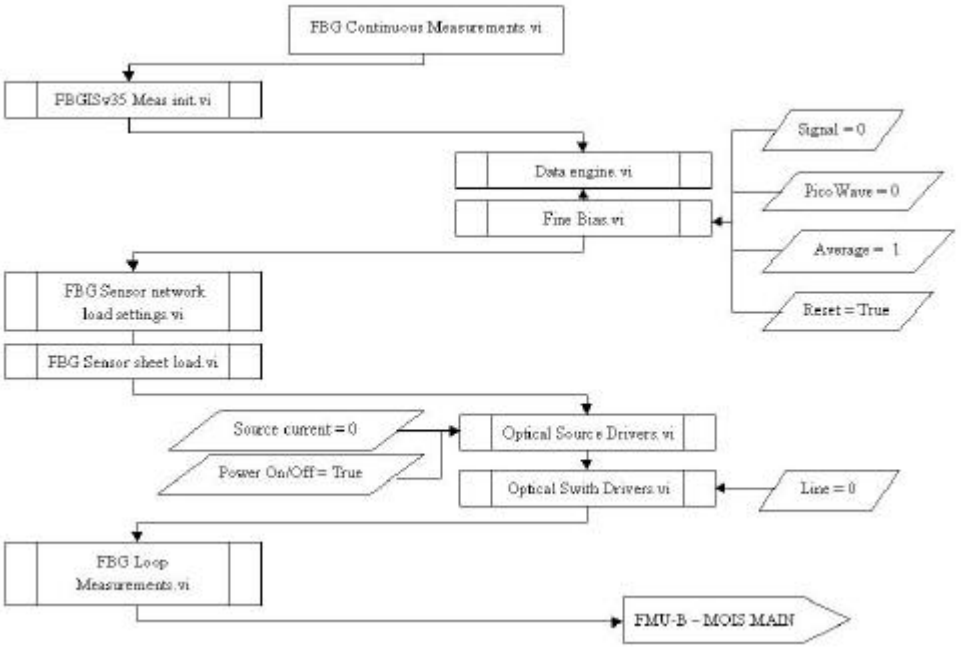

Fig. 2.9: FBG Continuous measurements

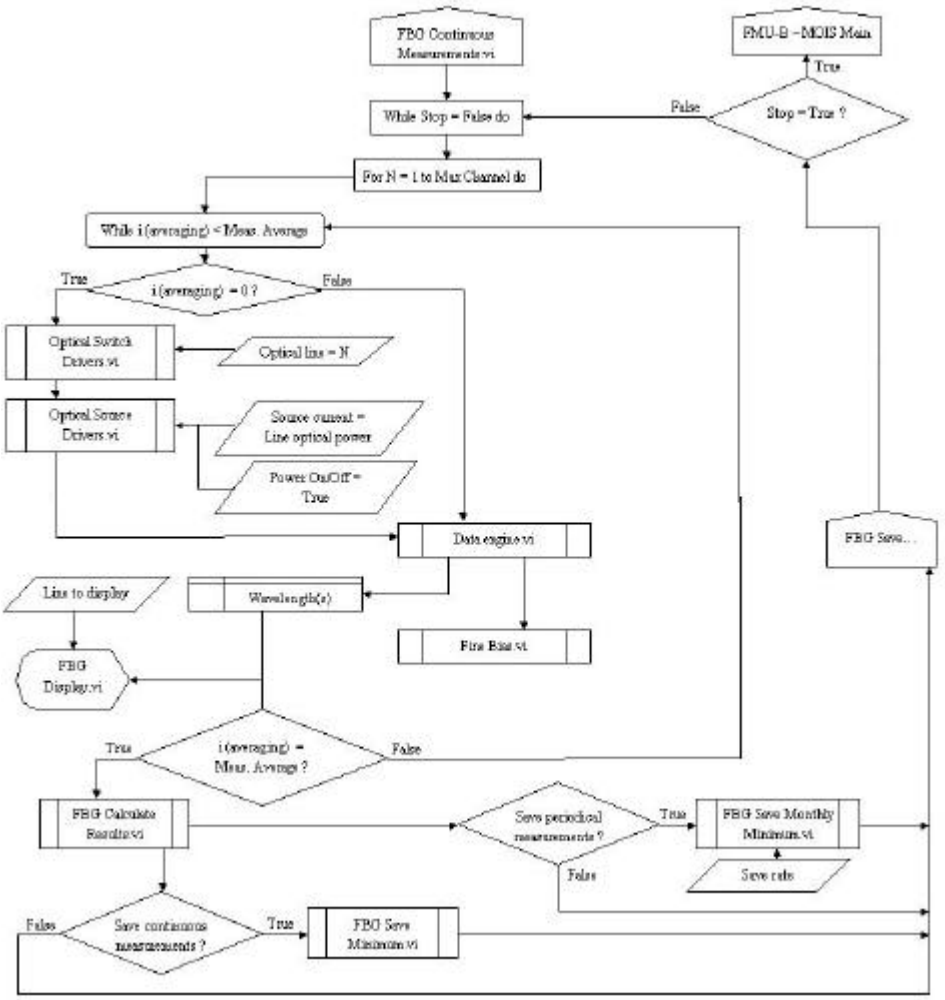

Fig. 2.10: FBG loop measurements

- FBG System Settings.vi, asks the end user for the hardware and software settings of the entire system “software + FMU-B – MOIS components” (which filter, which source which switch, which interface cards, which input/output channels, which DIO ports, which communication kind etc.).
- FBG System Test.vi, runs the software and hardware test of the entire system (software + FMU-B – MOIS components) and displays the results.
- FBG Sensors Settings.vi, asks the user for the calibration characteristics of the FBG-FOSs (one after each other) multiplexed in the FOSN monitored by the FMU-B – MOIS (which parameter is addressed, which nominal Bragg wavelength, which lower and upper spectral limits, which scale factor, which constant term etc.) and stores the calibration information in an “.cal” file the name of which is (partly) defined by the user.
- FBG Network Settings.vi, asks the user for the configuration of the FOSN monitored by the FMU-B – MOIS (which FBG-FOSs on each line, which optical power on each line etc.) and stores the configuration in an “.ini” file the name of which is defined by the user.
- FBG Sensor Network Load Settings, loads the configuration of the sensing network monitored by the FMU-B - MOIS.
- FBG Sensor Sheet Load, loads the calibration files of the FBG-FOSs interrogated by the FMU-B – MOIS.
- FBG Display.vi, displays the measurements (wavelengths or addressed parameters) on a graph; the user can choose the line he wants to read independently from the current interrogated line.
- FBG Calculate Results.vi, calculates with the raw data (sampling point locations) the FBGs’wavelengths, their shift with respect to their nominal wavelength and the parameter addressed by each sensor on the current line.
- FBG Save Minimum.vi, save continuously i.e. each measurement (only sampling point location and addressed parameter with its standard deviation) along with time, date, code error, error source, number of peaks on the line, number of acquisition for averaging etc.; creates one text data file per day; useful to make a survey of the system and identify a trouble when it arises.
- FBG Save Monthly Minimum.vi, save periodically at a rate specified by the user on the ront panel (only sampling point location and addressed parameter with its standard deviation) along with time, date, code error, error source, number of peaks on the line, number of acquisition for averaging etc.; creates one text data file per month; useful to make an analysis of the structure under survey with a reasonable amount of data.

2.3. Optical switching

At the beginning of the project, efforts have been put in the design of less expensive optical switches. A first type of an 1x3 optical switch by using different 1X2 optical switches in cascade has been designed.

The optical switch (OS) comprises two 1X2 optical switches driven by a CMOS or TTL logic. The required electronics has been soldered to interface the 1X2 switches to the computer through a very basic digital input/output interface card.

The first 1X2-OS (OS1) connects directly line 3 to the demodulator whereas it connects line 1 and line 2 through the second (cascaded) 1X2-OS (OS2). This configuration is required since the optical loss are the larger along line 3 and the signal need to propagate through as few as possible components in order to experience as low as possible optical loss. In any case, the amplitudes of the signals are all at least twice the detection threshold which is itself about

5 times the noise level. Fig. 2.11 summarises the optical switch configuration along with its optical budget. Fig. 2.12 shows some pictures of the actual developed 1X3 optical switch.

The control of the switch is done using a software program developed in Labview and has been integrated into the monitoring software described earlier.

The here developed optical switch has been used for the installation in GTS in Switzerland and is still functioning well.

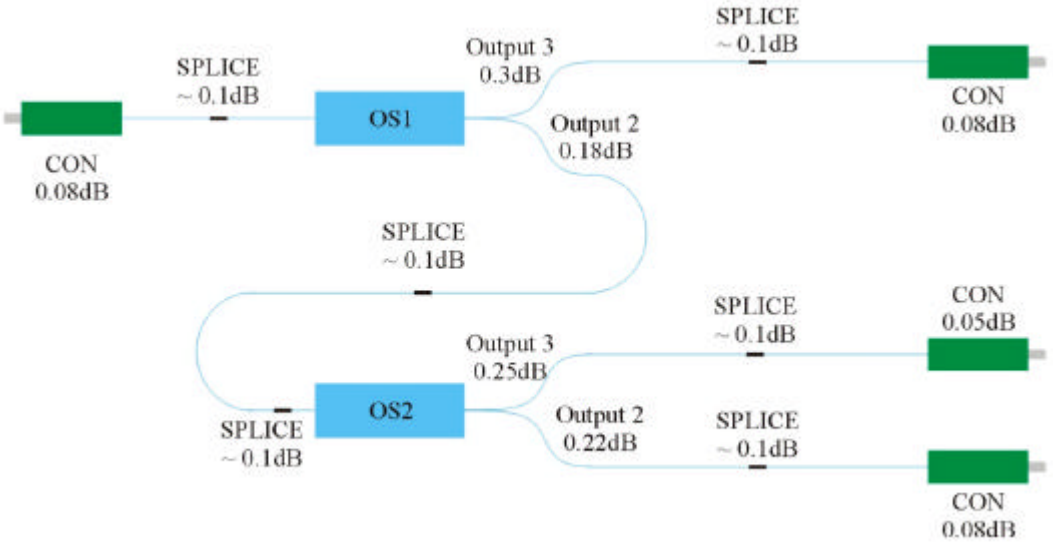

Fig. 2.11: Optical switch configuration and optical loss.

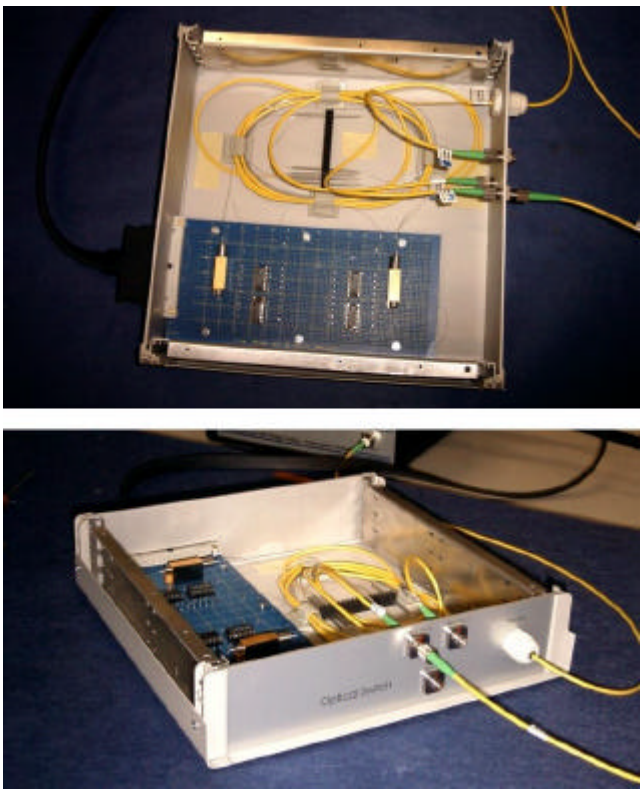

Fig. 2.12: 1 X 3 optical switch design.

More generally, this “shot” development was the preliminary to a larger scale development of an optical switch. Up to 4 lines, it is interesting to cascade several 1X2 OSs to build up a 1XN OS (N = 2, 3). This is modular and cost effective. Beyond 4 lines, a 1X4 OS cascaded with 1X2 OS(s) can be used to build up a 1XM OS (M = 4,5,6,7). From 8 lines, a 1X8 OS can be cascaded with 1X2 OS etc.

This way to build up an optical switch is flexible (exact required number of lines), electrically efficient since the driving signals are most of the time of the same kind (CMOS/TTL logic) and requires only slight adaptation of the board, optically very efficient since the power budget can be optimised and economically the best way to keep the cost as low as possible.

Nevertheless, due to new developments in the telecommunication market, it did became unfavourable to built the optical switches ourselves. Cost price of the optical switches has drastically be reduced during the last two years. It was therefore concluded to use commercial available OEM optical switches in stead of building our own switching system.

2.4. Evaluation of passive optical components

2.4.1. Connector evaluation

Different optical connector types have been investigated. During the former project, the FC/APC connectors have been extensively be used. The most important problem with the FC/APC connectors is the contamination with dust of the connectors during maintenance when the connectors are in a disconnected state. Therefore, alternatives have been searched and found: the E2000 connector.

The E2000 connector holds a single fiber in a ceramic ferrule. E2000’s are small form factor connectors with a moulded plastic body similar to that of an LC Connector. The E2000 also exhibits a push-pull latching mechanism, and integrates a protective cap over the ferrule, which acts as a dust shield and shields users from laser emissions, see Fig. 2.13. The protective cap is loaded with an integrated spring to ensure proper closing of the cap. A more technical drawing of the E2000 connector and adapter is shown in Fig. 2.14. Therefore, this type of connector is very well suited for usage in dusty environments.

The first field tests with these connectors have been performed in the mine at Morsleben. The experience so far is excellent. It has therefore been decided to use these connectors from now on for all sensing applications in dusty environments.

Fig. 2.13: Photo E2000 connector

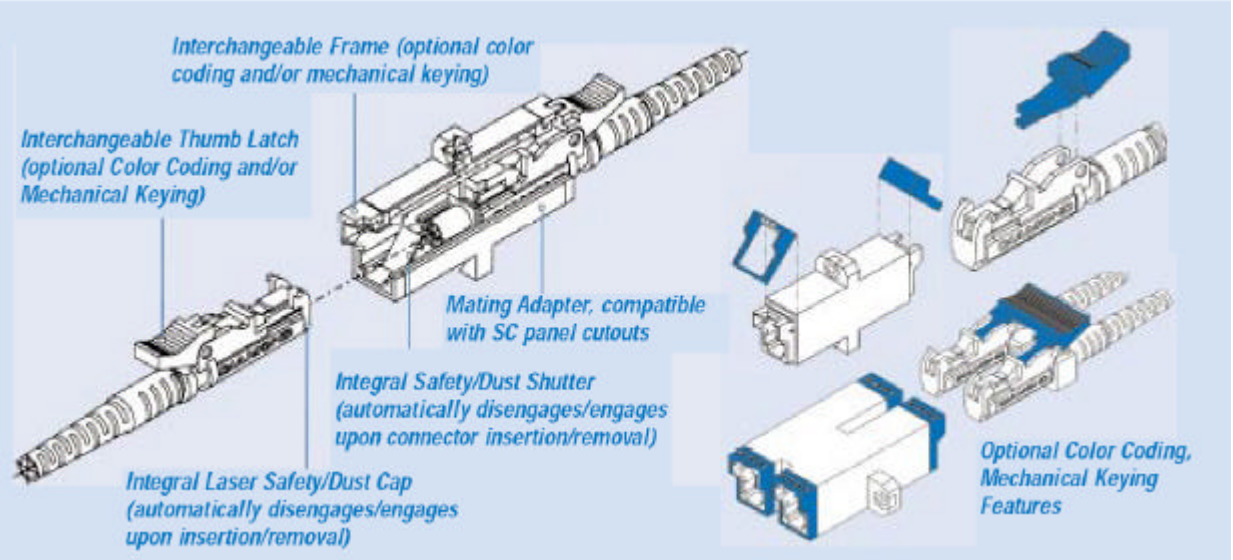

Fig. 2.14: Technical drawing E2000 connector

2.4.2. FBG evaluation

New developments in the telecommunication and sensing market, have lead to new types of Fibre Bragg Gratings. Three main types can be distinguished: mechanical gratings, UV transparent coated gratings and tower gratings.

2.4.2.1. Mechanical gratings

The mechanical gratings are the gratings that have been used so far in all the installed FO sensing networks. The process plan for mechanical gratings is shown in Fig. 2.15. As input for the process, a coated fibre with a photosensitive core is needed. Two different possibilities exist to get this photosensitivity. The first possibility is to use a high-doped fibre (for example high Ge doping). The disadvantage of this type of fibre is the high attenuation (several dB/km) what makes the fibre less interesting for sensing over long distances. The second possibility is using a standard telecom fibre. This fibre has a very low photo sensitivity but can be increased by hydrogenating the fibre prior to FBG writing. For example by putting the fibre for several hours in a hydrogen atmosphere at 150-200 bar at room temperature. After the annealing process (later in the process) the hydrogen is diffusing out and the induced defects (refraction index changes) remain. The use of this type of fibre has the advantage that after annealing a low attenuation can be obtained (<0.5 dB/km) what makes this type of fibre interesting for monitoring over long distances.

In a first step, the coating of the fibre is removed. This is necessary in order not to shield the UV light during the writing of the FBG from the core. Different process technologies are possible: mechanical, chemical, heating or laser removal. It needs to be mentioned here that the stripping process reduces the mechanical strength of the fibre.

Once the coating has been removed, a UV exposure will be performed in order to write the FBG in the core of the fibre. The UV pattern can be applied using the interferometric or the phase mask method. With this method mostly high reflectivity gratings (>90 %) can be produced.

The next step is an annealing step. Due to thermal depopulation of trapped states the reflectivity of the grating shows initially a strong decrease. In order to stabilise the grating reflectivity, the FBG is annealed.

Finally, the fibre will be recoated in order to protect the fibre. Different materials can be used as recoating material: Ormocer, Acrylate, Polyimde, …. The coating can be applied using a thermal or UV-curing process.

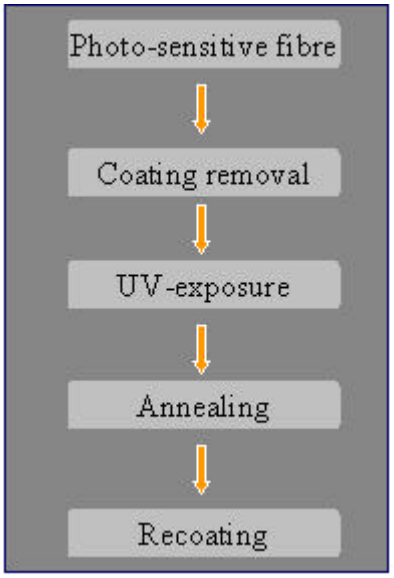

Fig. 2.15: Process steps mechanical gratings.

This type of gratings has been used so far in all applications. The most important disadvantage of the gratings is the low mechanical strength (typically a maximum strain of 1% is the limit). This reduces the reliability of the sensors, especially when the grating is experiencing high strain levels. Note that higher strain levels can be achieved by some suppliers but due to the special procedure that needs then to be followed, the price almost doubles, making the sensors very expensive.

2.4.2.2. UV-transparent coated fibre gratings

Recently a new type of fibre is introduced on the market: a UV-transparent coated fibre. This fibre does has the advantage that the coating must not be removed prior to UV exposure. As a consequence, the production process becomes simpler, see Fig. 2.16. The coating removal as well as the recoating does not need to be performed anymore with this type of fibre. Due to the fact that no stripping has to be applied, the mechanical strength of the fibre is expected to be much better for this type of fibre.

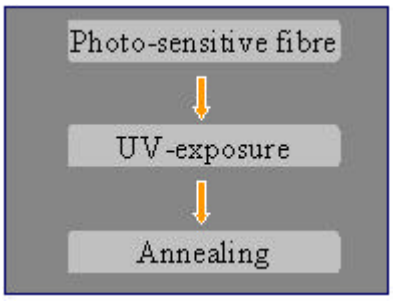

Fig. 2.16: Process steps UV-transparent coated fibre gratings

Due to the interesting high strength properties, this fibre has been put under investigation. A FBG has been written in the fibre after the fibre has been hydrogen loaded. The grating has been written using a wavelength of 248 nm. The writing of a FBG has been successful. A reflectivity around 85% could be obtained. Higher reflectivity's could not be achieved. The reflectivity seemed to saturate around this value.

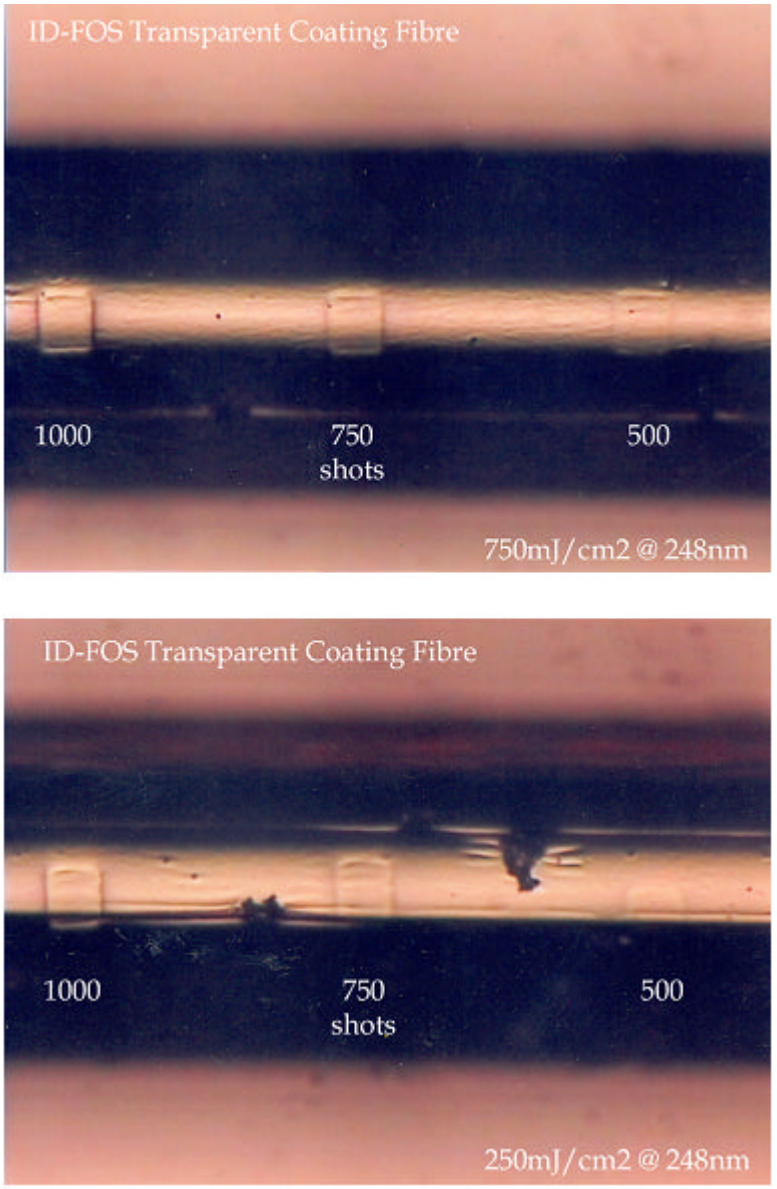

Fig. 2.17: Coating adhesion experiments of UV transparent coated fibre

Furthermore, the quality of the coating has also been analysed. The coating has been radiated using pulse energies of 250 mJ/cm^2 and 750 mJ/cm^2 and this for 500, 750 and 1000 pulses. After the radiation experiments the coating has been analysed using a Scanning Electron Microscope (SEM). Fig. 2.17 shows the result. As can be observed, ablation effects of the coating did occur even for the smallest dose (250 mJ/cm^2 and 500 shots). This ablation can cause problems with respect to the protection of the fibre. As a consequence, more fine tuning of this type of fibre is required before the fibre can be used in sensing applications.

2.4.2.3. Tower gratings

The tower grating production process is a process that combines the drawing of the fibre and the writing of the FBG.

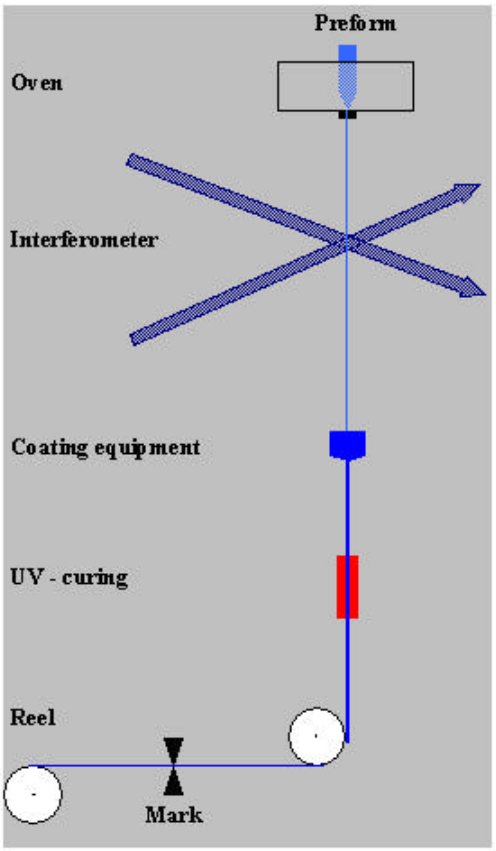

Fig. 2.18: Tower grating production set-up

Fig. 2.18 shows the set-up of this production process. The input of the process is a pre-form that is used for drawing fibres. The pre-form needs to be highly doped in order to obtain a good photosensitivity of the fibre. By heating the pre-form to 2000°C, the pulling and formation of the fibre will be initiated. In the way down, the fibre crosses the optical axis of an excimer-laser and the interferometer. Using a pulse selector and taking into account the draw speed, FBG's can be written on well-determined places in the fibre. Notice that due to the low available exposure time (15-25 ns), an excimer-laser with high pulse energy is used. The gratings will have low reflectivities (<10%). After writing the grating, the fibre will be coated. To do this, the fibre enters a kind of bath with the coating material and passes then a UV-curing or thermal region in order to harden out the coating. Finally, the location of the FBG is marked automatically and the fibre is reeled on a drum. The advantage of tower gratings is that the FBG is written into the fibre prior to the coating process. As a consequence, no stripping is needed what results in a good mechanical strength.

Tests have been performed to investigate the mechanical strength of the fibre. Strain levels up to 6% could be obtained without breaking the fibre. This type of fibre is therefore very interesting for future sensors applications.

3. Field trials

3.1. Konrad mine

In the framework of the project, a follow-up of the first test installation at the Konrad mine in Germany in terms of re-investigation of the sensing system after recuperation has been carried out. All other results of the tests have already been reported in the final report of the previous R&D project [14]. At 4 and 5 June 2003, the system has been dismantled. The sensors that could be recuperated have been investigated.

3.1.1. Sensor system

In the year 1999, a demonstration system of the fibre optical sensing network system has been installed in the Konrad mine in the framework of the LOMOS project. The fibre optic sensing network consists of 22 FBG-based sensors distributed along 6 optical lines:

1. Line 1: 3 anchored displacement sensors
2. Line 2: 1 strain cable with 3 sensing heads
3. Line 3: 4 surface displacement sensors
4. Line 4: 4 surface displacement sensors
5. Line 5: 4 temperature sensors
6. Line 6: 4 water leakage sensors

Fig. 3.1 shows the configuration and position of the sensors in the gallery. The polygon is measured using lines 3 and 4 and is used to observe the gallery deformation. The sensors of lines 1 and 2 are used for measuring the strain in the underground layers. The temperature cells are also positioned in a borehole and give the temperature as function of depth.

In order to validate the system, some conventional (electronic) reference sensors have been installed for line 1 and line 5. For line 3 and line 4, manual measurements have been performed from time to time in order to compare to the FO sensors. The results are reported in [14].

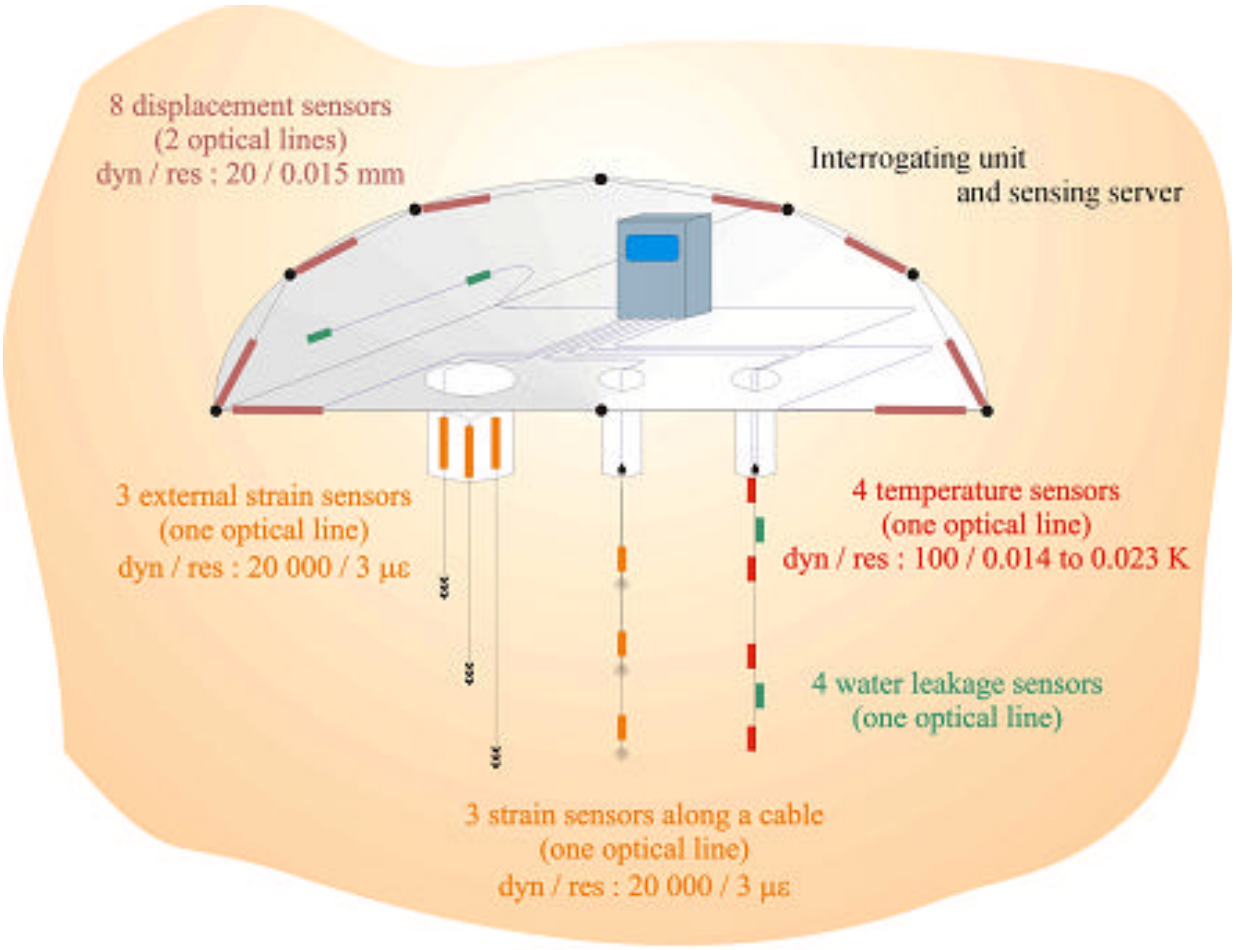

Fig. 2.1: Fibre optic sensing network at the Konrad mine.

Fig. 2.2: Photo of the fibre optic sensing network at the Konrad mine.

3.1.2. Dismantling results

On 3 and 4 June 2003, the system at Konrad has been dismantled. All sensors that could be retrieved have been taken to the laboratories of I.D. FOS Research for further investigation. A recalibration of the three different types of sensors (Water Leakage, temperature and displacement) has been carried out and the possible contamination of the inner parts has been investigated.

Fig. 3.3 shows the recalibration results of sensor SD-Lomos-03. The results are compared to the calibration results of the same sensor before installation. It can be seen that the new calibration also shows a linear relation without no significant hysteresis effect. As a consequence the sensor is still functioning well. However, when comparing the results with the previous calibration results, a change in sensitivity factor can be observed, from 0.096 nm/mm to 0.099 nm/mm. This change can possibly be explained due to the difference in interrogation system that is used to carry out the calibrations. The first calibration results have been calibrated using the FMU-B-SFP while the new calibration has been performed using the FMU-B-MOIS system. As already explained, the FMU-B-SFP did show some shortcomings with respect to linearity and accuracy compared to the FMU-B-MOIS. This could be the cause of the here observed discrepancy.

Fig. 3.4 shows the recalibration result of the temperature sensor FBG-T-Lomos 02. A very nice linear relation can be found and without a significant hysteresis. The sensor response is therefore again showing a good response. When comparing the results with the former calibration results, an offset can be found. The nature of this offset can also be explained by the shortcomings of the former interrogation system: the FMU-B-SFP unit. Furthermore, the response of the water leakage sensor has also been checked by putting the sensor into water for a while, followed by a drying period. Also for this sensor, a proper functioning can be observed.

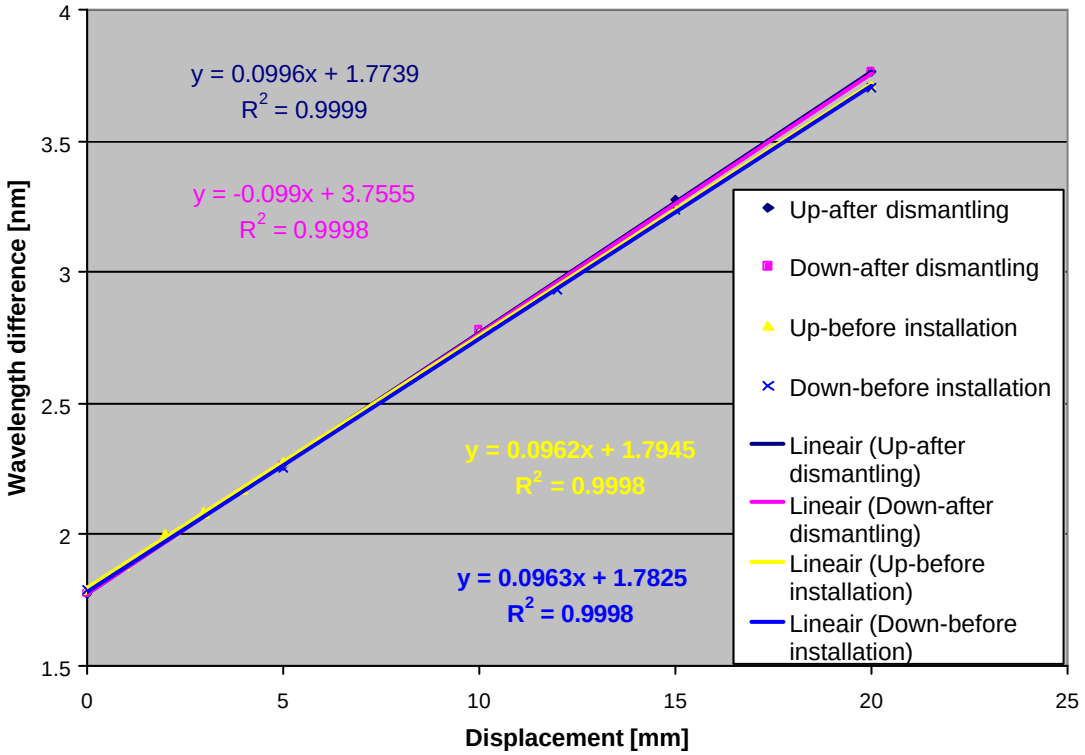

Fig. 3.3: Recalibration results SD-Lomos-03

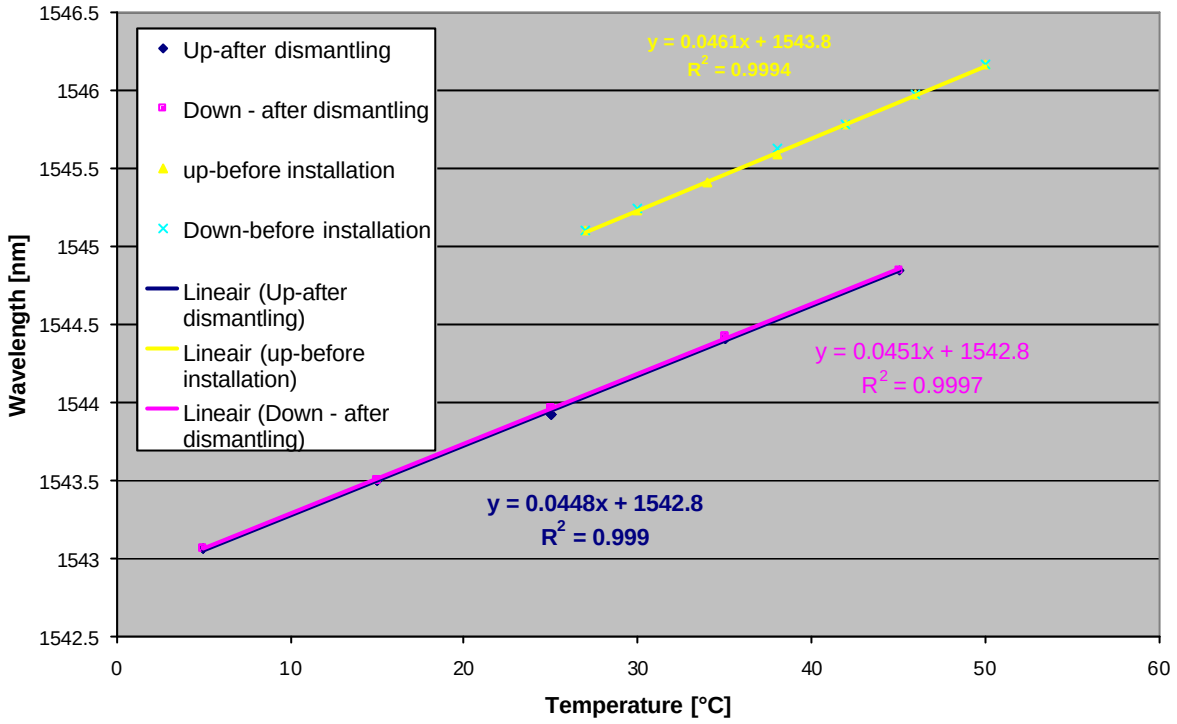

Fig. 3.4: Recalibration result FBG-T-Lomos 02

Finally, the interior of the different sensor has also been investigated. Fig. 3.5 and Fig. 3.6 do show the interior of the displacement and temperature sensors used in the Konrad mine. As can be observed, no contamination of the inner parts is visible. As a consequence, the packaging of the sensors have resisted very well the harsh and dusty environment in the Konrad mine. Fig. 3.7 shows the inner part of the water leakage sensor. A contamination is here of course observed due to the fact that the sensor is designed to let the water infiltrate. Only a filter is used to reduce the contamination. Fig. 3.8 shows a zoom of the sensing head of the water leakage sensor. It can be observed that this head is still quite clean what demonstrates that the filter is functioning well.

Fig. 3.5: Photo of the interior of the displacement cell FBG-D-LOMOS 03 .

Fig. 3.6: Photo of the interior of a temperature sensor used in Konrad

Fig. 3.7: Photo of the interior of the water leakage sensor FBG-WL-Lomos 01

Fig. 3.8: Zoom of the interior of the water leakage sensor FBG-WL-Lomos 01

Based on the previous results it can be concluded that the sensors still show an excellent behaviour, what subscribes the long life time expectation of these fibre optical sensors. It is also proven that the housing do give an excellent protection against contamination of the inner mechanical parts of the sensors.

3.2. Grimsel Test Site (GTS)

3.2.1. Sensors

The initially planned configuration for implementation in the GMT is depicted in Fig. 3.9 and consisted in two optical sensing lines:

- Line 1: three water leakage sensors (W-FOS) and one total earth pressure sensor (MTP-FOS) at the end of the line; one W-FOS lies in the sand (layer 13) while the two remaining W-FOSs and the MTP-FOS lay in the bentonite-sand (layer 12);

- Line 2 : two temperature sensors (T-FOS) and one pore water pressure sensor (MPWP-FOS) at the end of the line; one T-FOS in the backfill layer, the other T-FOS in the sand (layer 13) and the MPWP-FOS in the bentonite-sand (layer 12).

This configuration allowed to implement all the sensor on the same spectral line even if two physical lines are deployed behind a 1X2 (one input X two outputs) optical coupler. The advantage was the use of a low power optical source (included in the demodulator) without any optical switch which kept the budget of the installation low enough. The drawback was the limited spectral allocation for each sensor given the fact that the sensors are all multiplexed on one spectral line. This can be quite restricting regarding the dynamic-resolution comprise which depends on the width of the sensor spectral allocation.

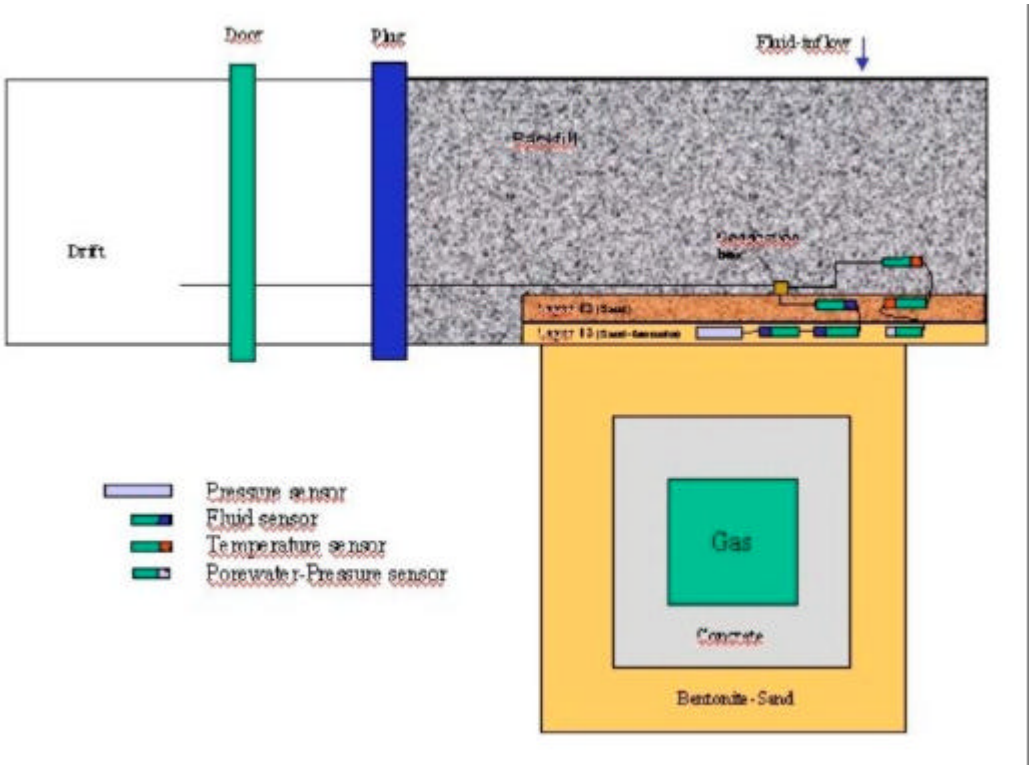

Fig. 3.9: Initially planned configuration at the GTS (GMT).

However, the configuration changed quite quickly and a 1X3 optical switch was required. This allowed to distribute the sensors among three physical/optical and spectral lines. This also released the compromise spectral allocation-dynamic-resolution of each sensor. The expected temperature at the GTS is 12 to 14°C, the expected pressure 3 to 4 bar and the relative humidity of interest is 70 to 100%. As a result, the final targeted specifications are summarised in Table 3.1.

Sensor	Dynamic Range	Line and Layer
W-FOS 1	On/off water leakage sensor	Line 1 – Layer 12
MPWP-FOS	0-5 bar	Line 1 – Layer 12
W-FOS 2	On/off water leakage sensor	Line 2 – Layer 12
MTP-FOS	0-5 bar	Line 2 – Layer 12
W-FOS 3	On/off water leakage sensor	Line 3 – Layer 13
T-FOS 1	0-50 °C	Line 3 – Layer 13
T-FOS 2	0-50 °C	Line 3 – Layer 13

Table 3.1: Targeted sensor specifications and network configuration for the GTS.

The sensors were produced according to these specifications and tested/calibrated. Fig. 3.10 shows the calibration of the MPWP-FOS sensor. As can be observed, the calibration curve is perfect (linearity, hysteresis etc.). The calibration of the MTP-FOS (Fig. 3.11) is almost as perfect as the calibration of the MPWP-FOS. The two sensing cells (membrane + FBG) of these sensors are strictly the same, however, the MTP-FOS is connected to a pressure pad filled with oil which gives rise to a very small hysteresis at least larger than the hysteresis of the MPWP-FOS.

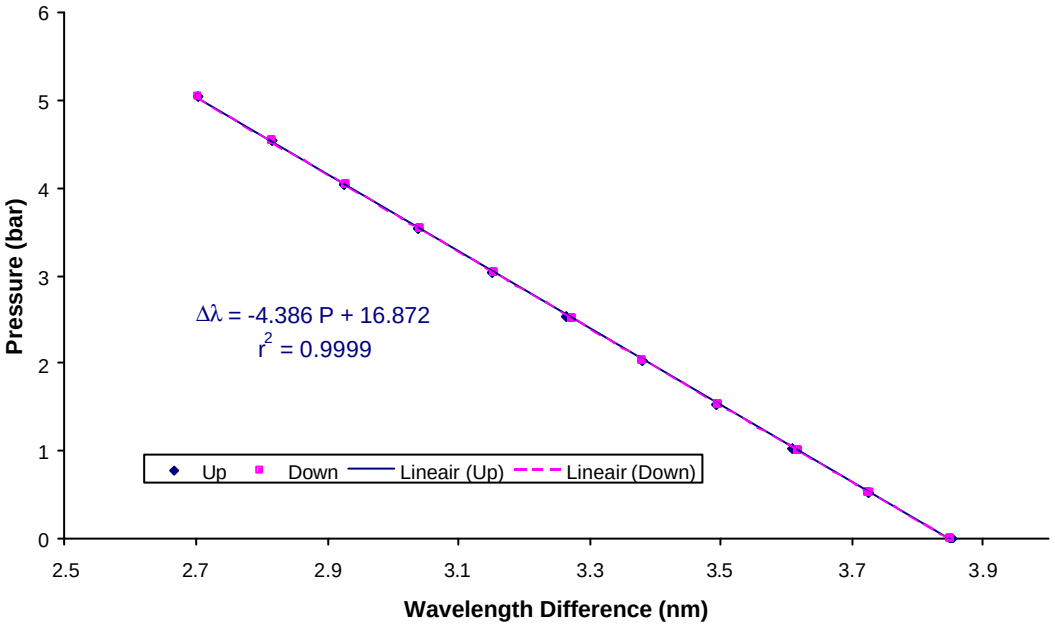

Fig. 3.10: Calibration result MPWP-FOS

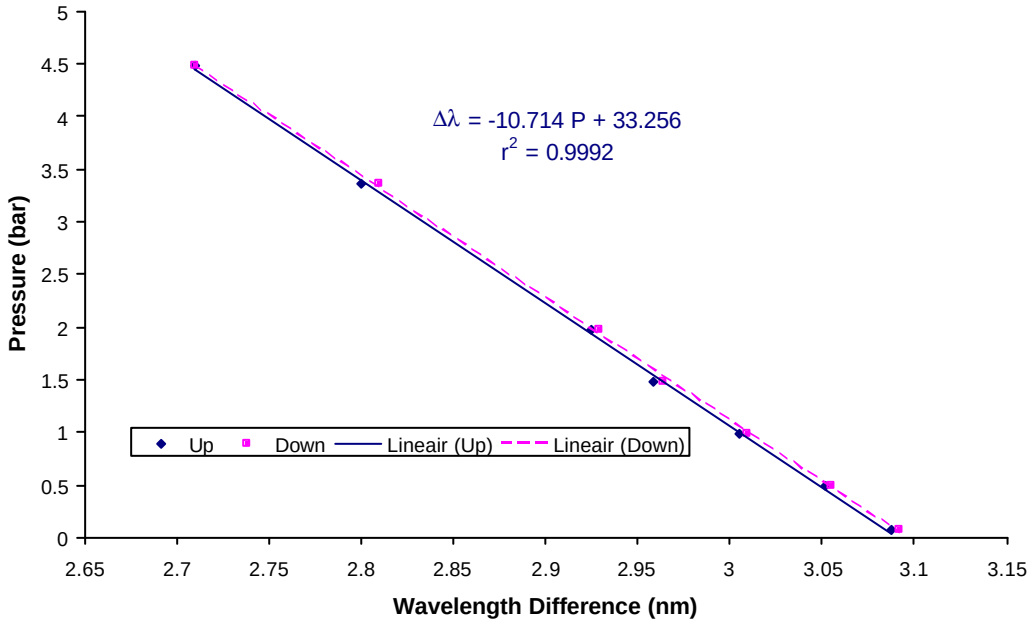

Fig. 3.11: Calibration result MTP-FOS

The temperature sensors have been warmed up and cooled down several times so as the different mechanical part of the mechanism to find their final position and to remove any

possible mechanical slacks. Then, a fine calibration around the temperature range of interest has been achieved. As can be seen in Fig. 3.12 and Fig. 3.13, the calibration curves show a perfect linear behaviour with no significant hysteresis effect.

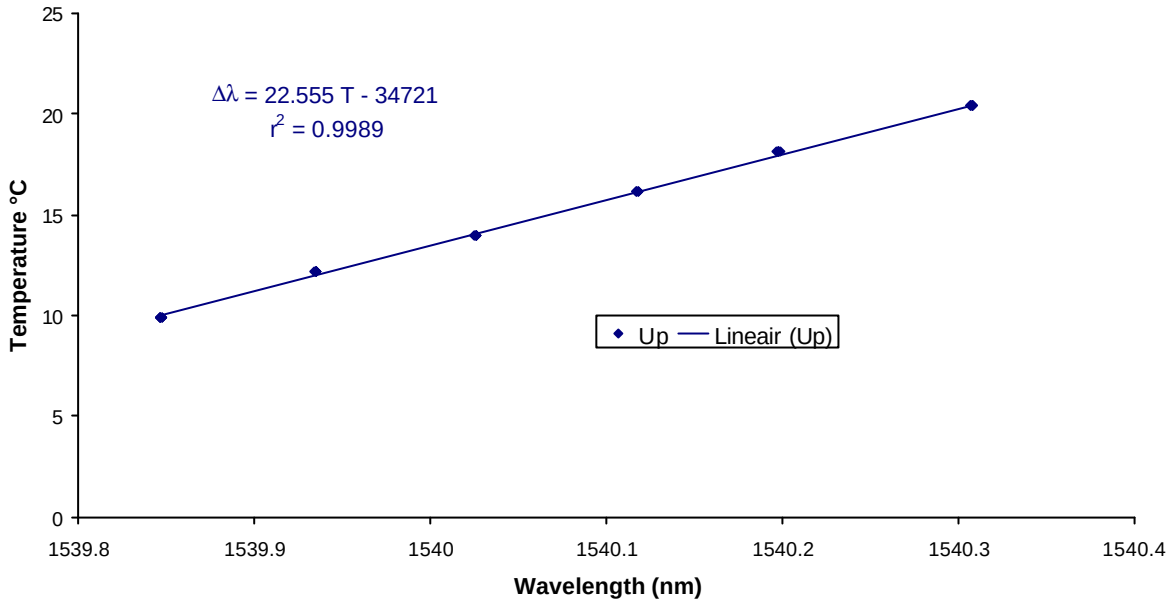

Fig. 3.12: Calibration result T-FOS 1

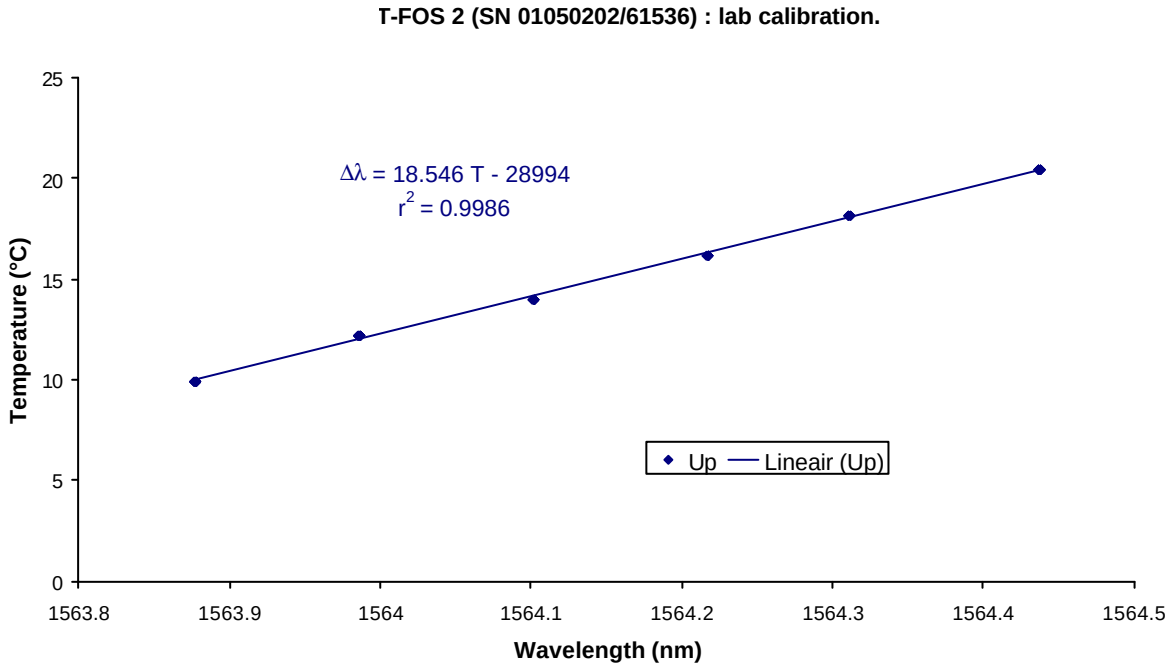

Fig. 3.13: Calibration result T-FOS 2

The W-FOS sensors have been tested as ON/OFF water leakage sensors. Their responses are as expected. Some of them do not dry down to the initial wavelength offset. This behaviour has already been observed in a former characterisation.

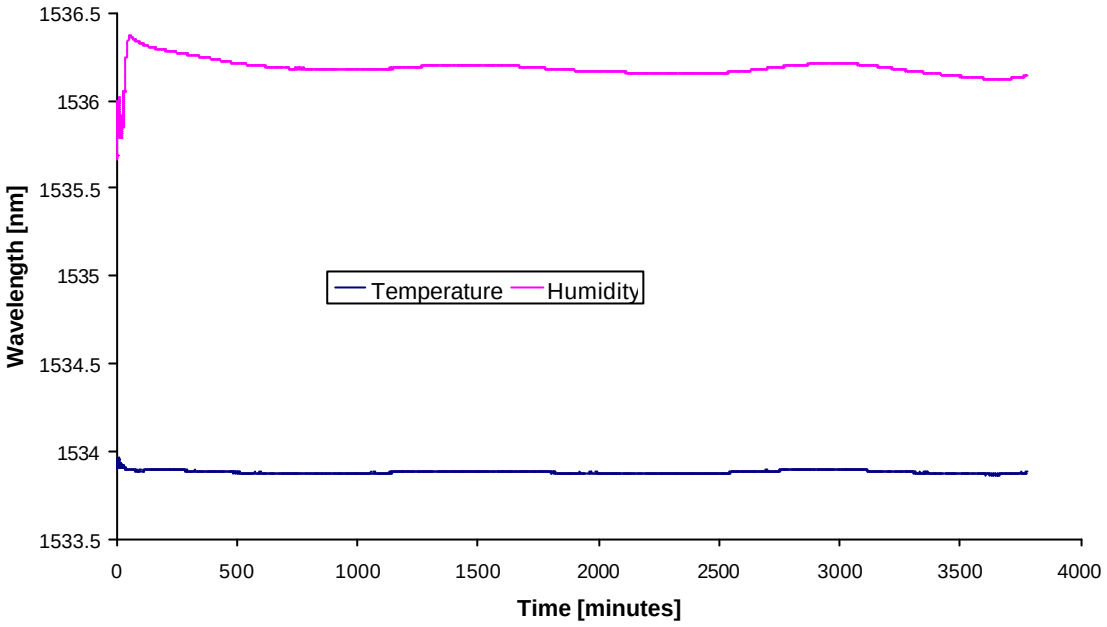

Fig. 3.14: Calibration result W-FOS 1

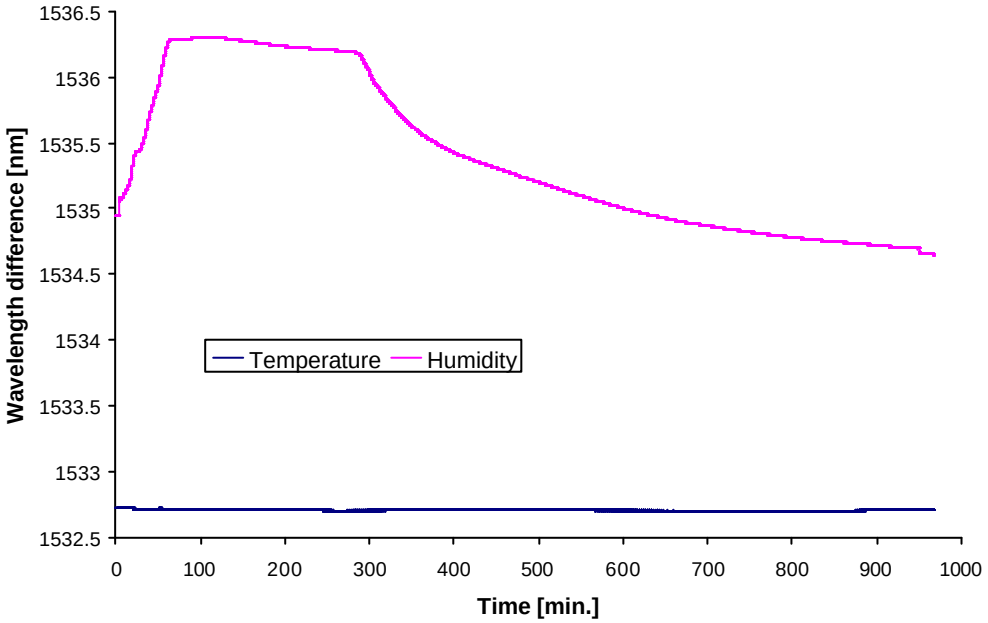

Fig. 3.15: Calibration result W-FOS 2

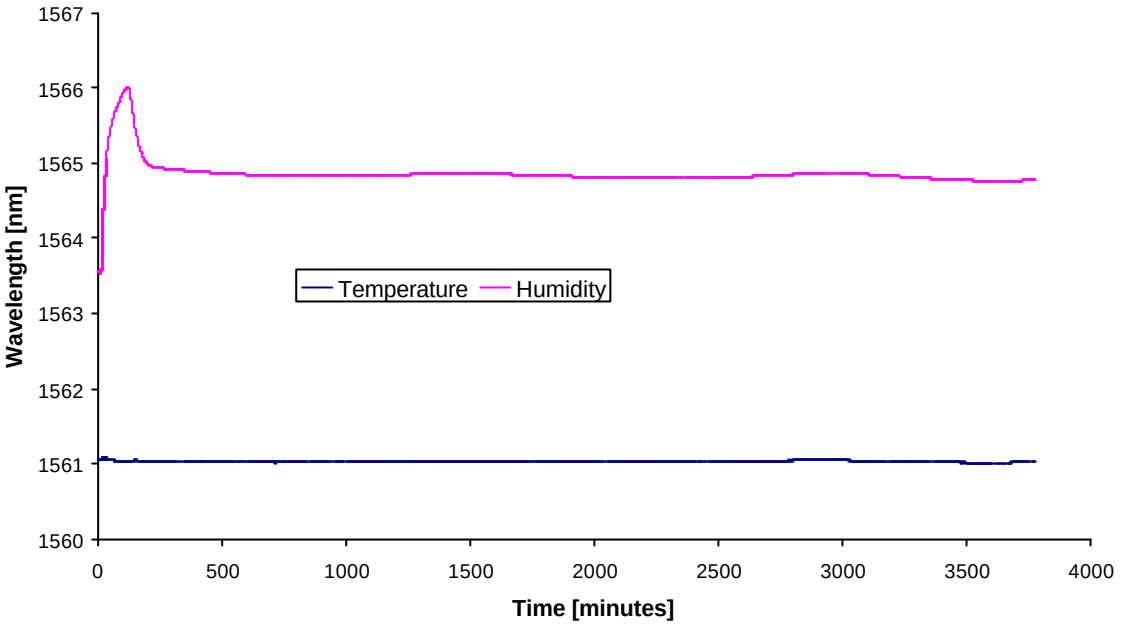

Fig. 3.16: Calibration result W-FOS 3

The sensors are usually connected with normal outdoor telecom cables. The few centimetres of the sensor cable pigtail at the end of its housing is a 6/3 nylon tubing (outer diameter 6 mm, inner diameter 3 mm). The telecom cable spliced with the sensor fibre coming out of the nylon tubing is mechanically maintained to the 6/3 nylon tubing by a 10/8 nylon tubing which is slid around both the telecom cable and the 6/3 nylon tubing after the splice is completed. This 10/8 nylon tubing protects the splice which is loose inside and a thermo-shrinkable tube with silicon on its inner face seals tightly the whole assembly. Fig. 3.17 depicts the usual pigtailing technique of the sensors.

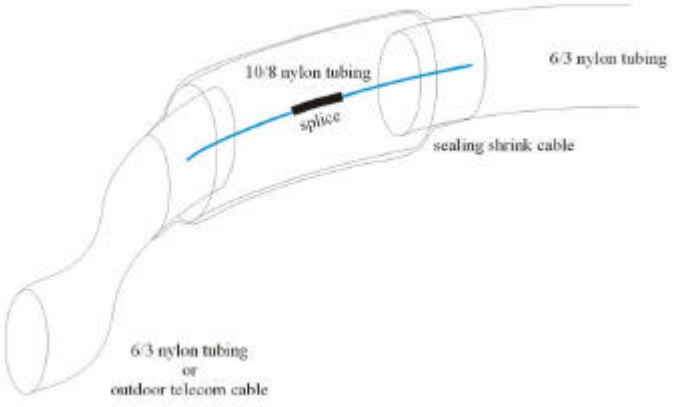

Fig. 3.17: Usual pigtailing technique of the FBG-FOSs.

Note: if the sensors have to be cast in a grouted borehole, the telecom cable is replaced by another 6/3 nylon tubing which can withstand the temperature and the pressure of the grout as it cures.

The same principle has been implemented at the GTS. However, due to a lack of space, it was impossible to use wound tubing or cables. The sensors on each line have been interconnected by metallic straight protective tubes 6 mm in diameter and with 10 to 20 cm in length (Fig. 3.18).

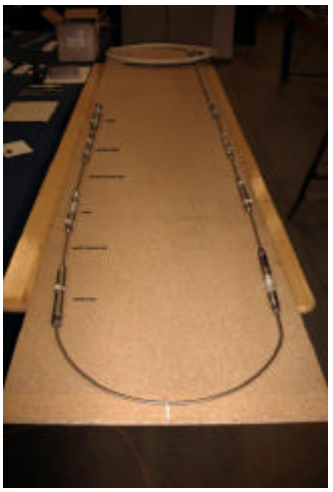

Fig. 3.18: Protective tubes and bridges along line 3.

In layer 12, a intermediate piece of bentonite has been used to bridge two protective tubes to each other and to allow these tubes to be slid around the splice once it is completed (Fig. 3.19). In layer 13, other metallic tubes with a larger diameter have been used to bridge two protective tubes with each other (Fig. 3.18).

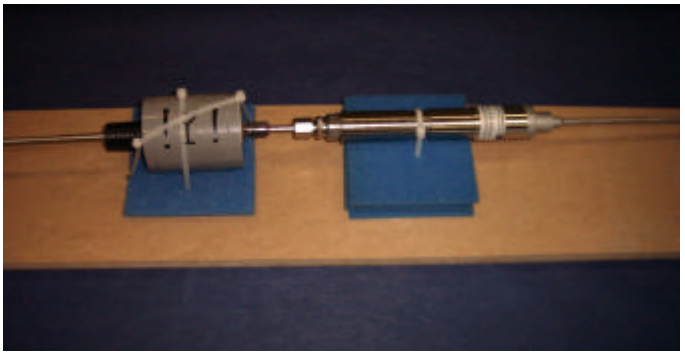

Fig. 3.19: Bentonite bridge in layer 12.

Finally, the sensing line was terminated by a special cap closing the riser along which the normal sensing line pigtail could be pulled to the location of the interrogating unit (Fig. 3.20).

Fig. 3.20: End sensing line riser cap.

Every tube has been close inside by a thick cap of glue and the pressure tightness has been successfully tested in the lab up to 20 bar.

In general, this special way of interconnecting the sensors was quite difficult to achieve. If one splice was not good enough, a few fibre reserve and spacing between the protective tubing was left to re-splice the optical line. It is always better to have enough fibre reserve along the line which can be wound on place to make the reliable optical connections in an easy way.

3.2.2. Interrogation system

The interrogation system used at GTS is an FMU-B – MOIS unit. It is connected to the 1X3 OS described in paragraph 2.3. Since no optical source is required, the demodulator and the OS are housed into separate boxes. A laptop runs the FMU-B – MOIS monitoring software and monitors the overall unit. The system is shown in Fig. 3.21 and has been located in a technical cabinet.

Fig. 3.21: FMU-B – MOIS unit at the GTS.

3.2.3. Installation of sensors at the GTS.

The installation of the sensor has been completed in two steps: line 1and 2 in layer 12 in April 2001 and line 3 in layer 13 a couple of weeks later. The interrogating unit has been installed in July. A portable unit of I.D. FOS Research has been used to control the sensors during the different phases of the installation.

Before installing the lines, they have been checked at the premises of SolExperts in a pressure chamber. In general, the sensors, their interconnections and the pigtails withstood the pressure applied and where validated for installation.

However, around the bentonite bridge of line 1, a small leakage appeared and the connection broke. This did not happened with the bentonite bridge of line 2. It is assumed that the tough splicing and connecting procedure made it difficult to reliably seal the sensing lines in a repeatable way. If this metallic protective tubes have to be used again, the connecting procedure has to be revised. The MPWP-FOS could fortunately be retrieved and has been connected at the end of line 3 in layer 13.

When the team of I.D. FOS Research went back to GTS to install line 3, the already installed line 1 and line 2 have been interrogated. It appeared that line 2 was broken around the bentonite bridge since the W-FOS 3 was still detected whereas the MTP-FOS was not any more. It is believed that the bentonite bridge broke during the levelling of layer 12 and broke

the optical line. The machinery used for the stabilisation of the different layers caused enormous vibrations in the sand-bentonite mixture. Every 6 cm has been stamped until full settlement has been achieved. This induced big forces on the sensors and possibly broke an FBG on the line. At the time being, this piece of bentonite is not considered to be an efficient protective bridge along an optical line and need to be adapted in the future to allow for safe splicing while sealing reliably the optical line. The remaining sensors survived and the long optical link could be pulled in the risers up to the location of the interrogating unit.

During the installations of the interrogation unit at the GTS in July, the patchcord of optical line 1 was found in a broken condition. This has probably occurred during the installation of the optical fibre into the riser. Since special tools were requested to solve this problem, line 1 could not be put in the measurement configuration network at that moment. This problem has been solved during a special visit to the GTS at the end of September.

Furthermore, it was also observed that the sensors MPWP-FOS and T-FOS-2 of line 3 are not detectable. This is probably due to a break of the fibre somewhere between the W-FOS-3 and T-FOS-2 sensor. Both sensors were however working correctly after the installation. This is a similar observation as has been done for line 2. Line 3 possibly also has been broken due to the levelling of layer 13. The learned lesson is that very special precautions in terms of vibration protection have to be made to assure a successful installation of the fibre optical system in material that is still to be compacted after sensor installations.

The final sensor configuration is shown in Table 3.2. The different lines during installation are shown in Fig. 3.22 to Fig. 3.24.

Sensor	**Dynamic Range**	**Status**	**Line and Layer**
W-FOS 1 (SN01041101)	On/off	Working	Line 1 – Layer 12
W-FOS 2 (SN01041102)	On/off	Out*	Line 2 – Layer 12
MTP-FOS (SN01041104)	0-5 bar	Out	Line 2 – Layer 12
T-FOS 1 (SN01050201)	0-50 °C	Working	Line 3 – Layer 13
W-FOS 3 (SN01050203)	On/off	Working	Line 3 – Layer 13
T-FOS 2 (SN01050202)	0-50 °C	Out	Line 3 – Layer 13
MPWP-FOS (SN01041103)	0-5 bar	Out	Line 3 – Layer 13

*Only the strain- FBG can be detected

Table 3.2: Final sensor configuration and sensor status at GTS

Fig. 3.22: Sensing line 1

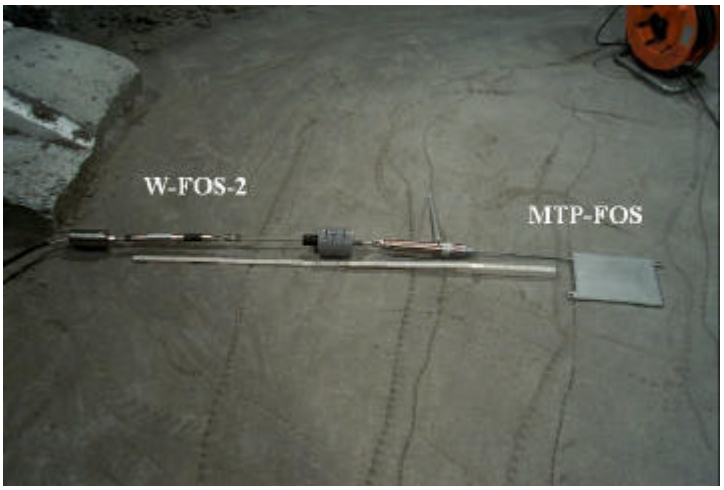

Fig. 3.23: Sensing line 2

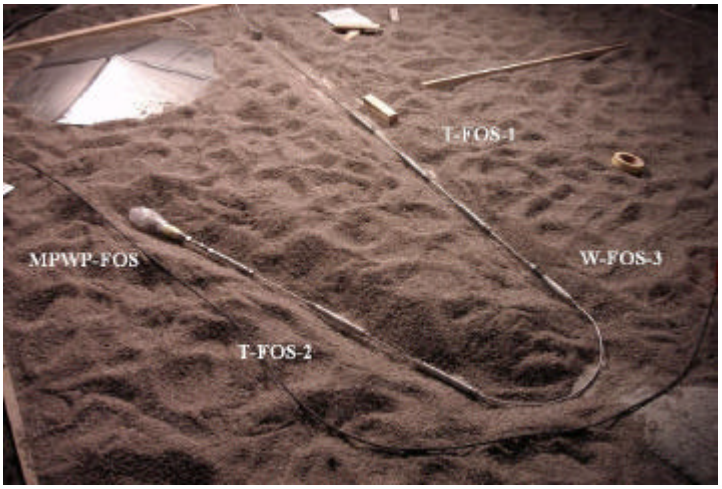

Fig. 3.24: Sensing line 3

3.2.4. Results

Fig. 3.25 shows the results of the humidity level of sensor W-FOS 1. The humidity level is defined as the wavelength difference between the strain-FBG and the Temperature FBG of the sensor, both expressed in nm. This difference will increase when the actual humidity increases above 80% humidity. As can be observed, compared to the humidity level at I.D. FOS Research lab, a very strong increase in signal has been observed just before and after installation. One of the reasons might be that the sensor responds at a humidity level starting from 80%. This limit has possibly be exceeded during the climatological conditions that the sensor encountered during transport. Furthermore, as can be observed, the sensor shows a continuous decrease during operation and the signal falls even below the initial value at I.D. FOS Research lab. This can be attributed to the hysteresis of the hydrogel film. At the last months an increase of the humidity level could be observed in two steps.

Line 2 does contain the water leakage sensor W-FOS-2 and the Total Pressure sensor MTP-FOS. However, as discussed before, a break of the fibre did occur within the sensor line. As a result, only one FBG (the strain-FBG) of the water leakage sensor W-FOS-2 can be measured. Unfortunately, this wavelength can not be used to measure the humidity because the fibre isn't stressed anymore due to the break. Nevertheless, we decided to keep

measuring this wavelength since it is important for the evaluation of the interrogation unit and optical switch system. The measurements are shown in Fig. 3.26.

Due to the break of the fibre in line 3, the temperature sensors T-FOS-2 and pore water pressure sensor MPWP-FOS are lost. As a consequence only the temperature sensor T-FOS-1 and water leakage sensor W-FOS-3 are visible. Fig. 3.27 shows the results of water leakage sensor W-FOS-3. The results of the temperature sensor T-FOS-2 are shown in Fig. 3.28. From last three figures, some peaks can be observed. These have been caused by some noise generation within the interrogation system.

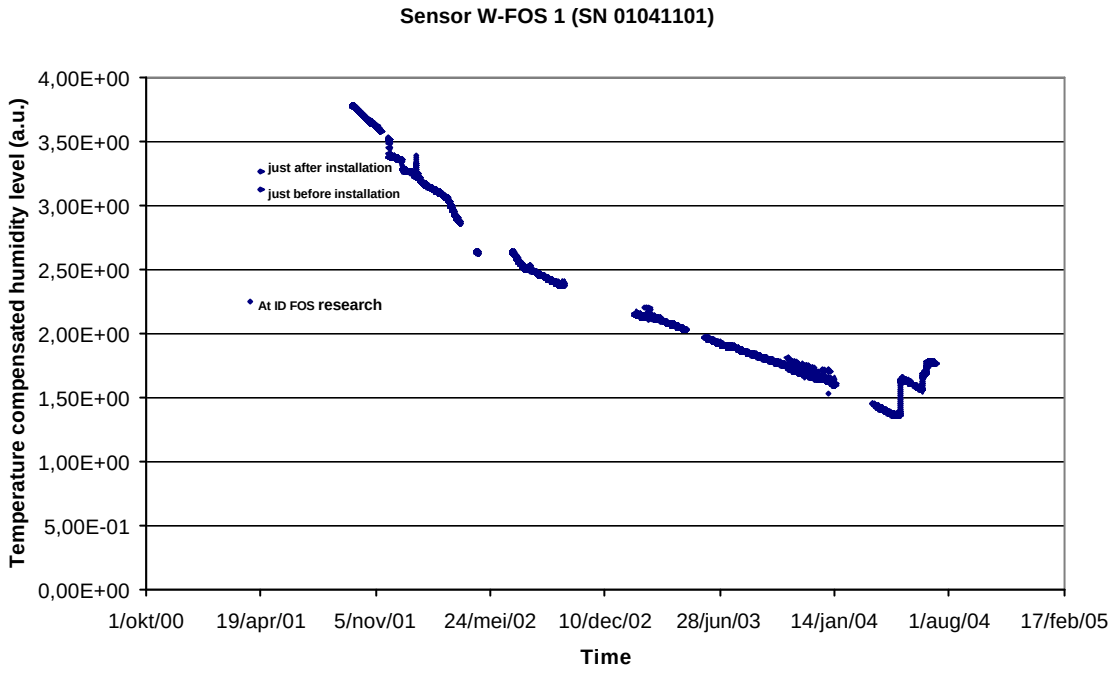

Fig. 3.25: Line 1: W-FOS 1 (SN01041101)

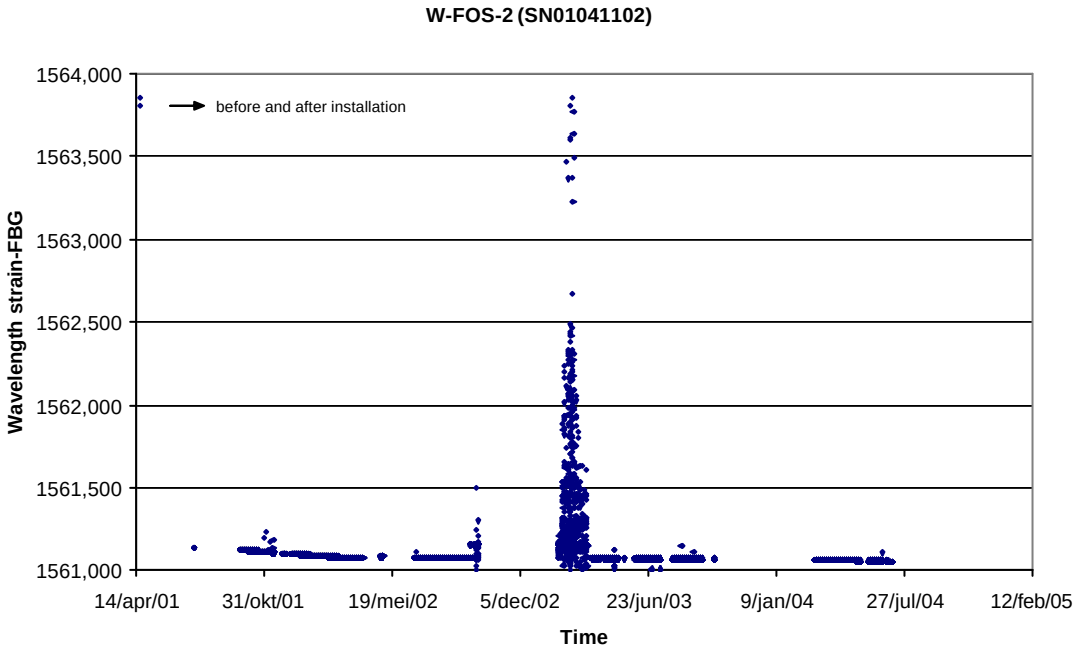

Fig. 3.26: Line 2: W-FOS-2 (SN01041102)

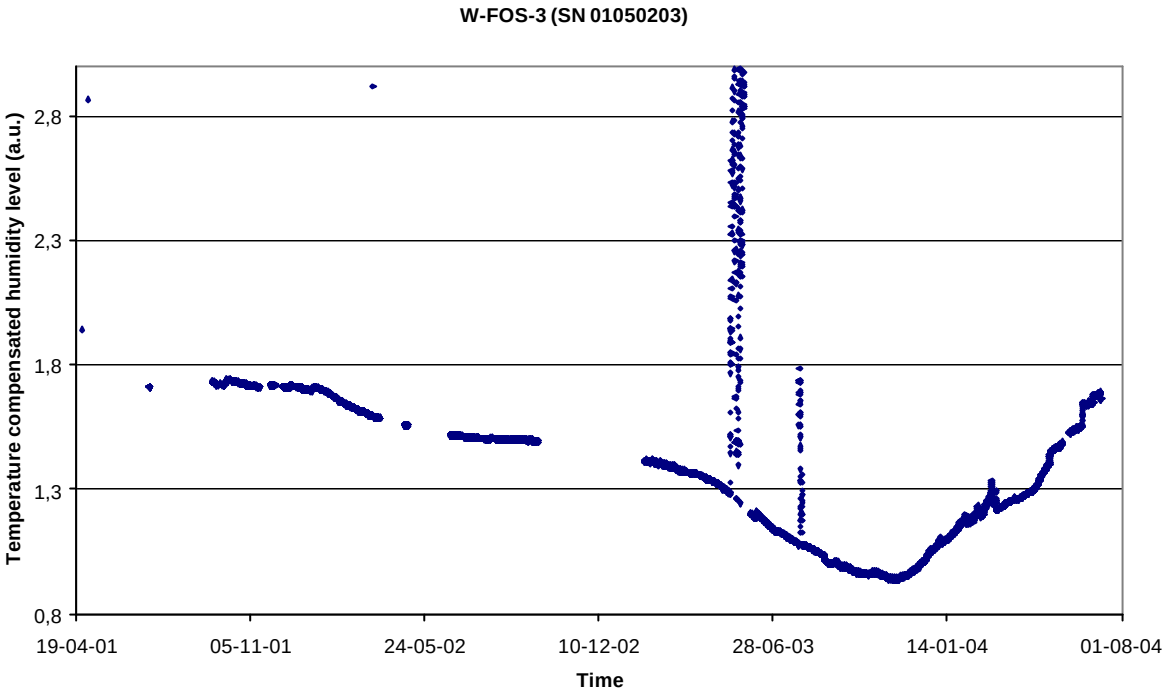

Fig. 3.27: Line 3: W-FOS- 3 (SN01050203)

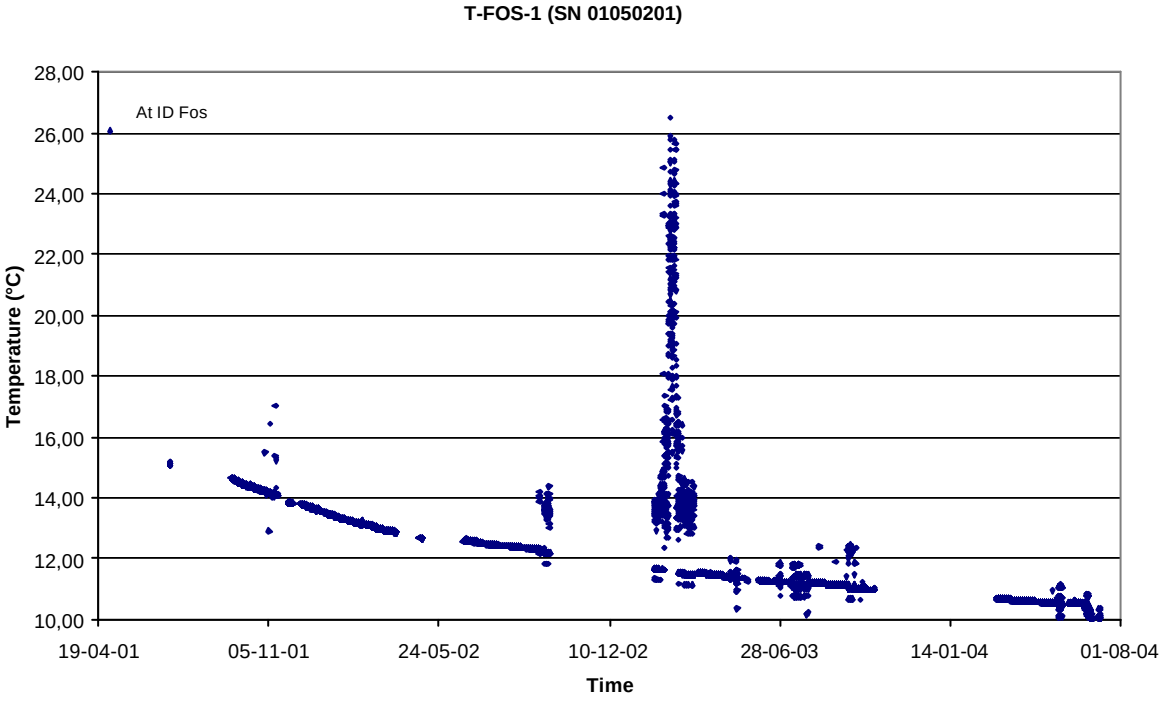

Fig. 3.28: Line 3: T-FOS-1 (SN01050201)

3.2.5. Dismantling results

During the de-installation at 8/7/2004 of the sensors, a few problems were encountered. A first problem occurred due to the kind of installation. All the optical fibres needed to be guided by a piping system (risers) to keep the complete niche locked from outside pressure. With the de-installation we weren't able to guide the fiber back from the measurement system to the sensor. This let's us no other choice then to cut the tubing and fiber. With sensor W-FOS 1 (see Fig. 3.29) we weren't able to cut far enough from the sensor to recover the sensor, so the fiber left in the sensor was too short to re-connectorise in the office and recalibrate.

Fig. 3.29 Riser and W-FOS1

Optical sensor line 2 is a series configuration of W-FOS 2 and MTP-FOS. W-FOS 2 has been damaged from the beginning due to heavy vibrations produced by the compaction of the bentonite layer. The strain-grating in W-FOS 2 was broken at the end of the grating as is shown Fig. 3.30. The temperature grating in W-FOS 2 has always been recorded. By the fact that the strain-grating in W-FOS 2 was damaged no data could be obtained during in-situ test. Recalibration of W-FOS 2 had no sense by the loss of the strain-grating which measures the water leakage.

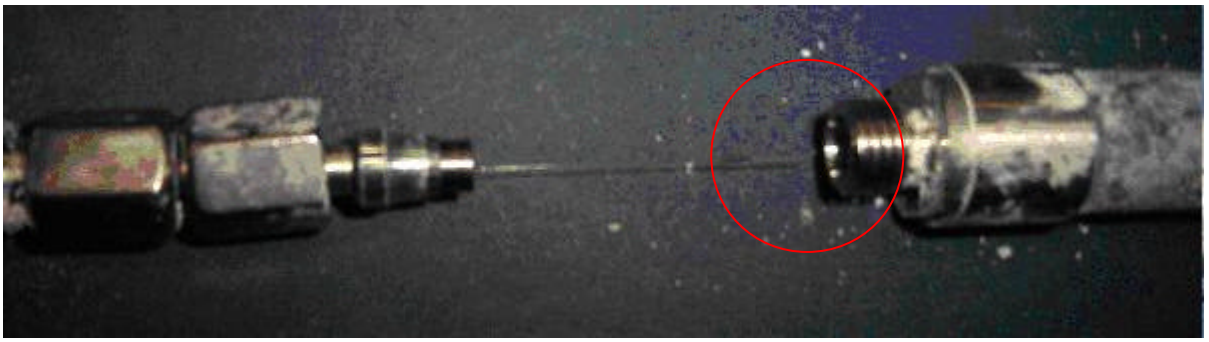

Fig. 3.30 W-FOS 2 Strain grating broken

As written before, the strain-grating in W-FOS 2 was broken after the drilling and by this MTP-FOS could not be measured. There is also the possibility that the bentonite bridge was damaged before. This can be concluded since during the de-installation of the optical line, the bentonite bridge was observed to be loose. This bentonite brigde is filled with glue and the fiber was broken at the glued swagelock coupling. In Fig. 3.31 the broken fibre in the bentonite bridge is shown. While dismantling MTP-FOS there was still oil in the pressure plate and the plate did not show any leakage. It could be observed that the two FBGs inside are still intact.

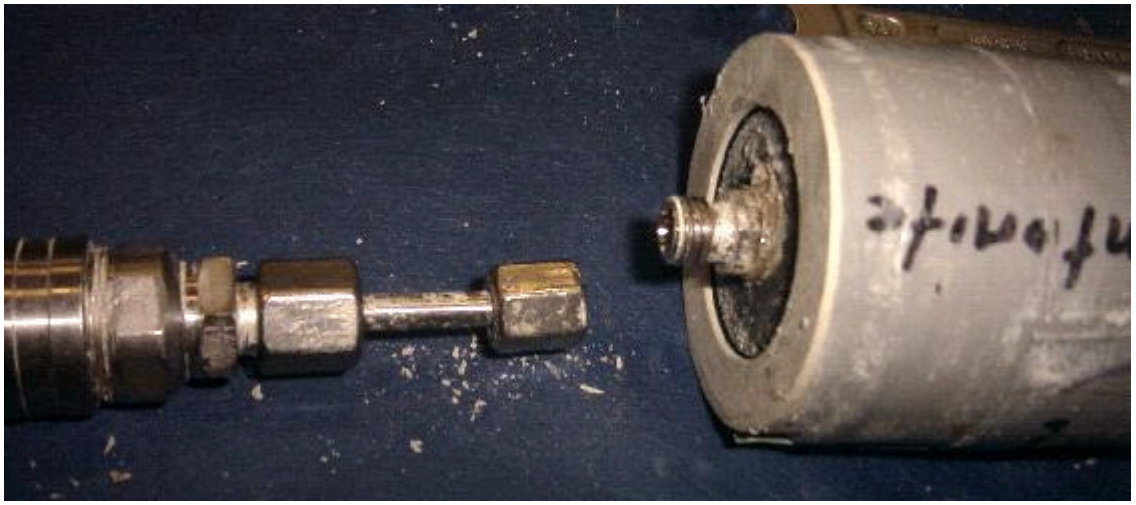

Fig. 3.31 Broken fibre in bentonite bridge connected to MTP FOS

Optical sensor line 3 also faced some problems. First of all some water leakage from the sensors to the optical switch has been observed. The water leakage was created by a not perfectly closed riser, this made it possible that water was transported through the aramide fibers in the cable to the optical switch were we can see water intrusion on Fig. 3.32 . This also had some effects on the measurement data from that line, that explains some data loss due to higher losses then expected with water intrusion and de-generation of both connectors and adaptors.

Fig. 3.32 Optical switch water intrusion

Furthermore, it could be observed that the parameter grating in the W-FOS 3 sensor was broken (see Fig. 3.33).This most probably has also been caused by the strong vibrations during the compaction of the bentonite. The optical line 3 was a series configuration of sensors. This means, as can be seen in the measurements, that all the sensors behind W-FOS 3 could not be measured during the in-situ test.

Fig. 3.33 W-FOS 3 with broken Parameter grating

These are T-FOS 2 and MPWP-FOS. MPWP-FOS was unable to be repaired by the fact that all swagelock coupling were filled with glue to have a perfect fitting. This handling made it impossible to dismantle the sensors at ID FOS lab while keeping them intact. The MPWP-FOS was destroyed during vibrations produced by the compaction of the bentonite layers. As can be seen on Fig. 3.34, the temperature grating is broken. No re-calibration could therefore be obtained from MPWP-FOS. The strain grating is still intact. As can also be clearly seen, MPWP-FOS was soaked by water (picture taken 1 week after de-installation).

Fig. 3.34 MPWP FOS broken at temperature grating

Further on line 3 both T-FOS1 and T-FOS 2 are intact and were recalibrated at the ID FOS labs. The results are shown in following graphs Fig. 3.35 and Fig. 3.36. As clearly seen the sensitivity coefficients are almost the same before and after. On the other hand, the offset is different due to measurement calibration topics, this means that both equipment from calibration and recalibration were different. As we can clearly see the difference on both temperature sensors, this can exclude other problems.

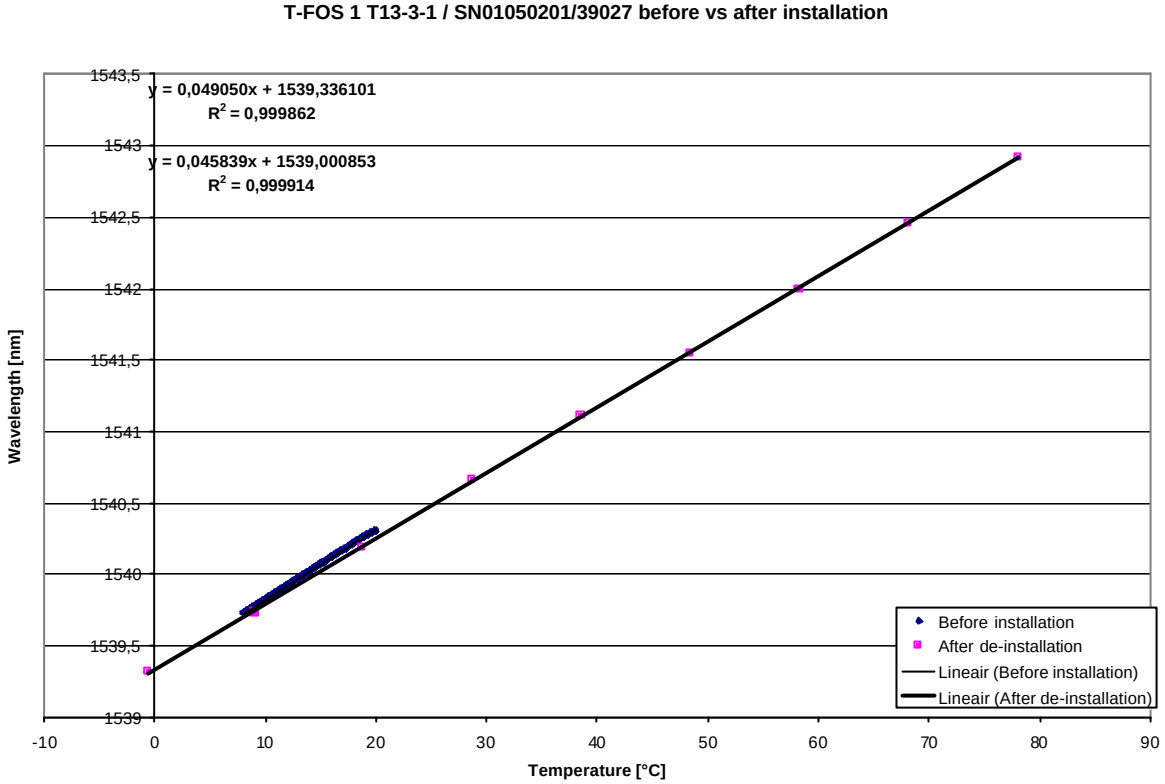

Fig. 3.35 T-FOS 1 Calibration vs Recalibration

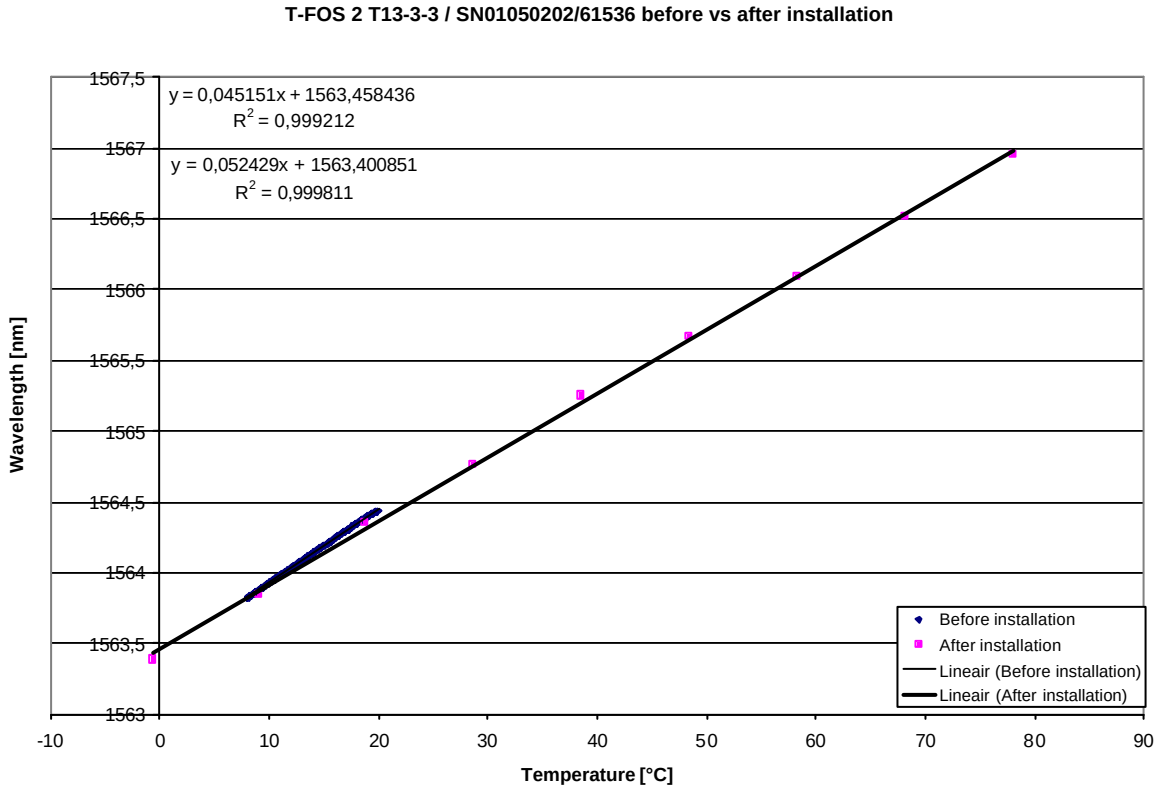

Fig. 3.36 T-FOS 2 Calibration vs Recalibration

3.3. Morsleben repository

The first installation at the Morsleben repository took place at 5 and 6 December 2001. Three fissurometers (mountable strain sensors) and 2 hydrogel sensors were installed together with the interrogation system. During the visit from 9 up to 11 April, the strain cable has been installed. In the following paragraphs, the characteristics of the different sensors and interrogation system will be described and an overview of the measurement results is given.

3.3.1. Sensors

In total, 9 sensors have been installed. Three fissurometers, two hydrogen leakage sensors and 1 strain cable containing four measurement intervals. The sensors are installed at two different levels. Fig. 3.37 shows the position of the different sensors and the measurement unit. An overview of the different sensors and the corresponding series numbers and used optical lines is shown in Table 3.3.

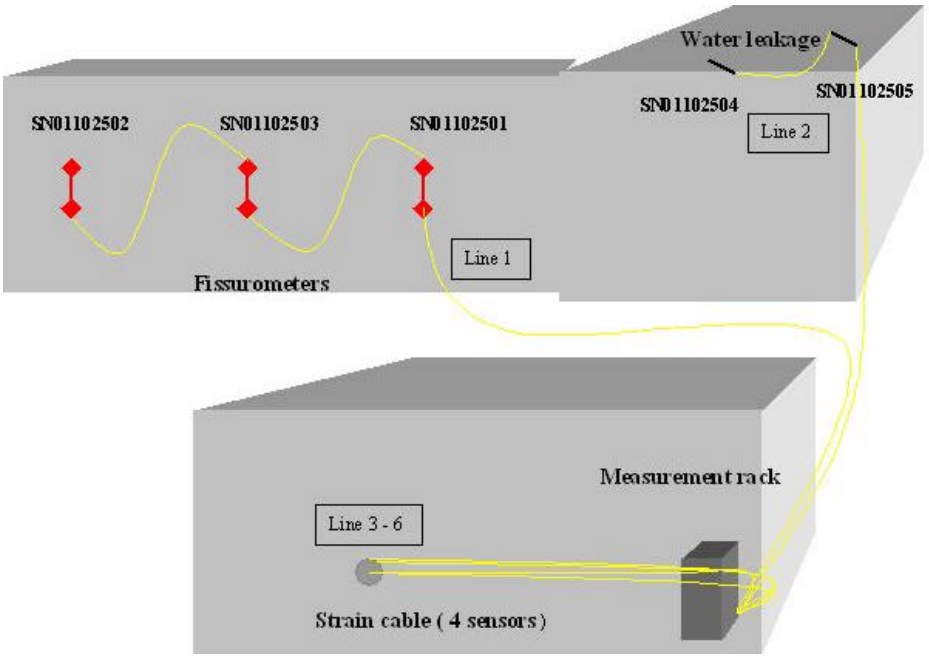

Fig. 3.37: Position of the different sensors at the Morsleben site.

Sensor type	*Sensor description*	*Optical line*	*Serie number*
MS-FOS 1	***Fissurometer 1***	Line 1	SN01102501
MS-FOS 2	***Fissurometer 2***	Line 1	SN01102502
MS-FOS 3	***Fissurometer 3***	Line 1	SN01102503
W-FOS 1	***Water leakage sensor 1***	Line 2	SN01102504
W-FOS 2	***Water leakage sensor 2***	Line 2	SN01102505
D-SC-FOS-1	***Strain sensor 1***	Line 4	SN02032801
D-SC-FOS-2	***Strain sensor 2***	Line 5	SN02032802
D-SC-FOS-3	***Strain sensor 3***	Line 3	SN02032803
D-SC-FOS-4	***Strain sensor 4***	Line 6	SN02032804

Table 3.3: Overview of the different sensors at the Morsleben site

The design of the fissurometers has been described in paragraph 1.2. Three of these fissurometers have been produced: SN01102501, SN01102502 and SN01102503. All fissurometers are foreseen of two Diamond E2000 connectors at each side to make a connection to the following sensor or interrogation unit. These connectors do have the

advantage that they are much more resistant against dust. Fig. 3.38 shows the calibration result of sensor MS-FOS 1 (SN01102501). A very good linear relation has been obtained. The same has also be observed for the other fissurometers.

The installation of these sensors took place at 5 and 6 December 2001. All three sensors are put against the same wall (left SN01102502, centre SN01102503, right SN01102501) and are in series connected to the interrogation unit using optical line 1. In Fig. 3.39, a photo is shown of sensor SN01102502 after installation. It can be observed that the conventional fissurometer (left sensor) is close positioned to the optical fibre sensor. This is the same for all other fissurometers what makes a comparison possible.

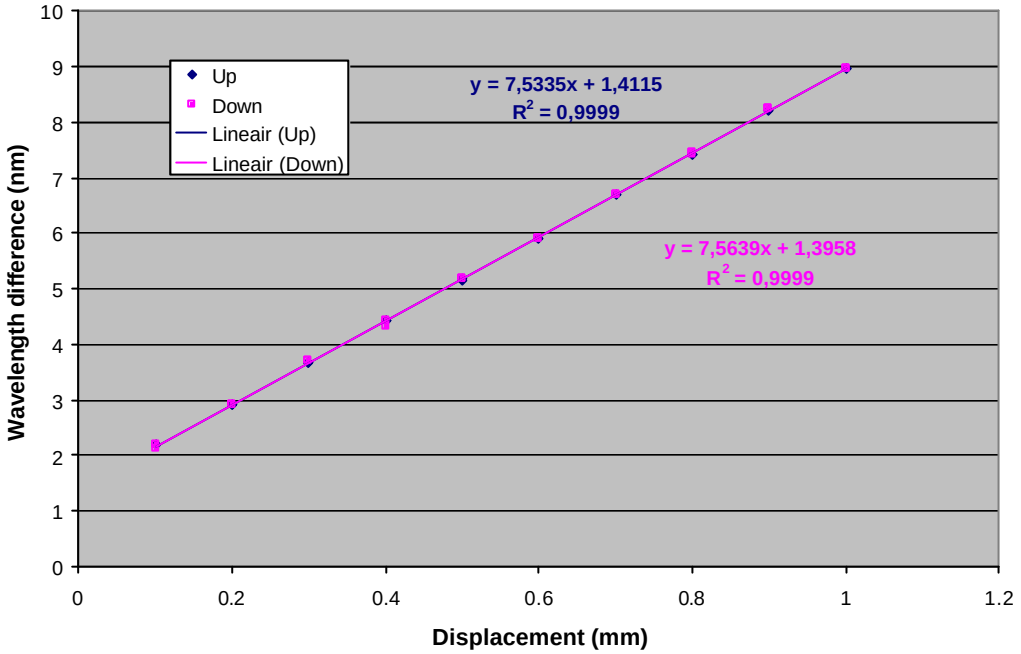

Fig. 3.38: Calibration result MS-FOS 1 (SN01102501)

Fig. 3.39: Fissurometer SN01102502

The water leakage sensors have been installed at the same level as the fissurometers. Before installation it was tested if the water leakage sensors do react on the salt solution, see 2.9. As could be observed, a good response did occur. Nevertheless, the sensor did show an hysteresis for the salt solution. After drying the sensor, the wavelength was even increased. This can possibly be attributed to the crystallisation of the salt in the hydrogel films. The water leakage sensor is as a consequence only a 1 way sensor in this environment.

The water leakage sensors installed in the mine have 3 hydrogel films and were positioned against the sealing, see Fig. 6-40. The sensors are used to measure the infiltration of water droplets in the gallery. It has to be noticed that the design of the installed sensors had to be adapted for measurements of droplet infiltration. The sensor should be extended by a kind of collector around the sensitive part. This has been done by DBE TECHNOLOGY after the installation for SN01102504, see Fig. 3.41.

Fig. 3.40: Installed water leakage sensor SN01102504

Fig. 3.41: Water leakage sensor SN01102505 equipped with droplet collector

The strain cable has been installed during the visit of 9 to 11 April. A detailed description of the sensors and the fixation mechanism can be found in paragraph 1.3. A typical calibration

result, of sensor SN02032801, is shown in Fig. 3.42. For all sensors, a very good linear relation is obtained with no significant hysteresis effect.

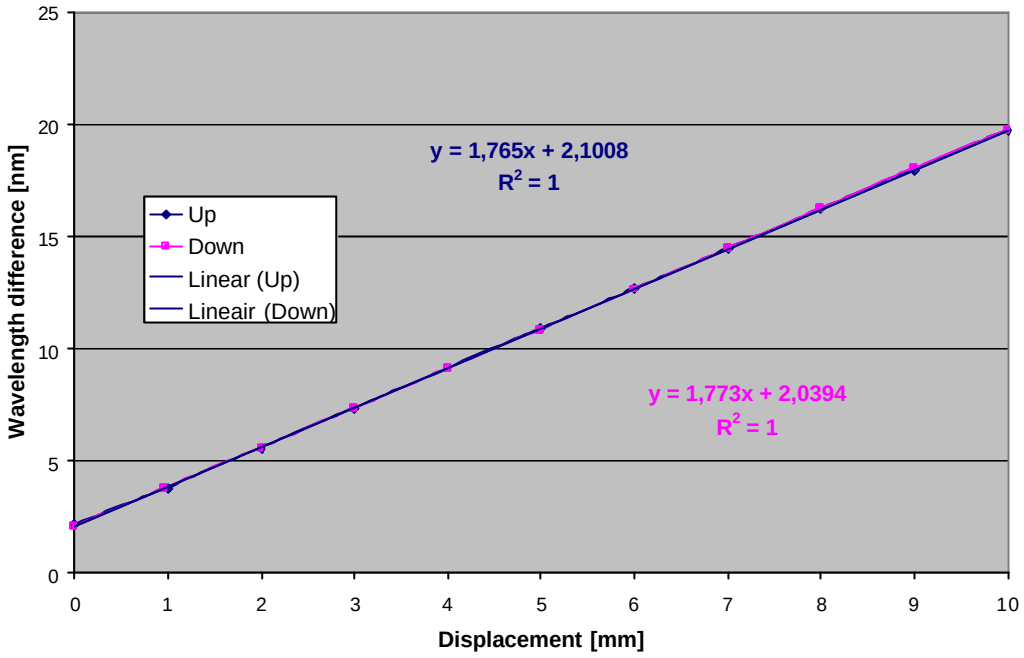

Fig. 3.42: Calibration results sensor SN02032801

The dimension of one segment of the installed strain cable is shown in Fig. 3.43. As can be seen, each segment has a total length of 6.98 m and contains two dummy packers. Four such segments are put in series (mechanical). Notice that the sensors are not put in series on one optical line. Four lines are used: line 3 up to line 4. The different sensor positions are shown in Table 3.4.

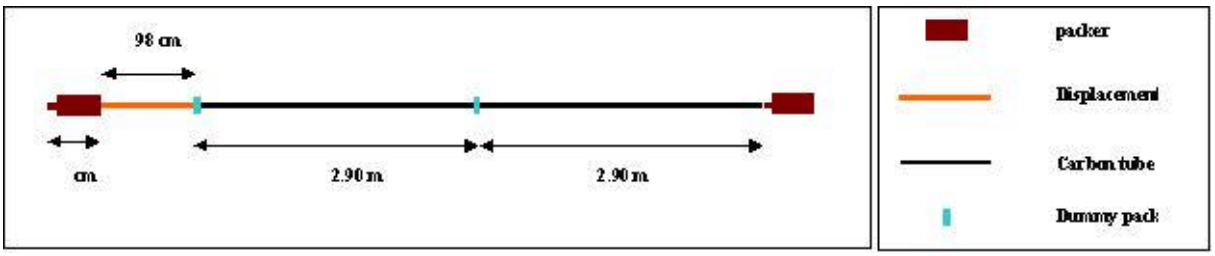

Fig. 3.43: Strain cable dimensions

Sensor	Position [m]
SN02032804	0.47
SN02032802	7.45
SN02032801	14.43
SN02032803	21.41

Table 3.4: Sensor positions in borehole relative to the gallery.

Fig. 3.44 shows some photo's of the installation. It has to be noticed that the borehole was not completely horizontally drilled. This induced some problems due to the fact that no long segments could be inserted. Finally, Fig. 3.45 shows the borehole after installation.

Fig. 3.44: Installation of strain cable

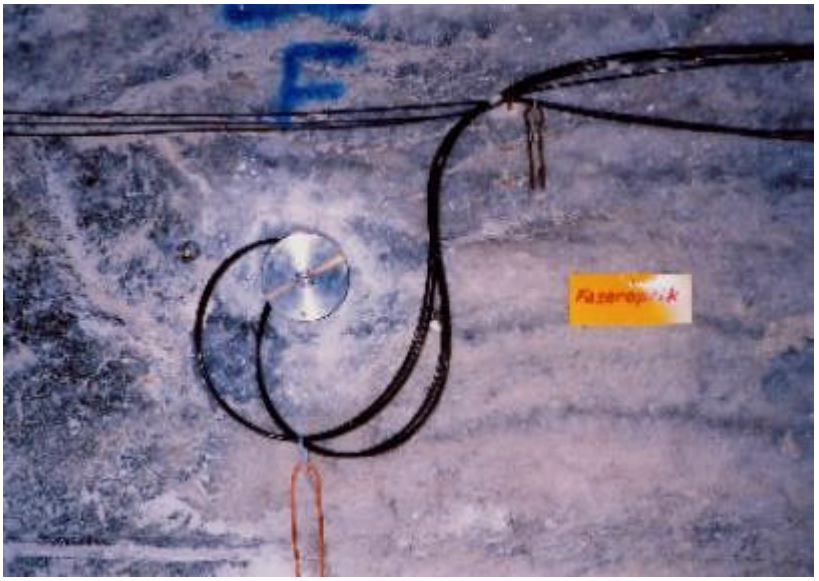

Fig. 3.45: Front plate strain cable

3.3.2. Interrogation system

The interrogation system installed at the Morsleben repository is shown in Fig. 3.46. It consists of a FBG-IS system of Micronoptics equipped with an external source input, a 1X8 optical switch of Polytec, an Uninterruptible Power Supply (UPS) and an industrial P.C. (Pentium III, Advantech). The system is software controlled using Labview. The complete system is integrated into a rack in order to protect the system from dust infiltration.

The PC can remotely be controlled using the modem connection and the installed PC Anywhere software (version 10.5). This makes it possible to update the software from off-site, restart the program and download the measurements.

The Labview measurement program is similar to the one used at the GTS. Only the control of the optical switch was changed due to the different type.

On the 26th of January the PC stopped measuring and collecting measurements. After a few interventions of Morsleben-personnel and dial-in problem solving, an intervention was needed. An intervention on the 1st of April taught us that the FBG-IS (Fibre Bragg Grating – Interrogation System) and harddisk of the Industrial PC was unrepairable damaged, due to a power failure. The FBG-IS was removed and replaced by a SpectralEye interrogator.

Fig. 3.46: Interrogation system

3.3.3. Results

Fig. 3.47 shows the results of the three fissurometers.

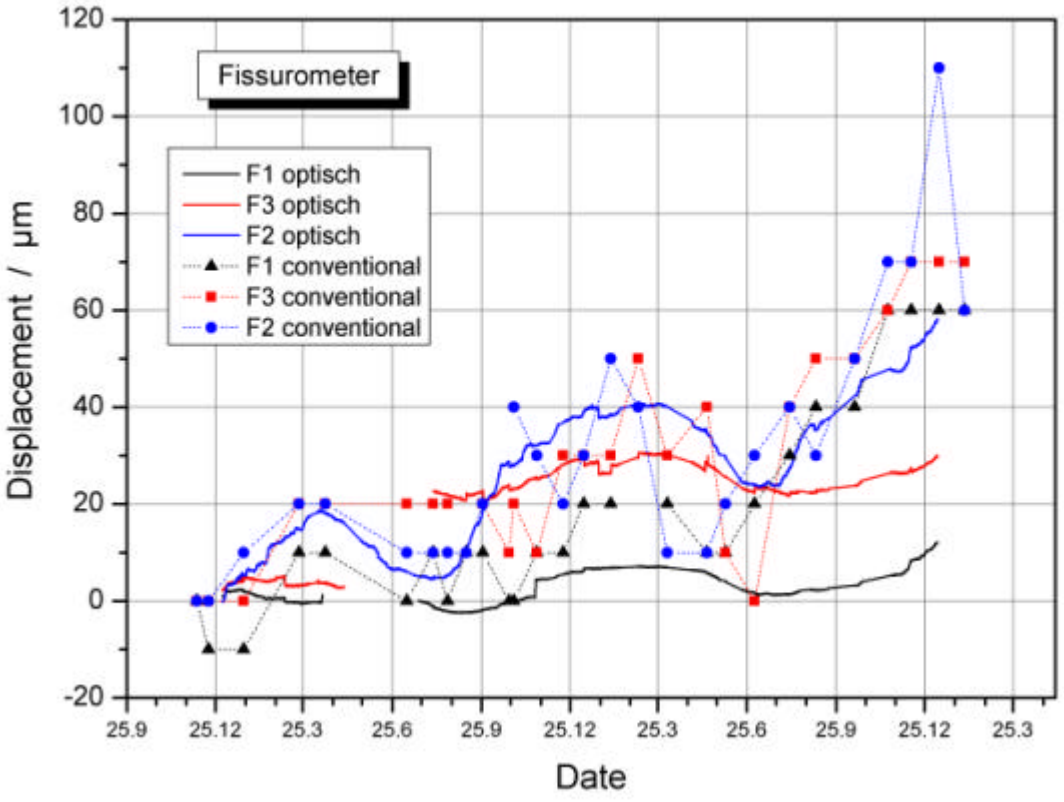

Fig. 3.47: Measurement results of fiber optic and conventional fissurometers at the Morsleben site

All sensors are indicating some variations in fissure opening. The resolution of the conventional fissurometers is ± 10 µm and for the optical system ± 0.1 µm which is about three orders of magnitude higher. Considering the different resolution abilities a good correspondence can be stated. The measurement trends are characterized by both types of sensors in a similar way except for the end of the measurement period where the optical system indicates a smaller displacement as the conventional system. It is assumed that this is due to the fact that the compared fissurometers are not located exactly at the same position. Discontinuities of fissure openings are assumed to the reason for small differences in fissure movement. Due to a failure of the interrogation system, some data loss occurred during the measurement period.

The temperature results, calculated using the temperature gratings, are shown in Fig. 3.48.

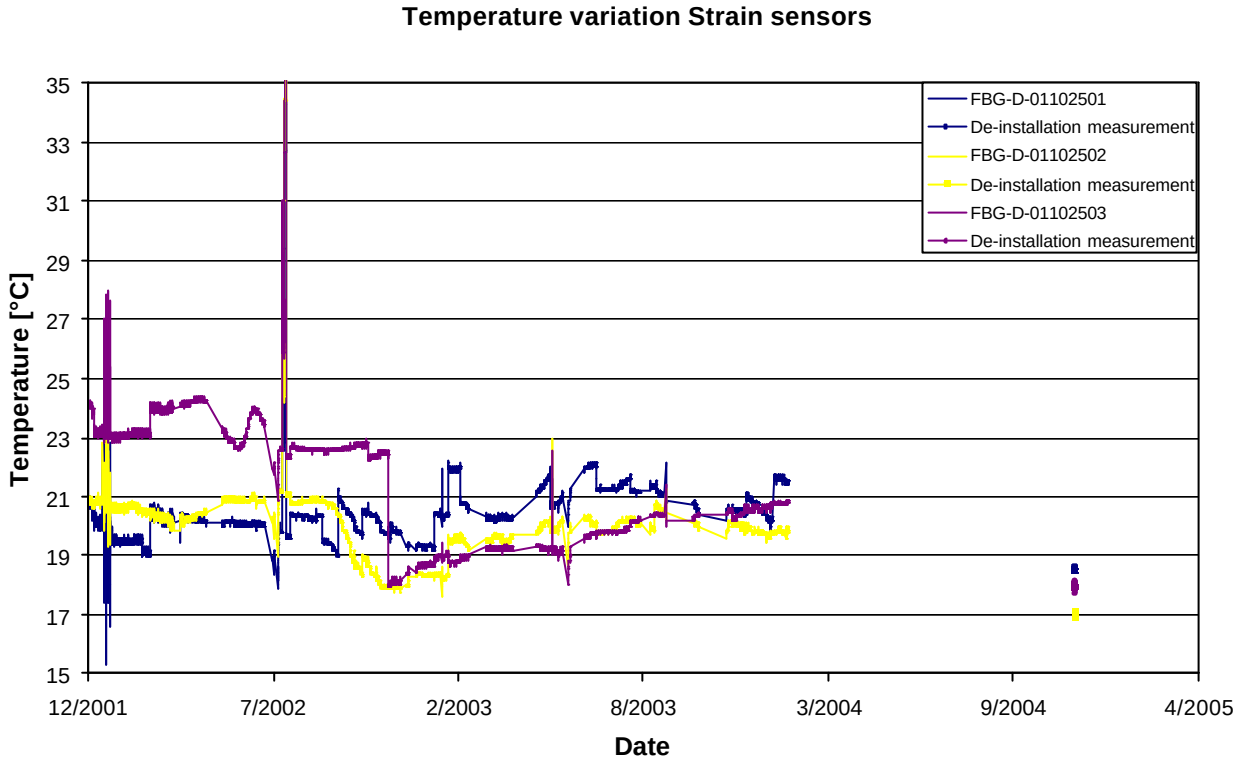

Fig. 3.48: Temperature measured by Fissurometers of line 1.

The temperature measured at the location of sensor SN01102503 did also show the largest fluctuations: between 18 and 24°C, while for sensor SN01102501 and SN01102502 the temperature fluctuated between 18 and 22°C. It needs however to be noticed that the temperature read-out shows some abrupt changes. This can for instance be seen on 19/11/2002 where the temperature decreases with 3.5°C. These changes are most probably caused by the series configuration of the sensors. Due to this configuration, the FBG used for the temperature configuration might become strained when the series connection cable is moved. Based on this observation, the design of the sensor has been adapted. In the new design, the temperature FBG is isolated from any strain influence by fixing the FBG inside a stainless steel capillary.

Fig. 3.49 shows results of the water leakage sensor. In this test the sensor has been installed at the roof of an underground opening to monitor fluid inflow or “dropping rates” respectively at selective locations. As can be seen, the brine inflow is not constant but varies periodically. Looking at the time scale this can be attributed to seasonal fluctuations over periods of 1 year. In addition, the measurement results of the temperature FBG at the sensor is plotted in

figure 3.49 to check for any temperature dependence. A more or less constant temperature has been observed and compensated. Thus, the fluctuation can be stated to be just humidity dependent.

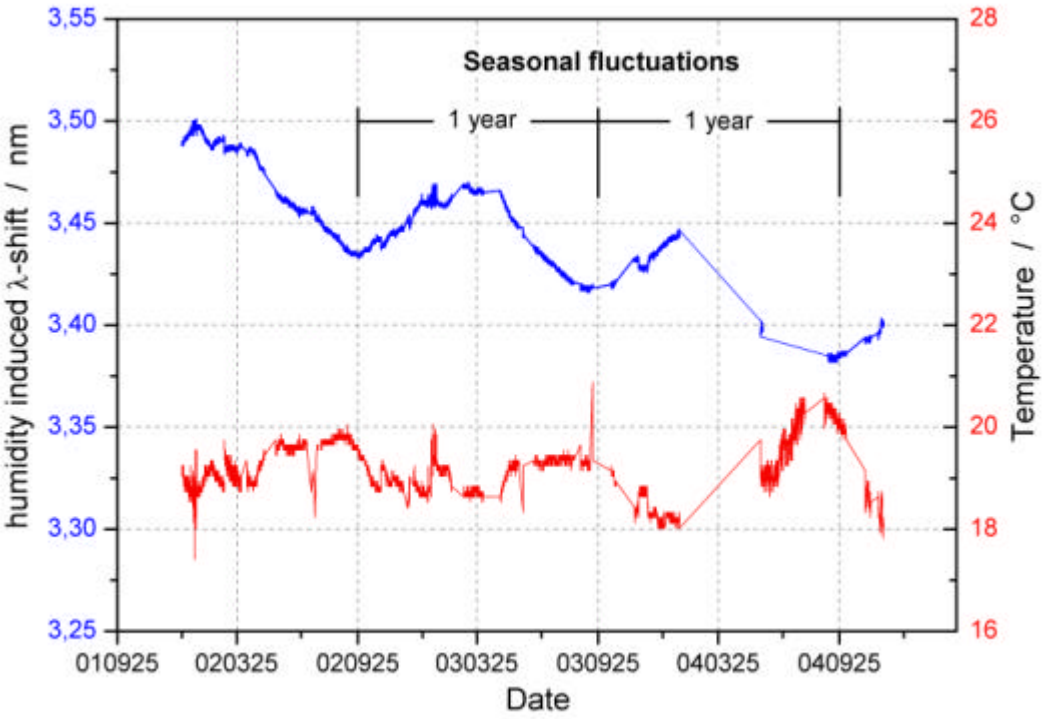

Fig. 3.49: Water leakage sensor results

Finally Fig. 3.50 shows the results of the strain cable. Sensor SN02032803 has not been recorded anymore since 20 November 2003. This is due to a too low signal, most probably caused by a damaged connector. All sensors do show first some very small decreases in distance between the different packers (< 50µm) after which the sensors seem to stabilise. However, at the end of 2003 and beginning of 2004 a strong increase in this distance occurs.

In addition, sliding micrometer measurements from an adjacent borehole are plotted into the upper graph. These measurements have been recalculated to obtain comparable interval displacements. A comparison yielded diverse results. The displacements obtained from interval 2 fit well with the sliding micrometer measurements from the second borehole. The increase of the relative displacements of interval 1 during the phase of temperature increase is significantly higher than the sliding micrometer measurements. In interval 3 no significant reaction has been recorded. The latter can be attributed to the spring mechanism. The higher deformation during the phase of temperature increase was assumed to be due to the uncompensated thermal expansion of the carbon cable that was expected to be small enough.

Lessons learned: The spring mechanism has to be improved especially for serial configuration of interval connections. The temperature effect on the carbon extension cable has to be compensated for. These “learned lessons” have been used to improve the new extensometer configurations recently applied at the Mont Terri and Bure URL in Switzerland and France in the framework of another research project. Within these configurations damping effects are excluded and additional FBGs for temperature measurements have been implemented in each individual carbon cable to compensate for temperature effects [15].

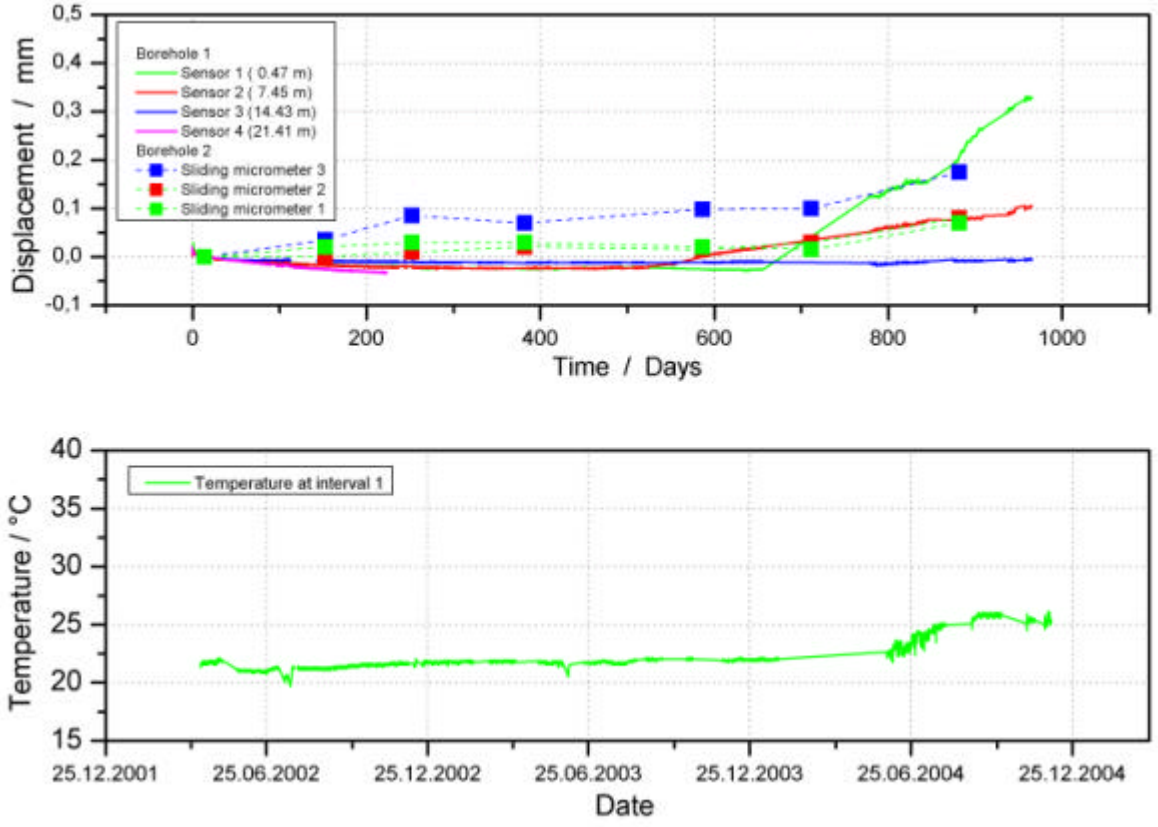

Fig. 3.50: Morsleben line 3-6: Strain cable

Finally, it needs to be mentioned that several points are missing. The system has stopped measuring 6 times in total from:

- 31/3/2002-09/4/2002 software bug
- 6/5/2002-23/5/2002 Installation modem - error
- 9/7/2002-16/7/2002 problem not identified
- 3/12/2002-9/12/2002 possibly caused by stopping modem connection
- 12/12/2002-19/12/2002 problem not identified
- 26/01/2004-31-5-2004 problems occurred at FBG-IS due to power failure

3.3.4. Dismantling results

The system has been dismantled at the first of December 2004. The interrogation system as well as the fissurometers and the water leakage sensor have been removed. The strain cable is still present since this is fixed inside the borehole and cannot be dismantled. After the dismantling, the sensors have been analysed at the laboratories of I.D. FOS Research.

Fig. 3.51 shows the recalibration of the fissurometer SN01102503 compared with the calibration curve before installation. As can be observed a good linear correlation still exists. Furthermore, the sensitivity coefficients are very much the same: 7.6147 and 7.5894. The offset however cannot be compared, this is due to the fact that the calibration measurement is a relative measurement method. However, a change in offset only would be expected if the fibre fixation is not working well resulting in a longer free fibre inside the sensor. If this would have been happened, this also would change the sensitivity coefficient which is not the case. It therefore can be assumed that no significant offset change has been taken place. For the other two fissurometers, similar results have been obtained. It therefore can be concluded that no remarkable ageing effect has been taken place for these sensors.

In a second phase, the water leakage sensors have been analysed. The broken sensor SN01102504 has been dismantled. It could be observed that the parameter grating was broken behind the hydrogel fixation. As discussed before, the reason for this break is the high response this sensor has experienced during the in-situ test. Fig. 3.52 shows a photo of the inner components of this sensor. As can be seen that the parameter grating is broken from the temperature grating, this is due to the high stress during and in-situ test.

Water leakage sensor SN01102505 was not damaged. The response of this sensor has been analysed by submerging the sensor into water. Fig. 3.53 shows the hydrogel response. As can be seen, the hydrogel still reacts quite well.

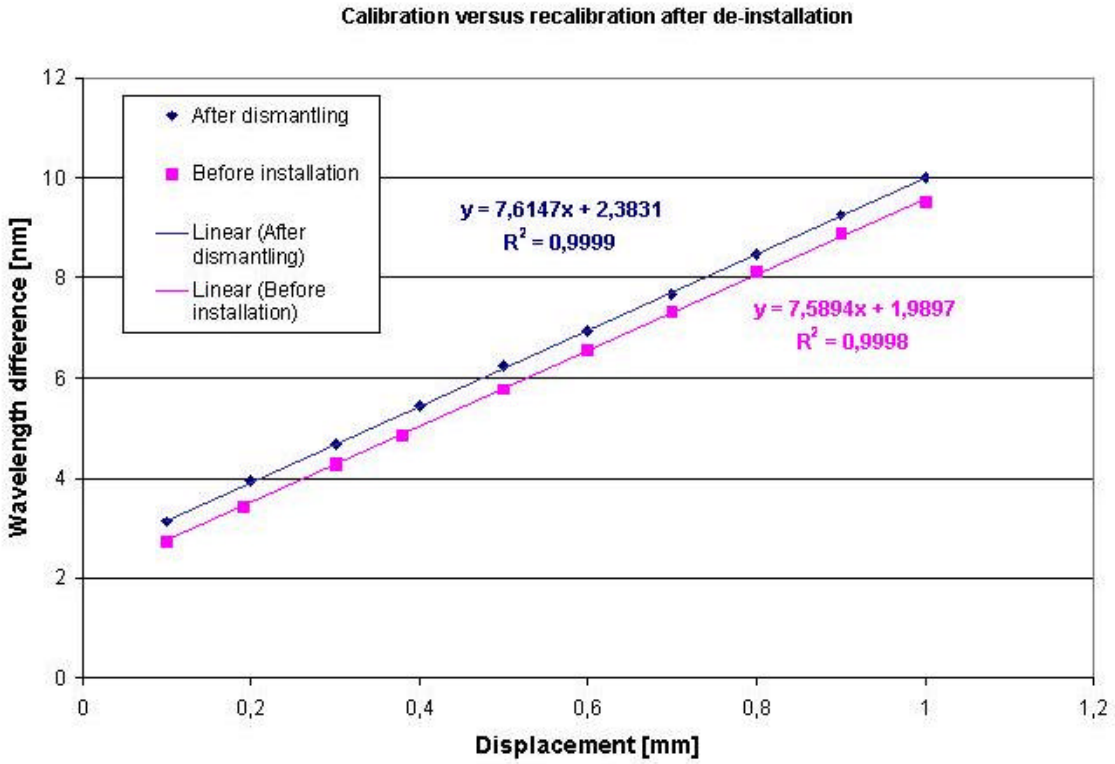

Fig. 3.51: Calibration before installation versus calibration after de-installation for sensor SN01102503

Fig. 3.52 : Photo of inner components of the damaged water leakage sensor SN01102504.

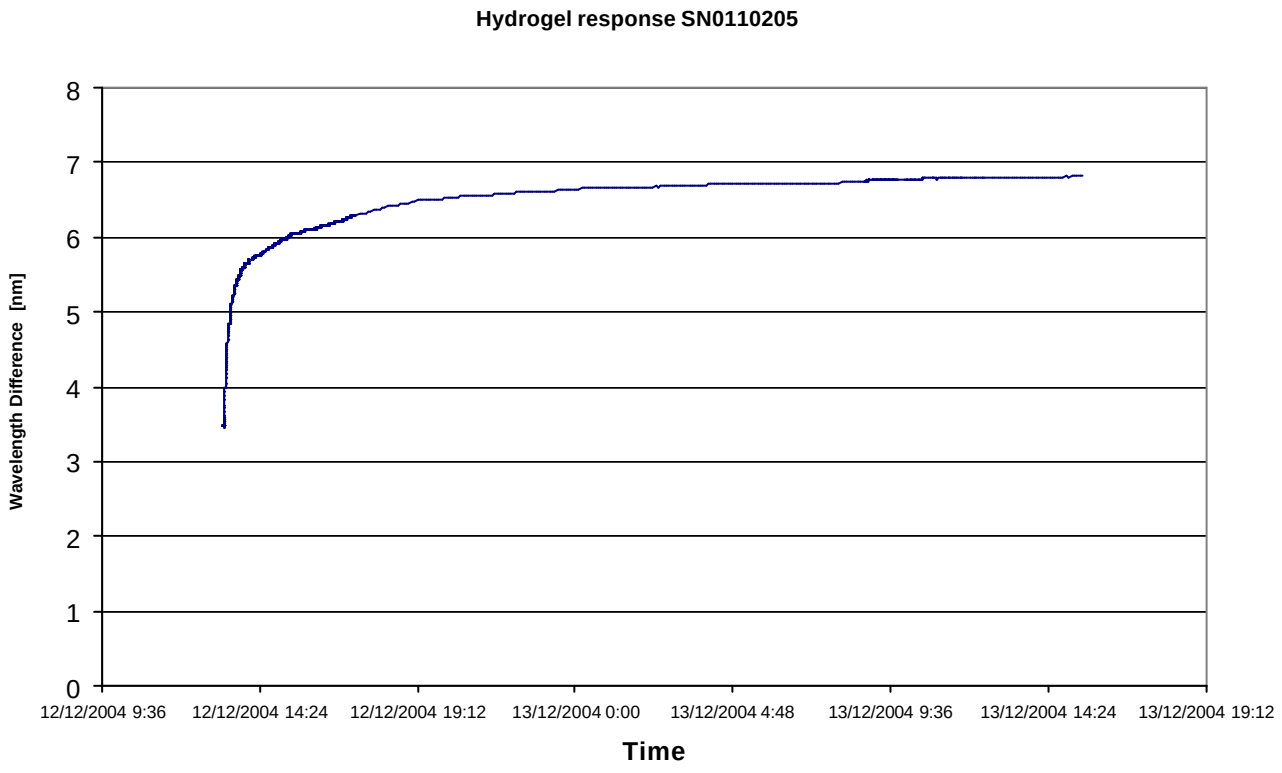

Fig. 3.53 Hydrogel response after de-installation

3.4. Königstein

After having achieved successful laboratory results the new probe has been tested in-situ at the Königstein mine for monitoring purposes. In what follows, a brief overview of the most important results will be given.

3.4.1. Installation of the optical pH system at the Königstein mine on 16/10/2001

The optical pH probe was protected against dirt and has been installed in a drain channel (see Fig. 3.54). The dimensions of this channel are shown in Fig. 3.55.

Fig. 3.54: Installed pH-head probe with filter to protect the reflectors against dirt in the drain water

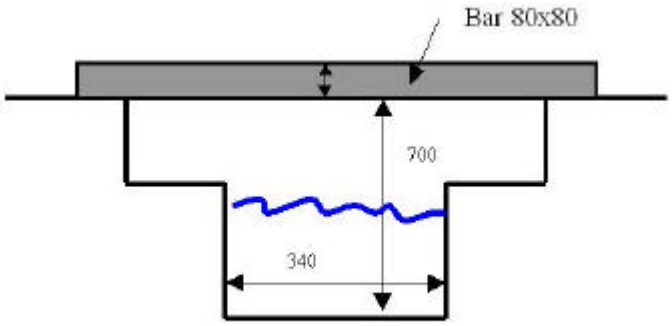

Fig. 3.55: Dimensions of drain channel

The metal bar across the channel has been welded to a metal rod in such a way that the pH-head probe could be fixed by a PVC tube into the drain water. The industrial rack containing the pH-unit and the laptop has been mounted at the mine wall and is shown in Fig. 3.56.

Fig. 3.56: Complete system installed in an industrial rack against the mine wall.

Software has been initialised with the latest calibration constants measured in the laboratory. Table 3.5 shows the calibration data and the corresponding calculated constants of the fitted

sigmoid function. Using these calibration coefficients, the pH-meter has been measuring a pH value of 3.4 but it stabilised around pH 2. This stabilisation is probably a temperature effect. The water temperature was 16°C. In the neighbourhood of the optical pH sensor, a conventional pH-meter had been installed to have a reference pH-value of the drain water. This conventional meter was measuring a pH-value of 2.53.

pH level	Signal
2,05	3994
3.18	3975
6	3945
7.74	3936

Parameter	Value
A	221,73
B	-2.6
X0	-0.06
Y0	3925

Table 3.5: Calibration data measured in Lab 16/10/2001 and corresponding constants.

3.4.2. Measurement results

Figure 3.57 shows main results of the test. It has been observed that there is a maximum period of about 2 weeks in which stable results could be obtained. During this period the measured values are very much the same as those taken with the hand held pH-meter. Any longer continuous running of the probe yield a drift of the measurement results.

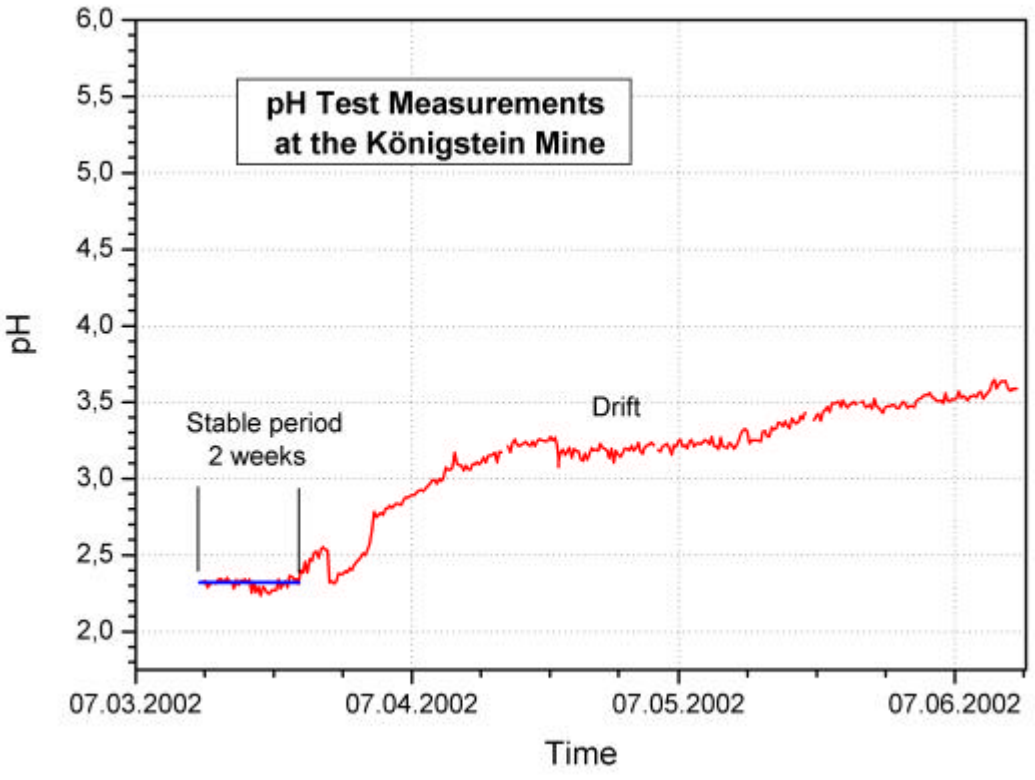

Fig. 3.57: pH measurement results

At the time being two main reasons can be given for the drift.

1. First of all, the drift can be caused by a kind of photo-bleaching effect of the reflector's dye (photo-decomposition). The old reflector was taken back to the laboratory for

investigation. Fig. 3.58 to Fig. 3.60 show some photo's at different locations of the old reflector. These can be compared to the new reflector shown in Fig. 3.61 and Fig. 3.62. The quality of the photos is not very good, since it is difficult to focus correctly the rough surface. As can be observed, the cpg's of the used reflector are still distinctive from each other what means that the reflector is not dirty or damaged. As a consequence, the used filter has been working good. Furthermore, it could visually be observed (not on photo's since these are black and white) that the colour of the used reflector is more faded what testifies a partial bleaching of the dye. This degeneration can possibly be reduced by decreasing the light radiation frequency. In order to verify this hypothesis, three different time intervals had been set. As can be seen some drift still is present after the second calibration (sampling interval is set to 4 times a day). This indicates that possibly also an other effect is causing a drift.

2. The second possible reason for the drift is the degeneration of the LED. The modulation of the wavelength is carried out by driving the LED in two different states with two different currents. By changing the driving current the emission of the LED changes: the change is roughly 10 nm. By measuring the amplitude change, the slope is measured. However, for a reliable result it is important that the relative change in emission power as well as the wavelength change of 10 nm is constant as function of time. If not, a drift is expected. As soon the equipment will be returned, the performance of the LED will be analysed in order to verify this hypothesis.

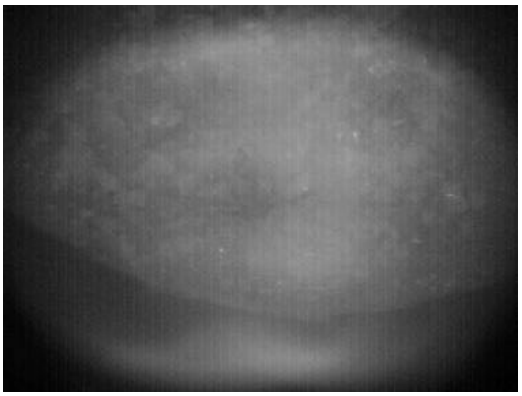

Fig. 3.58: edge of the old reflector.

Fig. 3.59: edge of the old reflector(higher zoom)

Fig. 3.60: central zone old reflector

Fig. 3.61: edge of the new reflector (smaller zoom)

Fig. 3.62: central zone of the new reflector (higher zoom)

3.4.3. Influence of temperature

The opto-electronic unit has been equipped with a thermoelectric cooler/heater (TEC) to keep the sensitive electronic parts on a constant temperature, during the year the temperature has been set to different temperatures during the calibration. If the set temperature is closer to the ambient temperature it's easier to keep the electronics temperature stabilised.

To clarify the temperature influence the measurements of the first period are used. Fig. 3.63 shows the results obtained in the mine from October to January.

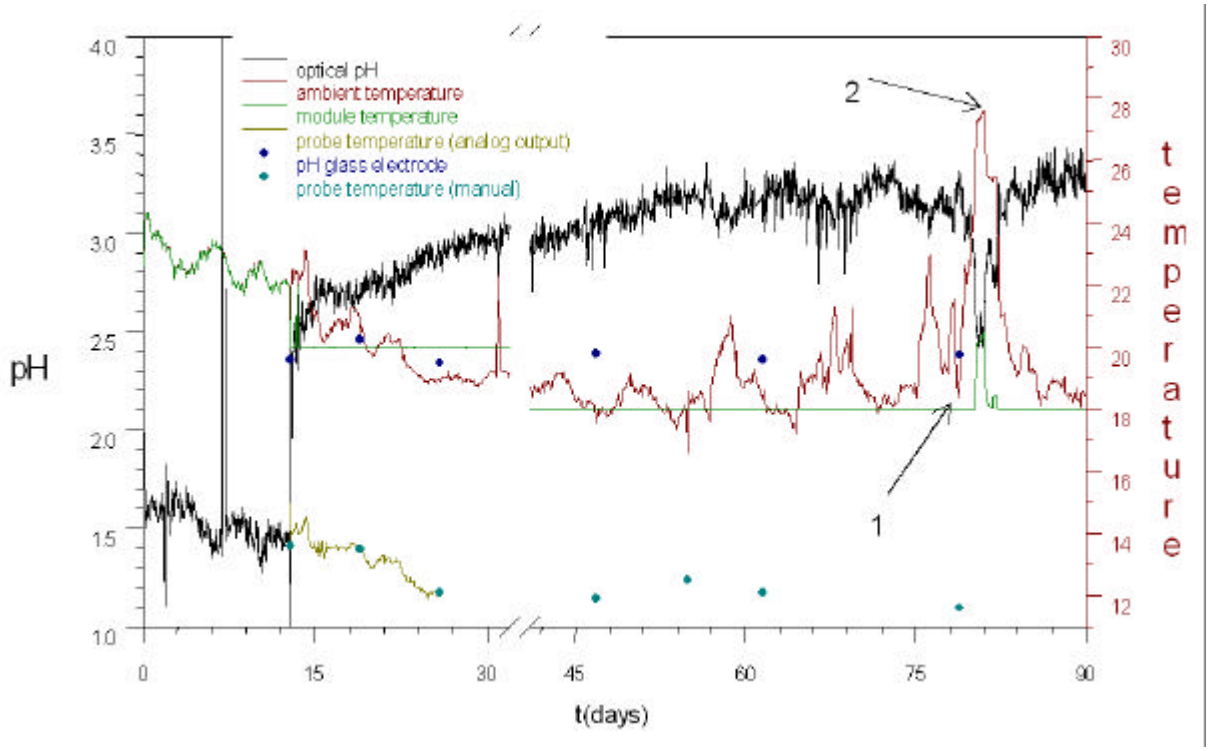

Fig. 3.63: Response curve of the optical pH sensor. The temperature curves are also given (in the first 12 days the ambient temperature and the temperature of the module were the same, since the temperature stabilisation of the electro-optical module containing the Led and the photo detector did not work)

The dependence of the sensor on the temperature is surely crucial. Three different temperature coefficient can be defined:

- α_1, temperature coefficient related to temperature changes of the instrumentation
- α_2, temperature coefficient related to temperature changes of the thermostatic module containing LED and photo detector
- α_3, temperature coefficient related to temperature changes of the probe

On this basis the true pH value is related to the measured pH values to the relationship:

$$pH_{true}(T) = pH_{measured} + \alpha_1 \cdot \Delta T_A + \alpha_2 \cdot \Delta T_M + \alpha_3 \cdot \Delta_{TP} + f(I) \qquad (3.1)$$

value, ΔT_M the change of the temperature of the module with respect to the initial value, ΔT_P the change of the temperature of the probe with respect to the initial value and f(I) is a function which takes into account the possible deterioration or photo-decomposition or leakage of the dye from the support.

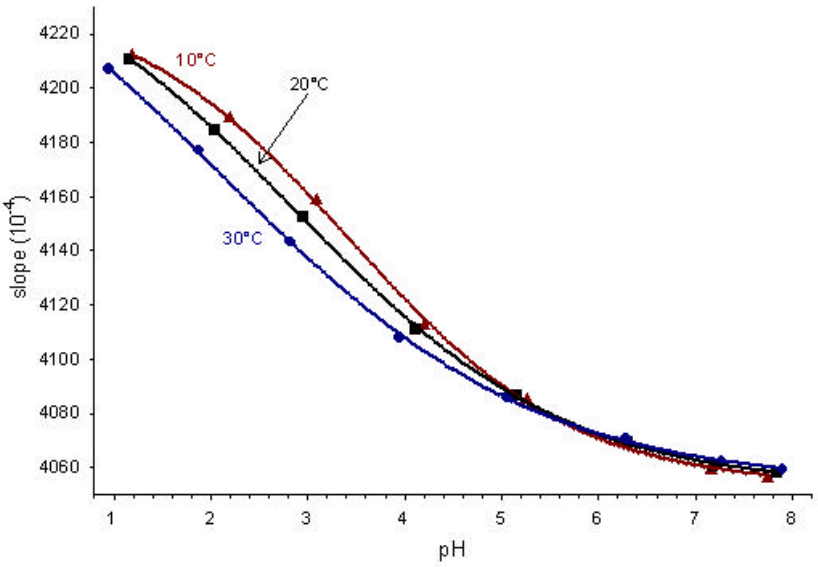

Fig. 3.64: Calibration curves for the three different temperatures.

Based on the calibration curve obtained at 10°C, 20°C and 30°C (Fig. 3.64), it can be concluded that the temperature coefficient α_3 is not constant at the different pH values. Around pH 3, it can be evaluated equal to 0.032. Therefore, for the measurement carried out in the mine, it can be considered that $\alpha_3 = 0.032$. If only the temperature of the probe changes, an increase of the temperature gives rise to a decrease of the measured pH value and vice versa.

A rough estimation of the coefficient α_1 can be obtained using the periods of times during which we can consider that the pH level is constant and that the only contribution dependent on temperature comes from the instrumentation.

For time t>45th day:

- the true real pH can be considered constant (measured values with the glass electrode showed only small changes)
- the probe temperature can be considered constant

Furthermore, if the considered periods of time are not too long, the effect of decomposition and deterioration of the dye can also be neglected (a period of time of ten days is acceptable on the bias of our previous experiments).

Three periods are considered:

1) 57-60 day

2) 63-72 day

3) 79-83 day without considering the period of time during which the temperature of the module changed. Fig. 3.65 shows the curves of pH versus T for different time periods

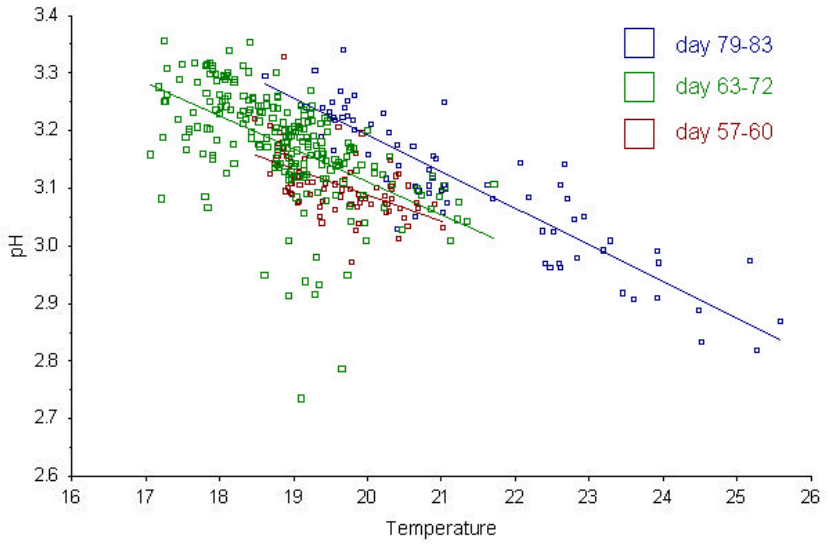

Fig. 3.65: pH versus temperature for three different periods of time

During this time the term f(I) should be negligible: that is there is no deterioration or leakage or photo-decomposition of the day within 10 days. If the regression line of the first order is considered, best results are obtained in the third case with a temperature coefficient α_1 equal to 0.064 and a correlation coefficient of 0.82. (In the other two intervals, the changes in temperature are too small and this prevents us to obtain a better a good correlation; in any case the calculated α_1 values are 0.057 and 0.045 so that the value of 0.064 can be considered as an acceptable estimation)

The value of the coefficient α_2 can be evaluated if the last collected data at day 32 and the first data at day 40 are compared. During this period the instrumentation did not work for problems to the power supply. When the instrument turned on again the temperature of the module has been changed from 20°C to 18°C (without making a new calibration):

So we have at t = day 32

$$pH_{true}\,(T) = pH_{measured} + \alpha_1 \cdot \Delta T_A + \alpha_3 \cdot \Delta T_P + f(I) \qquad (3.2)$$

since $\Delta T_M = 0$ and at t= day 40

$$pH_{true}\,(T) = pH_{measured} + \alpha_1 \cdot \Delta TA + 2 \cdot \alpha_2 + \alpha_3 \cdot \Delta T_P + f(I) \qquad (3.3)$$

since $\Delta TM = 2$

If:

1. the pH of the sample does not change (equal measured values at hour 26 and hour 47), that is $\Delta\, pH_{true} = 0$
2. f(I) remained constant that is no leakage, photo-decomposition or deterioration from day 32 to day 40
3. probe temperature T_P remained constant (measured values showed probe temperature almost constant)

the difference between equation (3.3) and (3.2) gives:

$$0 = pH_{measured}(\text{day } 40) - pH_{measured}(\text{day } 32) + \alpha_1 \cdot [(T_A)_{\text{at day } 40} - (T_A)_{\text{at day } 32}] + 2 \cdot \alpha_2 \qquad (3.4)$$

From the graph, roughly:

$pH_{measured}$(day 40) - $pH_{measured}$(day 32) = - 0.1

and

$[(T_A)_{at\ day\ 40} - (T_A)_{at\ day\ 32}]$ = - 0.5 °C

so that, $\alpha_2 = 0.066$

The calculated values of α_1 and α_2 can be checked by the evaluation of $\Delta pH_{measured}$ between point 1 and point 2 in the graph (roughly at day 78, see Fig. 3.65). Since the interval of time is short we can consider

$\Delta pH_{true} = 0$

$\Delta T_{probe} = 0$

$\Delta f(I) = 0$

so that $0 = (pH_{measured})_1 - (pH_{measured})_2 + \alpha_1 \cdot [(T_A)_1 - (T_A)_2] + \alpha_2 \cdot [(T_M)_1 - (T_M)_2]$ (3.5)

From the graph it follows that:

- $[(T_A)_1 - (T_A)_2]$ = - 9°C (3.6)
- $[(T_M)_1 - (T_M)_2]$ = -2.5 °C (3.7)

Therefore from equation (3.5) we obtain:

$(pH_{measured})_1 - (pH_{measured})_2 = 0.741$ (3.8)

which is in agreement with the change in the measured pH value.

Fig. 3.66 shows the corrected pH value (green curve) compared with the measured values (red curve) and with the pH measured with the glass electrode. The calculation has been made only after the day 13.

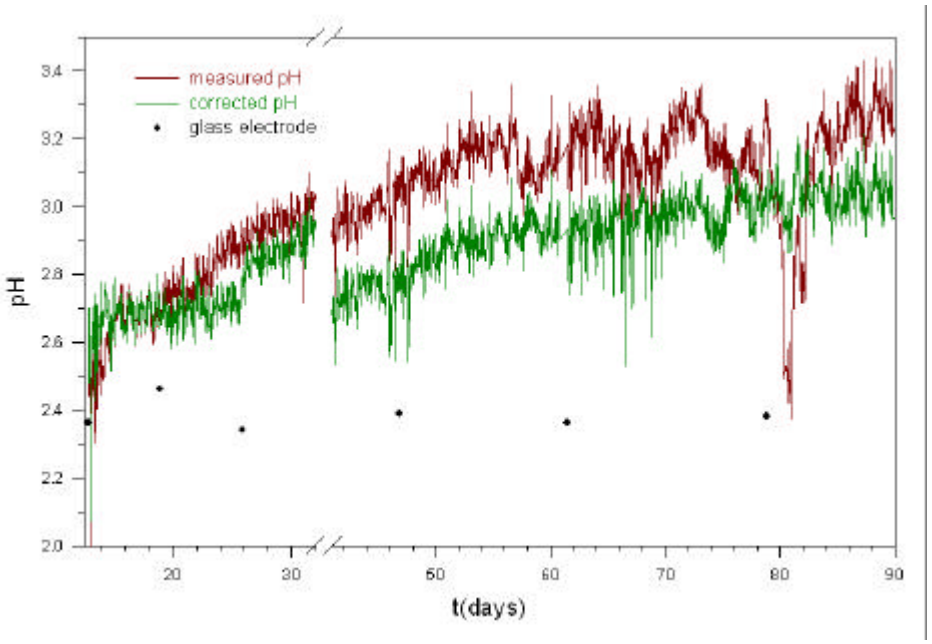

Fig. 3.66: Corrected pH value compared with the measured value.

It can be seen that the high change observed at day 80 is an effect of the big change of temperature. The correction is based on the hypothesis that:

1. there is no change in the temperature of the probe, during all the time in which the temperature of the probe is not measured with the analogue input;
2. the true pH value (considered as the value measured by the glass electrode) has been constant.

On this basis, the discrepancy between the measured pH and the true value should be caused only by the partial photo-decomposition or leakage of the dye.

The gap between day 32 and day 40 is not well understood; this could be due to some changes of the experimental conditions (only the changes of the temperature in the module are considered).

A rough evaluation of the leakage, photo-decomposition or deterioration can be done finding the linear plot pH=f(time). I limited this evaluation to the time intervals 12-32 and 40-62, where the relationship between pH and time is linear.

The slope of the curves in the two interval are quite similar:

- 0.0129 for the interval 12-32 (correlation coefficient 0.71) (Fig. 3.67).
- 0.0155 for the interval 40-62 (correlation coefficient 0.64) (Fig. 3.68).

The average value 0.014 would be the pH drift per day (0.0006 pH/hour) which is not so bad.

The fact that after day 62 the curve seems more stable (Fig. 3.69) could be due to the fact that there is no more leakage since all the molecules of the dye which were “badly” bound to the support were already removed (this is the optimistic interpretation and I wouldn’t bet on it). In any case I did not consider the time after day 62 for this calculation.

The error is always less than 0.7 pH. The effect of decomposition could be decreased by decreasing the duty cycle or increasing the sampling time (2 hours instead of 1 hour).

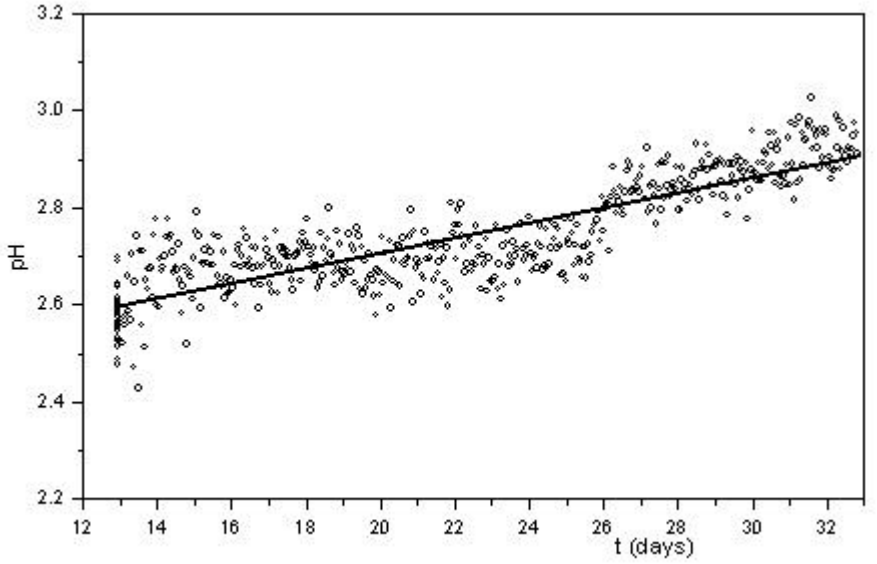

Fig. 3.67: pH versus time in the interval: day 12-32.

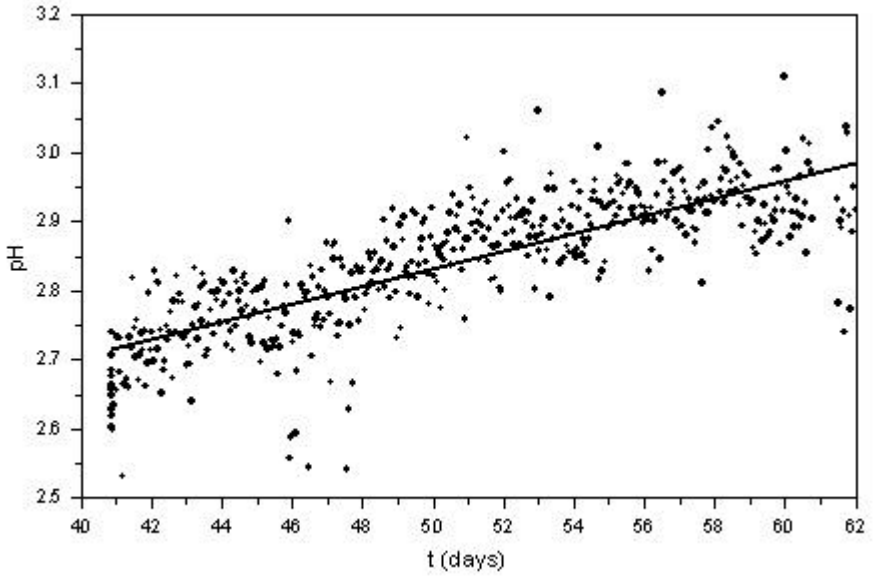

Fig. 3.68: pH versus time in the interval: day 40-62.

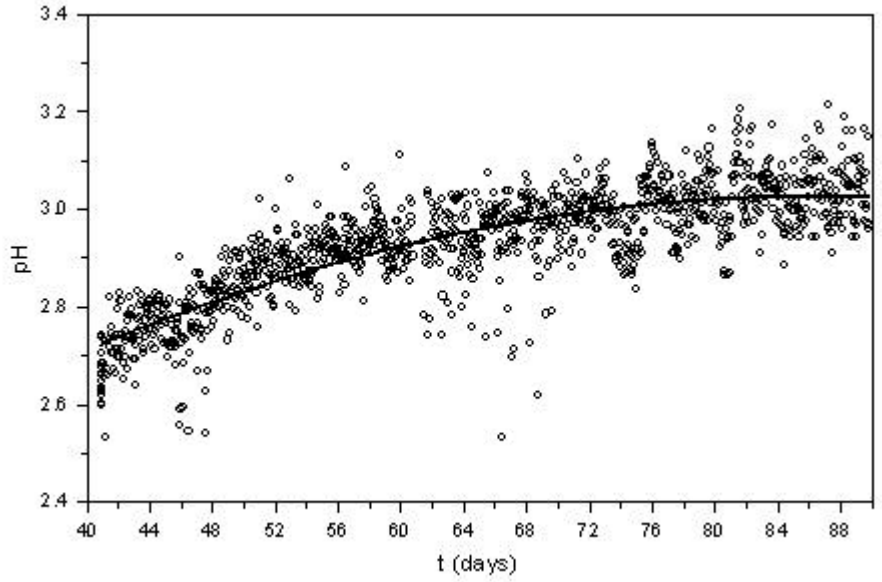

Fig. 3.69: pH versus time in the interval: day 40-88.

3.4.4. Conclusions

In general it can be concluded that the development of a fiber optic pH-sensor was very successful in terms of normal short term measurements. The measurements did represent very well the actual pH-variation within a short term. The remaining problem is the long term drift.

The drift did change from 0.6 to 1 on the pH scale. Several possible reasons for this drift can be defined. The most important of them are bleaching of the reflector's dye (photo-decomposition) and/or degeneration of the LED performances. The later problem is a sever problem that is general for intensity based sensing technologies.

Others could be turbidity in the flow stream and temperature effects which are not compensated for.

For future work, two possibilities are proposed:

1. Continuing with this amplitude modulated technique and try to reduce this drift effect. This can be done by: (A) Performing more research to select a LED with very stable performances. (B) Decreasing the optical power on the immobilised indicator in order to decrease the photo-decomposition. This could be obtained by increasing the time between different measurements or by working at a wavelength around 600 nm. At this wavelength we have an other inflection point of the absorption curves. The slope is in this case less but the energy of the transported beam is smaller.
2. Working with a wavelength modulated technology in stead of intensity (amplitude) based technology. As an example, a development of a pH-sensor based on Fibre Bragg Gratings can be considered. This type of technology has the advantage that the measurements are not influenced by the changes or fluctuations in performances of the LED, bending or other loss effects. The results can therefore be expected to be much more stable and reliable as function of time.

3.5. Äspö URL

3.5.1. Sensors

The installation at the Äspö URL (project TBT) took place at 29 and 30 of January 2003. Two pore water sensors (one in stainless steel 316 and one in Titanium) and two total pressure sensors (also one in stainless steel 316 and one in Titanium) which have to withstand pressure ranging up to 50 and 150 bar respectively and temperatures as high as 180° C have been installed. A detailed description of the sensor lay-out can be found in paragraph 1.5 and 1.6.

3.5.2. Experimental set-up

The sensors have been embedded in a separate bentonite layer to measure the water and earth pressure as well as temperature when water intrusion is initiated.

A demo version of the total system can be seen in Fig. 3.70. An excavation with 1.75 m diameter and 8.5 meters depth has been foreseen in the granite block. Within the excavation, compacted bentonite rings are placed. In the middle of the bentonite rings, a canister surrounded by a 5 cm thick copper protection has been positioned. In this copper housing there is a Stainless Steel structure to insert the waste-capsules. The sensors are embedded in the bentonite rings and guided to the surface via special slots in the granite.

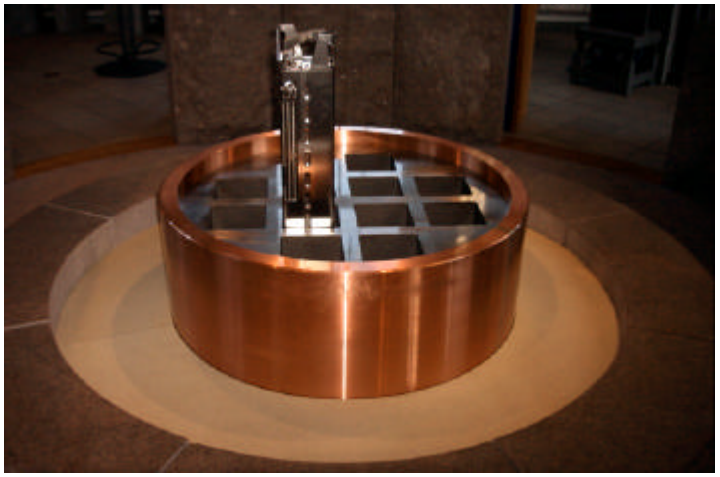

Fig. 3.70: View of the mock-up design.

The technical details are shown in Fig. 3.71. There are 16 regions of each 0.5 meter bentonite which are divided in 7 measuring sections. Two canister of each 3 meters are separated by a bentonite block of 0.5 meter. In the lowest block the bentonite surrounds the canister and in the upper block there is a backfill layer of 0.2 meter of sand between the canister and the bentonite. The sensors have been placed in 2 different sections: section 2 (lower block) and section 5 (upper block). Fig. 3.72 and Fig. 3.73 show the drawings of these sections. The sensor locations are indicated by the words 'DBE Special'.

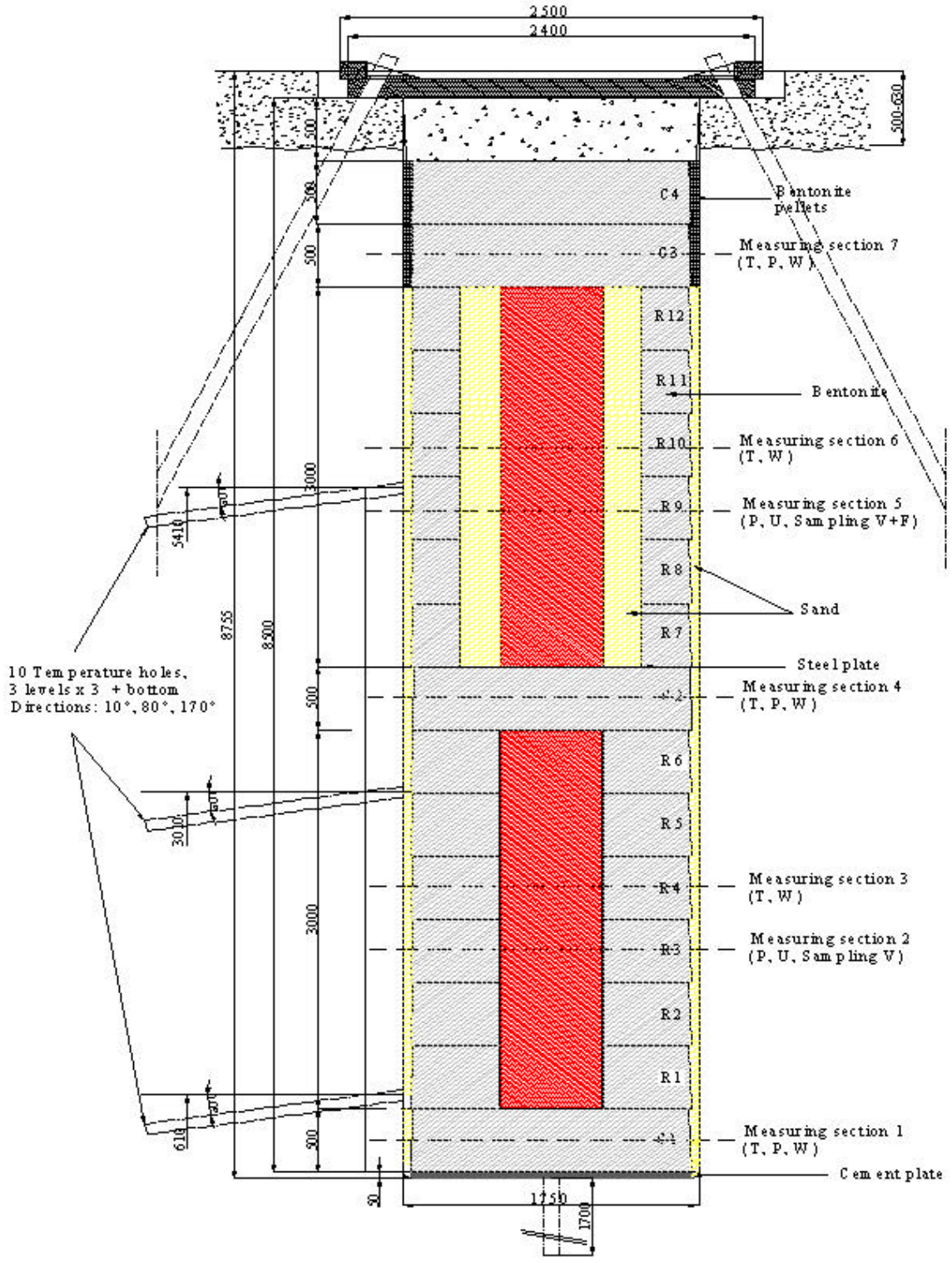

Fig. 3.71: Technical drawing of set-up

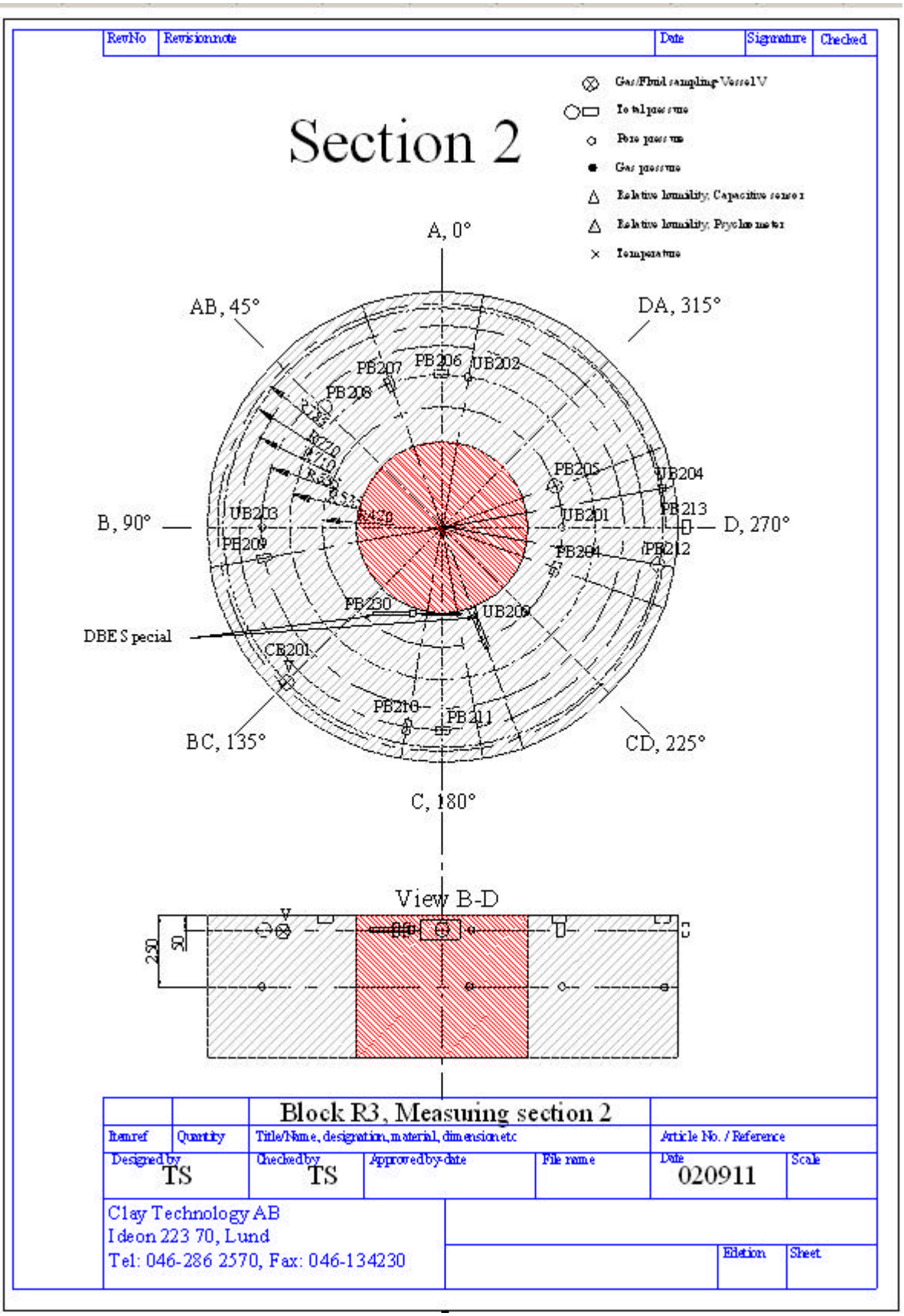

Fig. 3.72: Drawing of Block R3 in section 2

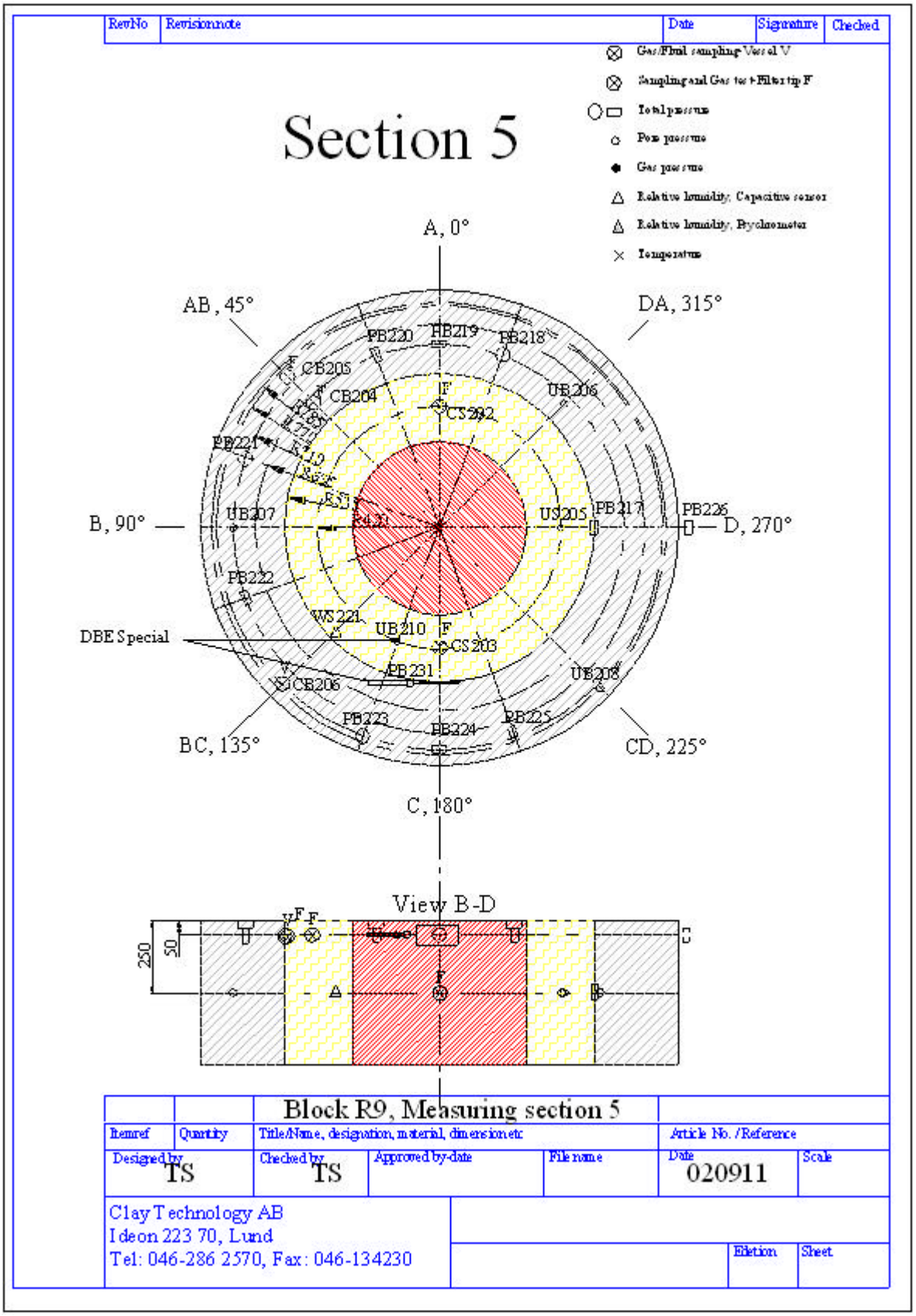

Fig. 3.73: Drawing of Block R9 in section 5

In section 2 block 3, two Titanium sensors have been installed:

- PW-Ti-50 bar (SN03012801) - Titanium Pore Water Pressure sensor 50 bar (UB209)
- TP-Ti-150 bar (SN03012802) - Titanium Total Pressure sensor 150 bar (PB230)

In section 5 block 9, two Stainless Steel sensors have been installed:

- PW-SS316-50 bar (SN03012803) - Stainless Steel 316 Pore Water Pressure sensor 50 bar (UB210)
- TP-SS316-150 bar (SN03012804) - Stainless Steel 316 Total Pressure sensor 150 bar (PB231)

The notation in bold letter type is the one assigned by Clay Technology.

During the installation, Clay Technology prepared the bentonite blocks for the embedding of the sensor. At the same time ID FOS assembled the wiring and tubing of the Ti-sensors for their final installation in the bentonite blocks. The bentonite were easy to work with as it was easy to cut and saw or drill some holes in the bentonite. ID FOS fine tuned the bentonite blocks sparings and the sensors with their tubing were bended to fit into the grooves and the slots in the granite.

Fig. 3.74 shows the position of the 2 Titanium sensors in the bentonite block R3. These sensors will come almost directly in contact with the canister. As can be observed the Pore Water Pressure sensor is pointed to the canister and the Total Pressure sensor is directly placed across the canister to be able to measure the direct impact of the swelling pressure and heating up of the system.

To guide the fibres to the surface, a 8 meters long Titanium tubing has been used. They have been mounted with special made Titanium tube to tube connections from Swagelok. Out of the hole, the connection has been performed from the Titanium tubing to a polyethylene tubing of 25m length which is more flexible and easier to use to connect to the measurement rack. The cabling is shown in Fig. 3.75.

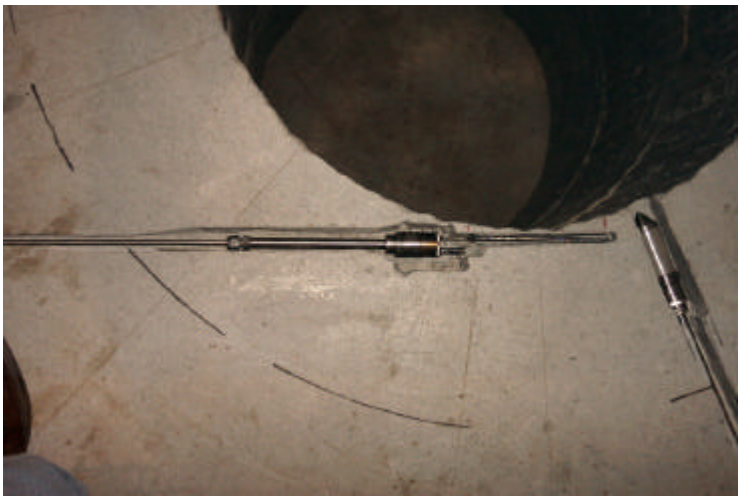

Fig. 3.74: Position of the Titanium sensors in the bentonite block R3

Fig. 3.75: View from the surface into the borehole.

A similar installation has been performed for the stainless steel sensors.

3.5.3. Interrogation system

The interrogation system has been installed in the control room located at approximately 12 meters of the experimental set-up. All connections have been easily guided to this control room.

Initially, the system was based on a double FossFibreScan interrogation system. Fig. 3.76 shows the measurement rack. The rack itself is fabricated by Schroff Europe and is fully 19 inch compatible. The rack is IP 56 protected. The rack has a glass front door for easy access, monitoring and data retrieval. It also has a mountable back plate with dust-free sealing. Initially the system has been equipped with the following components:

- a double integrated FossFibreScan
- 1 by 4 optical switch from JDS Uniphase
- Laptop: The laptop used is a Dell latitude 800.
- UPS: The UPS used in the rack is the Pulsar Extreme 1000 VA from MGE. It provides 1000VA (1000 Watt) when the main power goes down. With this UPS, an autonomy of about 2 hours is obtained. The laptop isn't connected to the UPS because the internal batteries have already an autonomy of 2h30. The UPS is the blue unit at the lowest position in the rack.

Fig. 3.76: Measurement rack with double FossFibreScan unit

Due to some unexplained power errors from the main power supply net, a damage of the FossFibreScan has occurred. The system has therefore been replaced by a MOI based system. Also the 1x4 optical switch needed to be replaced by a 1x8 optical switch due to the increase of the number of sensors for the Prototype Repository experiments. The current system is shown in Fig. 3.77.

Fig. 3.77: Measurement rack with MOI interrogation system. MOI unit has been positioned after blind panel.

Remote access is also here possible using the PC Anywhere software. The software is programmed to power-up automatically and auto run the measurement software when the laptop is rebooted. So when a power failure occurs the laptop does automatically restart and reboot the system. The PC Anywhere will be automatically restarted when the computer reboots.

3.5.4. Additional sensors

The sensing system at Äspö for the TBT experiments has been extended with 4 additional sensors. These sensors have been installed in the “Prototype Repository” experiment set-up. The following sensors have been installed:

- PW-SS316-50 bar (SN03031001) - Stainless Steel 316 Pore Water Pressure sensor 50 bar
- PW-SS316-50 bar (SN03031002) - Stainless Steel 316 Pore Water Pressure sensor 50 bar
- TP-SS316-150 bar (SN03031003) - Stainless Steel 316 Total Pressure sensor 150 bar
- Temperature chain (SN03031004) – Stainless steel tube with 4 FBGs inside.

The temperature chain consists of 4 FBG sensors put into a stainless steel capillary. The FBG-locations are shown in Fig. 3.78. The cable is put in the radial directions in the bentonite block what allows to obtain a radial distribution of the temperatures. Fig. 3.79 shows the positioning of the total pressure sensor.

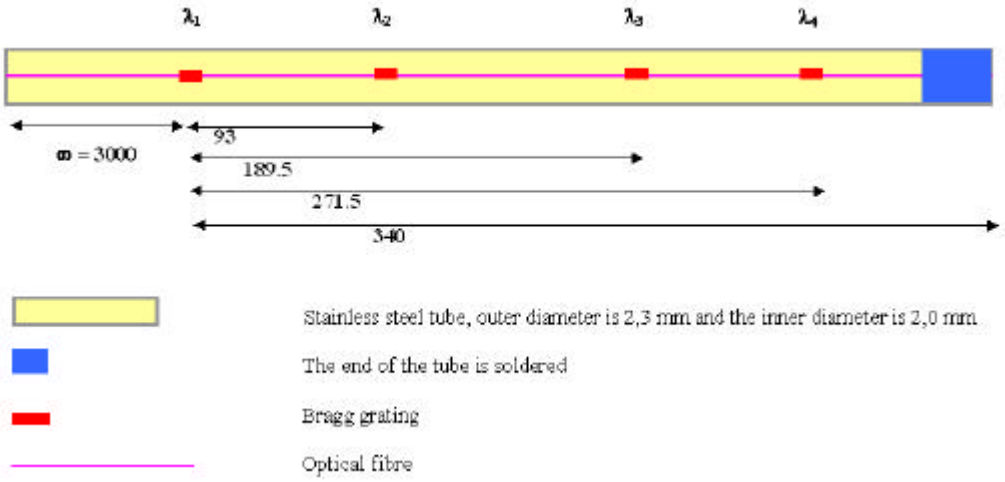

Fig. 3.78: Lay-out temperature cable

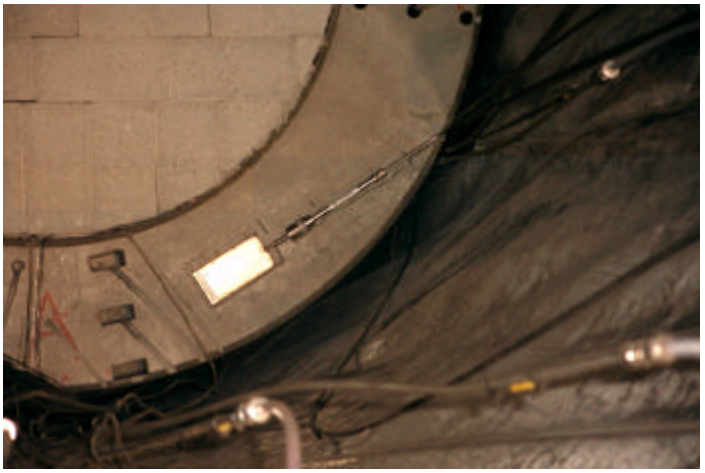

Fig. 3.79: Positioning sensor TP-SS316-150 bar (SN03031003)

The same interrogation system as used for the TBT experiments is used, see 3.5.3. The sensor tubes are connected to the interrogation system at the TBT site using a 500m long standard outdoor telecom cable containing 16 fibres.

The future work related to this experiment will be performed in the framework of another research project (02E9743) also funded by the Federal Ministry of Economics and Labour (BMWA = Bundesministerium für Wirtschaft und Arbeit). Results will be given and evaluated in the corresponding reports.

4. References

1. M.A. Butler and R.J. Bus, Sensors and Actuators B, 11 (1993) 161
2. X. Bévenot, A. Trouillet, C. Veillas and H. Gagnaire, Sensors and Actuators B67 (2000) 57
3. Mueller W.M., Blackledge J.P., Libowitz G.G., Metal hydrides, Academic New York, 1968
4. M. Eriksson, L.G. Ekedahl, Applied Surface Science 133 (1998) 89
5. M. Eriksson, L.G. Ekedahl, Sensors and actuators B42 (1997) 217
6. M.P. Kiskinova, G.M. Bliznakov, Surface Science 123 (1982) 61
7. G.A. Kok, A. Noordemeer, B.E. Nieuwenhuys, Surface Science 135 (1983) 65
8. I. Ratajczykowa, Surface Science 172 (1986) 691
9. Y.T. Peng, Y. Tang, J.S. Sirkis, Proceedings OFS-13 conference
10. Meltz G, Hewlett S J, and Love J D "Fiber grating evanescent-wave sensors", Proceedings of SPIE, Vol. 2836 Chemical, Biochemical, and Environmental Fiber Sen-sors VIII, (1996) 342
11. Asseh A, Sandgren S, Ahlfeldt H, B Sahlgren, R Stubbe, and Edwall G "Fiber optical Bragg grating refractometer", Fiber and Integrated Optics, Vol. 17, (1998) 51
12. Falciai R, Mignani A G, and Vannini A "Solution concentration measurements by means of optical fiber long-period gratings", Proceedings of SPIE, Vol. 3483: Euro-pean Workshop on Optical Fibre Sensors, (1998) 95
13. Patrick H J, Kersey A D, and Bucholtz F “Analysis of the response of long period fiber gratings to external index of refraction”, J. of Lightwave Technology, vol. 16, no. 9, (1999) 1606.
14. *Jobmann, M., Fischer, S., Voet, M. 2000:* Development and test of redundant fiber optic sensing systems with self operating control for monitoring at final disposal sites, Final Report, DBE, Peine.
15. Polster, M., Schonebeck, M., Jobmann, M. 2005: Investigation on thermal expansion effects in clay formations, F+E-Vorhaben TEE, Jahresbericht 2004, DBE TECHNOLOGY, Peine.